UDC 621
CODEN: MINSC5
In print: ISSN 1857 – 5293
On line: ISSN 1857 – 9191

MECHANICAL ENGINEERING SCIENTIFIC JOURNAL

МАШИНСКО ИНЖЕНЕРСТВО НАУЧНО СПИСАНИЕ

Volume 43
Number 1

Skopje, 2025

Mech. Eng. Sci. J.	Vol. 43	No. 1	pp. 1–70	Skopje 2025
Маш. инж. науч. спис.	Год.	Број	стр.	Скопје

MECHANICAL ENGINEERING – SCIENTIFIC JOURNAL
МАШИНСКО ИНЖЕНЕРСТВО – НАУЧНО СПИСАНИЕ

Published by
Faculty of Mechanical Engineering, Ss. Cyril and Methodius University in Skopje, North Macedonia
Издава
Машински факултет, Универзитет „Св. Кирил и Методиј" во Скопје, Северна Македонија

Published twice yearly – Излегува два пати годишно

UDC: "St. Kliment Ohridski" Library – Skopje — УДК: НУБ „Св.. Климент Охридски" – Скопје

Copies: 300 — Тираж: 300

Price: 520 denars — Цена: 520 денари

Address — Адреса
Faculty of Mechanical Engineering — **Машински факултет**
(Mechanical Engineering – Scientific Journal) — (Машинско инженерство – научно списание)
Editor in Chief — Одговорен уредник
P.O.Box 464 — пошт. фах 464
MK-1001 Skopje, Republic of North Macedonia — МК-1001 Скопје, Република Северна Македонија

Mech. Eng. Sci. J. is indexed/abstracted in INIS (International Nuclear Information System)
www.mf.ukim.edu.mk

MECHANICAL ENGINEERING – SCIENTIFIC JOURNAL
FACULTY OF MECHANICAL ENGINEERING, SKOPJE, REPUBLIC OF NORTH MACEDONIA

МАШИНСКО ИНЖЕНЕРСТВО – НАУЧНО СПИСАНИЕ
МАШИНСКИ ФАКУЛТЕТ, СКОПЈЕ, РЕПУБЛИКА СЕВЕРНА МАКЕДОНИЈА

Mech. Eng. Sci. J.	Vol.	No.	pp.	Skopje
	43	1	1–70	2025
Маш. инж. науч. спис.	Год.	Број	стр.	Скопје

TABLE OF CONTENTS
(С О Д Р Ж И Н А)

HYDRAULIC ENGINEERING
(Хидраулично инженерство)

PRODUCTION ENGINEERING
(Производно инженерство)

ENERGY AND ENVIRONMENT
(Енергетика и животна средина)

MECHATRONICS
(Мехатроника)

Mechanical Engineering – Scientific Journal, Vol. **43,** No. 1, pp. 5–16 (2025)
Number of article: 688
In print: ISSN 1857–5293
Received: May 12, 2025
On line: ISSN 1857–9191
Accepted: May 30, 2025
UDC: 621.644.063-423.4:004.942
https://doi.org/10.55302/MESJ2543151l

Original scientific paper

T-JUNCTION AND TRANSFER OF TRANSIENT MODES IN HYDRAULIC SYSTEMS

Marija Lazarevikj, Viktor Iliev, Zoran Markov, Valentino Stojkovski

Faculty of Mechanical Engineering, "Ss. Cyril and Methodius" University in Skopje, P.O.Box 464, MK-1001 Skopje, Republic of North Macedonia
marija.lazarevikj@mf.edu.mk

A b s t r a c t: A T-junction of a hydraulic system is the point where hydraulic parameters (which are defined by variable pressure and discharge) join or separate. The transmission of the hydraulic conditions distributed by the T-junction connection are numerically analyzed in different conditions which provide insight into the distribution – transfer of hydraulic parameters through the T-junction. Numerical calculations were performed for defining the transient modes and the interaction between the hydraulic parameters in the case of a T-junction with the application of the AFT Impulse software package. The software was chosen as suitable based on previous experience with good alignment between numerical calculations and field measurements. The results from the numerical prediction of the occurrences for different conditions in the T-junction construction showed the influence of simultaneity (interaction and dissipation) of the fluid flow parameters, time delay or parallel flow and counter-flow in the transient modes, which contribute to the technical opinion on the phenomena occurring in a T-junction.

Key words: transient modes; interference; dissipation; fluid flow parameters

Т-ЈАЗОЛ И ПРЕНОС НА ПРЕОДНИ РЕЖИМИ ВО ХИДРАУЛИЧНИ СИСТЕМИ

А п с т р а к т: Т-јазол на хидрауличен систем е точката каде што хидрауличните параметри (кои се дефинирани со променлив притисок и проток) се спојуваат или се одделуваат. Преносот на хидрауличните услови дистрибуирани преку Т-јазолот е нумерички анализиран во различни услови, што дава увид во распределбата – преносот на хидрауличните параметри низ Т-јазолот. Со цел дефинирање на преодните режими и интеракцијата помеѓу хидрауличните параметри во случај на Т-јазол, извршени беа нумерички пресметки со примена на софтверскиот пакет AFT Impulse. Изборот на софтверот е направен врз основа на претходното искуство со добро усогласување помеѓу нумерички пресметки и теренски мерења. Резултатите од нумеричкото предвидување на појавите за различни услови во Т-јазолот покажуваат влијание на истовременоста (интеракција и дисипација) на струјните параметри, временското задоцнување или истонасочно и противнасочно струење во преодните режими, што придонесува кон техничкото мислење за феномените што се случуваат во Т-јазолот.

Клучни зборови: преодни режими; интерференција; дисипација; струјнотехнички параметри

INTRODUCTION

The fluid flow parameters during a transient fluid flow in pipeline systems is a result of a complex set of independently variable parameters. They originate from the physical properties and mechanisms of the kinematics of the surrounding, as well as from the fluid properties at given flow parameters. They are described at unsteady state in a given section of the flow domain [1, 2]. The fluid and its basic physical quantities (density, compressibility, viscosity) are given based on generally known parameters, but the kinematics of their change under different conditions during the fluid flow is a mechanism for which research is still being carried out [3, 4]. The interaction between the surrounding and the fluid medium occurs in conditions of transient flow regimes in pipelines.

Numerical simulation has become the dominant method for analyzing transient flow phenomena. The main challenge in modeling water hammer lies in solving the hyperbolic partial differential equations involved. While the governing equations are available in closed form, no exact analytical solution currently exists. To obtain numerical solutions, several techniques have been employed, most notably the Finite Difference Method (FDM) which can include Lax-Wendroff Scheme and MacCormack Method [5], the Finite Volume Method (FVM), the Finite Element Method (FEM), and the Method of Characteristics (MOC).

Pal et al. [6] review recent advancements in numerical methods for modeling water hammer, focusing on one-dimensional approaches like FDM, MOC and FVM. Although MOC has been the most widely used method, especially in one-dimensional transient flow modeling, the authors highlight the advantages of FVM for accurate transient flow simulations, especially in complex scenarios like fault detection. Henclik [7] presents a numerical approach to modelling water hammer phenomena incorporating fluid–structure interaction (FSI) using a four-equation model solved via MOC. The study emphasizes the influence of viscoelastic pipe supports, formulating boundary conditions as differential equations of junction motion, which are solved concurrently with MOC compatibility equations. Numerical simulations, validated against experimental data from a laboratory pipeline model with complex support systems demonstrate that appropriately designed supports can significantly reduce pressure surges by absorbing and dissipating energy. Prica et al. [8] developed a numerical model to simulate condensation-induced water hammer in two-phase flows. Utilizing MOC, the model accounts for the direct condensation of steam on subcooled liquid and tracks the interface between steam and water columns. The model is validated through application to a laboratory test case. Ani and Khayatzadeh [9] developed a general computer program for analyzing pipelines with pumps, valves, surge tanks, air chambers, etc., based on FDM and MOC coupling. The accuracy of their program is validated by comparing numerical results to available exact analytical solutions. Kandil et al. [10] investigated the impact of different pipe materials on water hammer intensity and frequency in pressure pipelines by integrating experimental testing and numerical modeling. A numerical model based on MOC was developed and validated using data from a custom experimental setup equipped with pressure sensors and strain gauges. The research evaluated five pipe materials under various flow rates and pressures. Fast Fourier Transform (FFT) analysis revealed different frequency responses of each material, showing that more viscoelastic materials mitigate water hammer effects compared to rigid materials like steel. Deviations between experimental and numerical results were attributed to differences in pipe rigidity. Toumi and Sekiou [11] employed MOC and a mixed scheme for simulating transient flow. The results revealed that for each slow closing time, there is a unique convex law that effectively reduces maximum overpressure. Furthermore, the evolution of the optimal pressure at the valve is governed by two models: exponential and linear.

The literature review shows that the Method of Characteristics (MOC) is the most widely adopted approach which is extensively used in engineering applications to simulate water hammer effects especially in case of problems with relatively simple geometries and boundary conditions, like valve closures or pump failures.

Understanding transient flow behaviour in complex pipeline networks is essential for the safe and efficient design of hydraulic systems. The transient state of the junction element is considered in this paper, since different states are possible at this nodal point that can be achieved during the pipeline operation, i.e., it is possible for one branch of the junction to have inflow or outflow or no flow through it. On the other hand, the part of the pipeline where redistribution of flow to the branches occurs is in the junction. From a hydraulic point of view, the junction is a place in the pipeline where the influence of the surrounding is minimal or none from aspect of transient states of the fluid, but the hydraulic conditions are more dominant since a pressure wave is distributed or two pressure waves are superimposed. In particular, T-junctions present critical points where pressure wave interactions can lead to amplified loads, potentially compromising system integrity. Thus, in this paper, the MOC is selected as a numerical approach for defining the transient states at T-junction in pipelines through a one-dimensional model of analysis along the flow. The presence of a specific pipeline components (reservoir, valve, pump, accumulator, etc.) is given through appropriate mathematical boundary models to describe their influence and specificity. The junction model as a boundary condition is developed on the following assumptions: the head in the junction is constant for all its branches, while the pressure wave propagation towards the junction has a positive sign of the characteristic function C for a branch with fluid flow velocity in the same direction as the pressure wave propagation speed and vice versa [1, 2, 4, 12]. This research uses AFT Impulse with the MOC to simulate and analyze transient flow in a T-junction. The goal is to quantify how the length ratio between parallel branches influence wave intensity, timing and oscillation patterns, thereby improving predictive capabilities for transient behaviour in branched pipeline systems.

MODEL SETUP

The conditions for transient states transmission in a pipeline with a T-junction that connects three branches were numerically analyzed. The fluid flows from a tank with a constant level through a pipeline and is evenly distributed into two horizontal parallel branches positioned at the same elevation.

Two models of parallel branches were considered: a pipeline with branches of same length (with 1:1 length ratio) and a pipeline with parallel branches whose length ratio is 1:2. The length of the shorter branch of the pipeline model 1:2 is the same as the length of the branches of the 1:1 model. By assigning different lengths to the branches, it is ensured that the pressure wave induced by opening/closing the flow in the branch is present in the junction at different times.

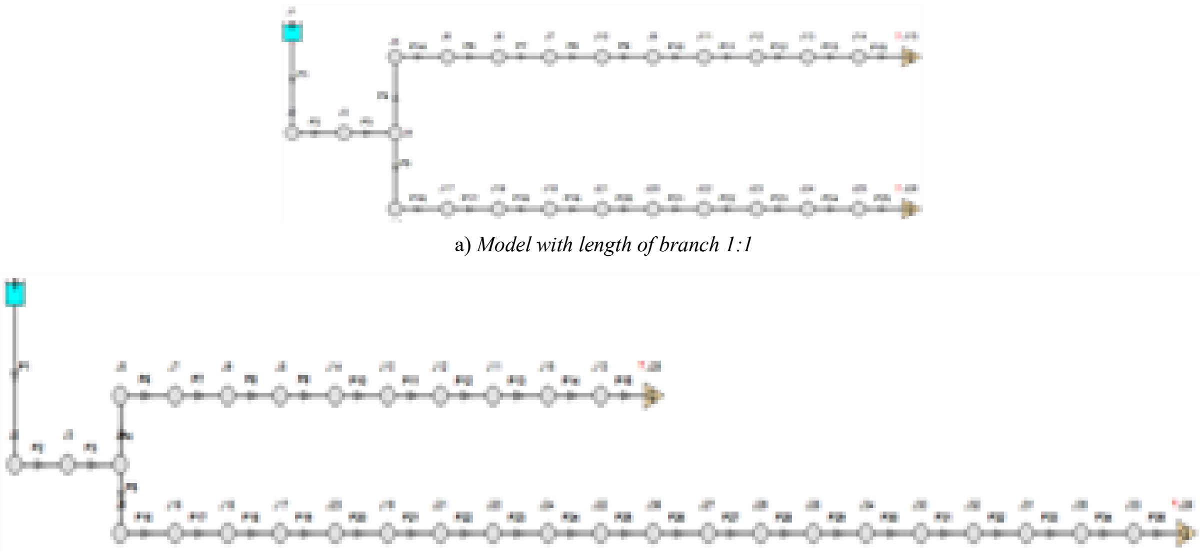

a) *Model with length of branch 1:1*

b) *Model with length of branch 1:2*

Fig. 1. Schematic of the models for T-junction

Technical parameters of model

Basic technical parameters for the models considered are:

- the water level in the reservoir is constant, set at 100 m height relative to the T-junction,
- the supply pipe (made of steel) to the T-junction (section 3) is 200 m long and has a diameter of DN600 and a wall thickness of 4.5 mm,
- the short branch has a total length of 1500 m, set with 150 m step,
- the longest branch length is 3000 m, set with 150 m step,
- at the ends of the branches, the flow is set at constant value of 0.1 m^3/s.

The conditions under which the numerical calculations were performed are:

- Fluid-water.
- The time duration of opening/closing the flow in the branch is 2 seconds.
- The law of change of flow is linear.
- Number of divisions-steps of calculation nodes is 5 m.
- Calculation time is set for 20 seconds.
- During the calculations, in the first second, the stationary state conditions of the pipeline system are set, and then the changes follow.

Numerical calculations were performed using the commercial software package AFT-Impulse.

Scenarios for calculated cases

Transient regimes in the T-junction are considered under conditions of positive pressure wave (flow closure), negative pressure wave (flow opening), as well as with the combined action of pressure waves. The different scenarios considered for the 1:1 model and for the 1:2 model are given in Table 1 and Table 2, respectively. Junctions J15 and J26 represent the ends of the parallel branches where the flow either closes or opens. For every scenario, the original state of the branch (opened/closed) is given, so as the time for completing the action of opening/closing at the respective branch end. The corresponding symbol for the resulting change, which is used in the graphical presentation of the results, is given in the second column of the tables.

Table 1

Scenarios of numerical calculations for a model with the same length of branches (1:1)

Scenario		J15			J26		
Number	Symbol	Start	Time	End	Start	Time	End
1	Zs-Zs	open	2 sec	closed	open	2 sec	closed
2	Zs-Xs	open	2 sec	closed	closed	no action	closed
3	Xs-Zs	closed	no action	closed	open	2 sec	closed
4	Os-Os	closed	2 sec	open	closed	2 sec	open
5	Xs-Os	closed	no action	closed	closed	2 sec	open
6	Os-Xs	closed	2 sec	open	closed	no action	closed
7	Os-Zs	closed	2 sec	open	open	2 sec	closed
8	Zs-Os	open	2 sec	closed	open	2 sec	closed

Table 2

Scenarios of numerical calculations for a model with different branch lengths (1:2)

Scenario		J15			J26		
Number	Symbol	Start	Time	End	Start	Time	End
1	Zs-Zl	open	2 sec	closed	open	2 sec.	closed
2	Zs-Xl	open	2 sec	closed	closed	no action	closed
3	Xs-Zl	closed	no action	closed	open	2 sec	closed
4	.+s-Zl	open	no action	open	open	2 sec	closed
5	Zs-+l	open	2 sec	closed	open	no action	open
6	Os-Ol	closed	2 sec	open	closed	2 sec	open
7	Zs-Ol	open	2 sec	closed	closed	2 sec	open
8	Os-Zl	closed	2 sec.	open	open	2 sec	closed
9	.+s-Ol	open	2 sec	open	closed	2 sec	open
10	Os-+l	closed	2 sec	open	open	2 sec	open
11	Xs-Ol	closed	no action	closed	closed	2 sec	open
12	Os-Xl	closed	2 sec	open	closed	no action	closed

RESULTS AND DISCUSSION

The results of the calculations for the transient modes are analyzed primarily for the pressure distribution in the T-junction, by defining the pressure change in section 3 (supply pipeline to the junction), section 4 and section 5 (branches from the junction). The results are given in the form of diagrams which show the pressure and flow change in each individual section, as well as a comparative diagram for the pressure distribution. In addition, the pressure and flow change diagrams at the point where the transient mode is induced in the pipeline system are given. The branch from which the transient mode is induced in the system is given on the comparative diagrams with a dashed line.

Effects of a positive pressure wave

Unsteady flow with the positive pressure wave is ensured by closing the parallel branches, i.e., by stopping the flow. The cases of pressure distribution in the T-junction during simultaneous closing of the parallel branches and the case when the flow is closing in only one branch while the other is already without flow are considered.

Simultaneous closure of branches

The transitional states in the pipe system in the T-junction zone under conditions of simultaneous closure of the flow in the branches are given in Figure 2 and Figure 3.

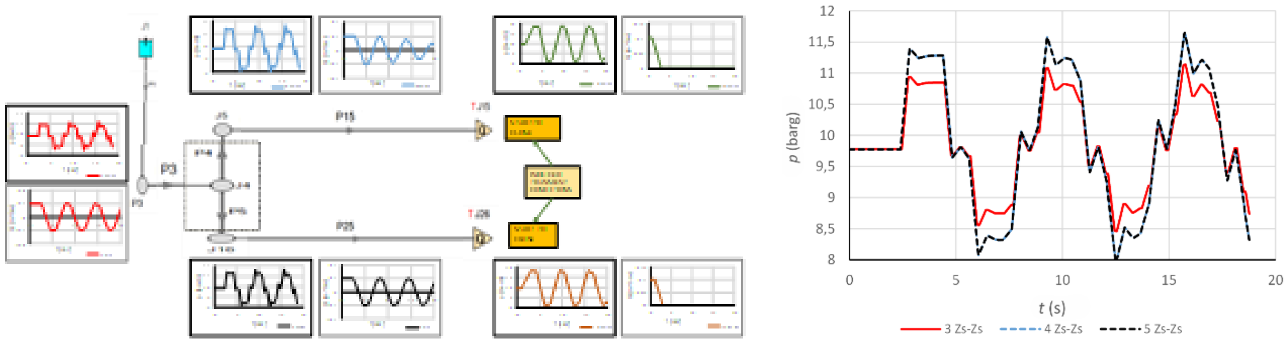

a) Pressure wave distribution at T-junction and initiation b) Comparative diagram

Fig. 2. Pressure wave distribution at T-junction – 1:1 model: same time closing of both branches

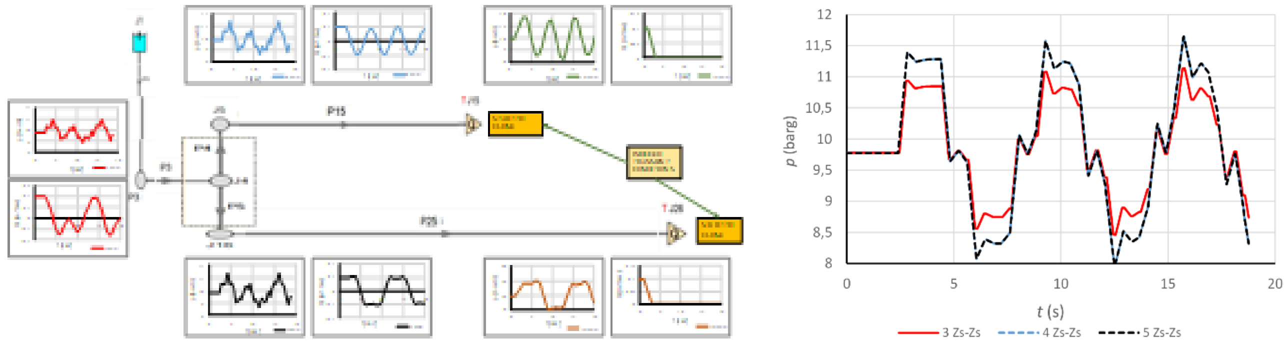

a) Pressure wave distribution at T-junction and initiation b) Comparative diagram

Fig. 3. Pressure wave distribution at T-junction – 1:2 model: same time closing of both branches

For the 1:1 model, the two positive pressure waves from the branches model propagate toward the T-junction and arrive simultaneously where they are superimposed in a more intense pressure increase due to constructive interference. The pressure wave is distributed to the supply pipeline with reduced amplitude because it propagates in the opposite direction of the water velocity, causing partial cancellation and energy dissipation.

For the 1:2 model, in the T-junction, the positive pressure waves from the shorter branch arrives earlier due to the reduced propagation path and its influence is transmitted to the longer branch. At the same time, the pressure wave generated within the longer branch is still propagating toward the junction. The superposition of the two positive pressure waves occurs along the branch with higher length. This amplified wave then reflects back toward the T-junction, where its delayed arrival causes a secondary pressure rise.

Closing one of the branches, the other one is closed (no flow)

Transitional states in the pipe system in the T-junction zone under conditions of flow closure in one of the branches are given in Figure 4 for the 1:1 model and in Figure 5 and Figure 6 for the 1:2 model.

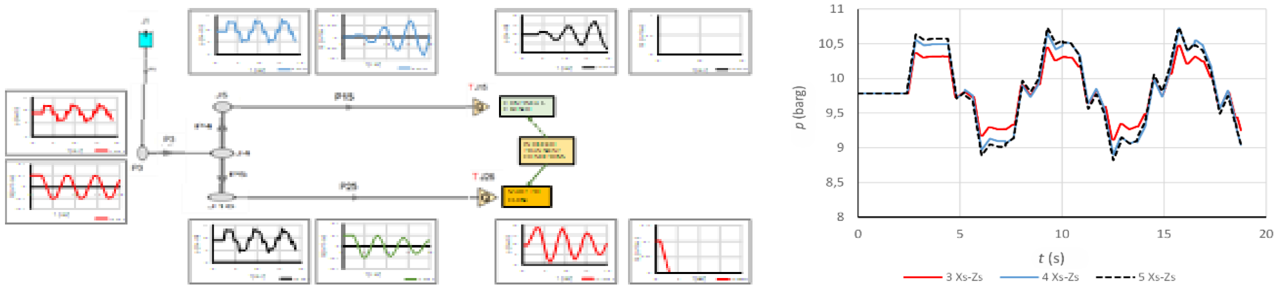

a) Pressure wave distribution at T-junction and initiation b) Comparative diagram

Fig. 4. Pressure wave distribution at T-junction – 1:1 model: closing one branch

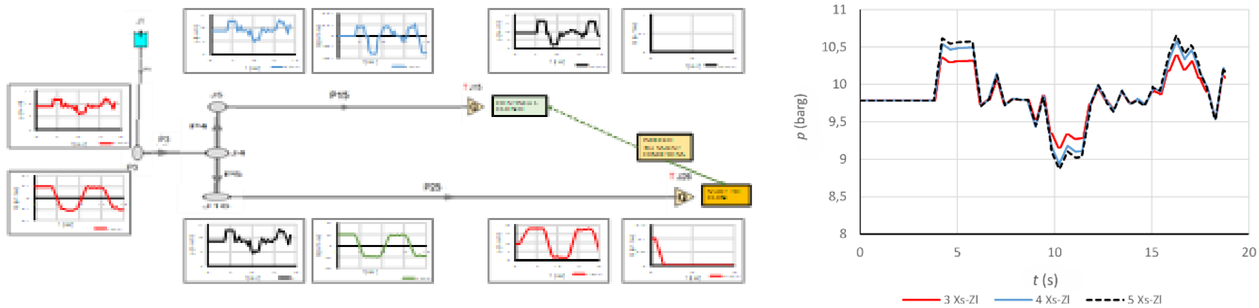

a) Pressure wave distribution at T-junction and initiation b) comparative diagram

Fig. 5. Pressure wave distribution at T-junction – 1:2 model: closing one branch (longer)

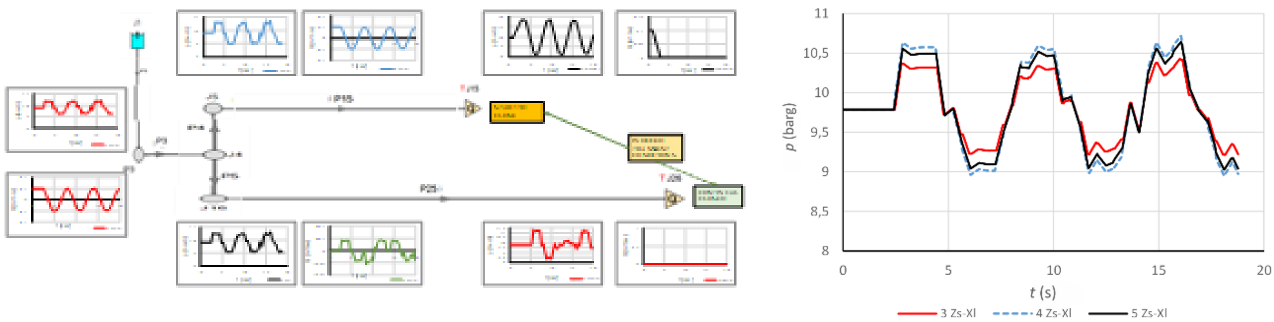

a) Pressure wave distribution at T-junction and initiation b) comparative diagram

Fig. 6. Pressure wave distribution at T-junction – 1:2 model: closing one branch (shorter)

For the 1:1 model, a positive pressure wave from only one of the branches enters the T-junction, which is partially transmitted into both the closed branch and the supply pipeline (section 3). Due to the hydraulic symmetry of the system, i.e. equal lengths, diameters and boundary conditions, the wave transmission pattern remains the same regardless of which branch is closed. The pressure wave transmitted through the T-junction has the highest intensity, as it carries the primary energy from the initiating disturbance.

For the 1:2 model, a positive pressure wave enters the T-junction from either the long or the short branch. In both cases, the wave is partially transmitted into the closed pressure branch and the supply pipeline (section 3). The pressure wave transmitted through the T-junction has the highest intensity, regardless of which branch closes. The difference in these two cases is in the periodicity of the transient modes, that is, due to the different branches lengths, the pressure wave propagation time is different resulting in variations in the timing of wave reflections and superpositions, which directly affect the frequency and phase of the pressure oscillations in the system.

The analysis of the branch with zero flow (closed end) given in Figure 7 shows that its length does not influence the initial phase of the transient response. However, as unsteady conditions develop over time, the difference in branch length leads to variations in the timing of wave reflections resulting in a non-uniform pressure distribution in the T-junction. The transient response of the pipeline system differs in the case of simultaneous closure of both branches and the closure of only one branch, as shown in Figure 8. When both branches are closed, the pressure wave intensity at the T-junction is higher due to the superposition of compression waves arriving from both sides. In contrast, closing only one branch results in a lower pressure peak, as the wave energy is not reinforced by a second incoming wave.

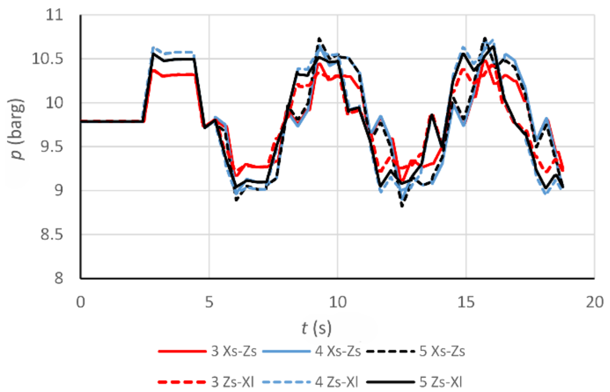

Fig. 7. Comparative diagram of pressure wave distribution at T-junction – 1:1 model and 1:2 model: closing one branch (shorter)

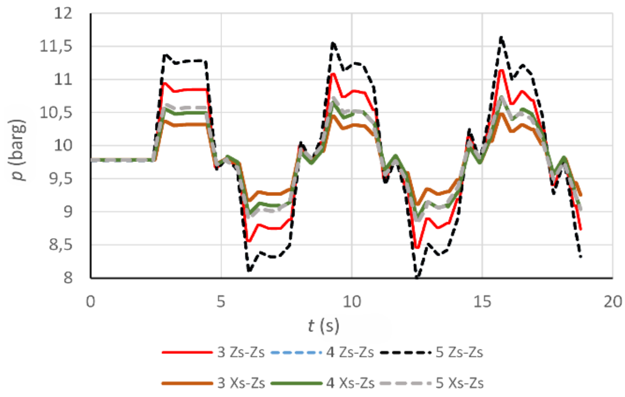

Fig. 8. Comparative diagram of pressure wave distribution at T-junction – 1:1 model: closing one branch vs. closing both branches

Effects of a negative pressure wave

Unsteady flow with a negative pressure wave is ensured by opening the parallel branches, that is, establishing a flow in the branch. The cases of pressure distribution in the T-junction during the simultaneous opening of the parallel branches and the case when the flow is established only in one branch while the other is without flow (closed) are considered.

Simultaneous opening of the branches

The transient states in the pipe system in the T-junction zone under conditions of simultaneous opening of the flow in the branches are given in Figure 9 and Figure 10.

For the 1:1 model, the two negative pressure waves (rarefaction waves) from the branches arrive simultaneously at the T-junction, where they are superimposed in a more intense increase in pressure, which is distributed to the supply pipeline with reduced intensity. The pressure distribution of the pressure wave towards the supply pipeline (section 3) is of reduced amplitude because it propagates against the direction of the water velocity which leads to partial attenuation due to momentum opposition and energy dissipation.

For the 1:2 model, in the T-junction the negative pressure wave from the shorter branch arrives first due to its shorter propagation path and its influence is transmitted to the longer branch. The superposition of the two negative pressure waves occurs along the length of the longer pipe and that effect is perceived in the T-junction after a delay.

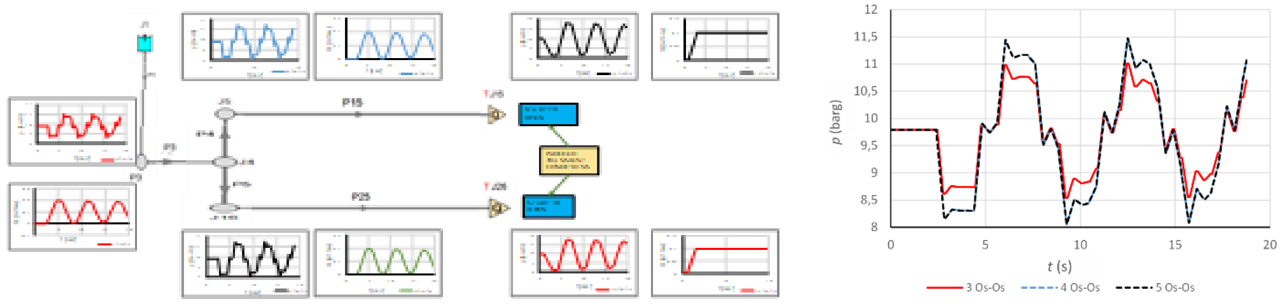

a) Pressure wave distribution at T-junction and initiation b) Comparative diagram

Fig. 9. Pressure wave distribution at T-junction – 1:1 model: opening at same time both branches

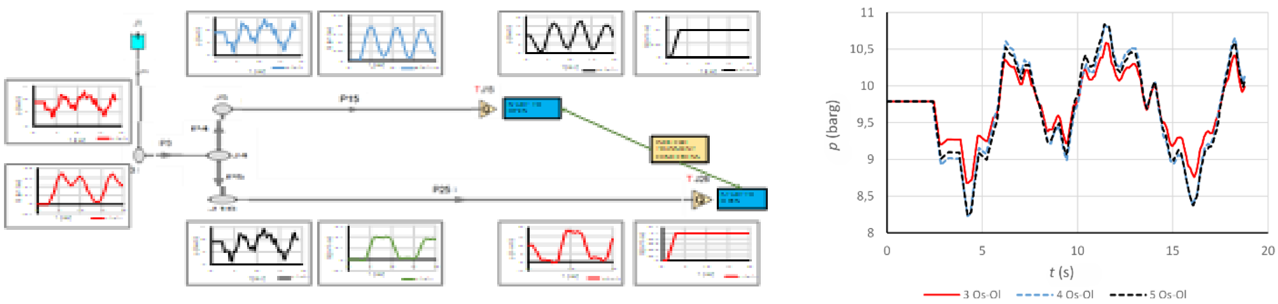

a) Pressure wave distribution at T-junction and initiation b) Comparative diagram

Fig. 10. Pressure wave distribution at T-junction – 1:2 model: opening at same time both branches

Opening one of the branches, the other is closed (no flow)

The transient states in the pipe system in the T-junction zone under conditions of flow opening in one branch are given in Figure 11 for the 1:1 model and in Figure 12 and Figure 13 for the 1:2 model.

For the 1:1 model, a negative pressure wave from only one of the branches enters the T-junction, which is transmitted to the closed branch and the supply pipeline (section 3). The calculations showed that due to the hydraulic symmetry of the system, the same diagram is obtained for the transmission of the negative pressure wave during the transient states, regardless of which of the branches is opened. The pressure wave transmitted through the T-junction has the highest amplitude.

For the 1:2 model, a negative pressure (rarefaction) wave is applied to the T-junction from either the long or the short branch. In both cases, the negative pressure wave is transmitted to the closed branch and the supply pipeline (section 3).

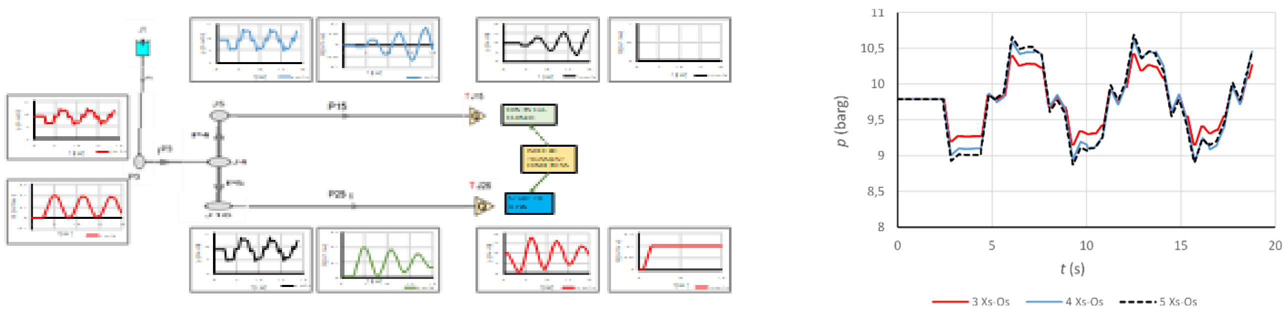

a) Pressure wave distribution at T-junction and initiation b) Comparative diagram

Fig. 11. Pressure wave distribution at T-junction –1:1 model: opening at one branch

a) Pressure wave distribution at T-junction and initiation

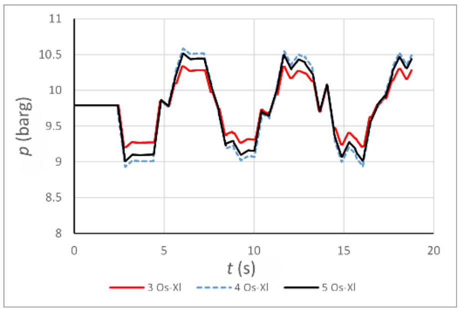

b) Comparative diagram

Fig. 12. Pressure wave distribution at T-junction – 1:2 model: opening one branch (shorter)

a) Pressure wave distribution at T-junction and initiation

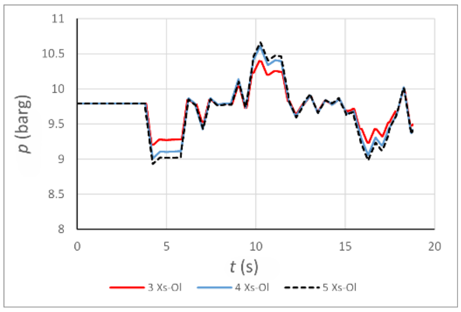

b) Comparative diagram

Fig. 13. Pressure wave distribution at T-junction – 1:2 model: opening one branch (longer)

The results in Figure 14 show that the pressure wave transmitted through the T-junction has the highest intensity, which is the same regardless of which branch opens. The difference in these two cases is in the periodicity of the transition modes, that is, due to the unequal lengths of the branches, the pressure wave propagation time differs, leads to variations in the period and phase of pressure wave reflections and superpositions throughout the system.

The transient conditions in the pipeline in the case of simultaneous opening of both branches and opening of only one branch shows a difference in the pressure wave intensity. Figure 15 shows the wave amplitude is greater in the case of opening both branches due to the superposition of rarefaction waves from both sides at the T-junction.

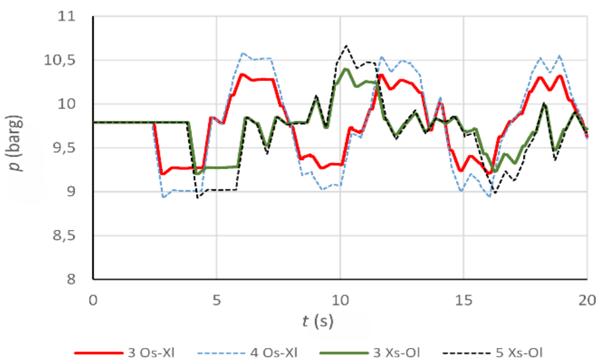

Fig. 14. Comparative diagram of pressure wave distribution at T-junction – 1:2 model: opening one branch, shorter vs. longer

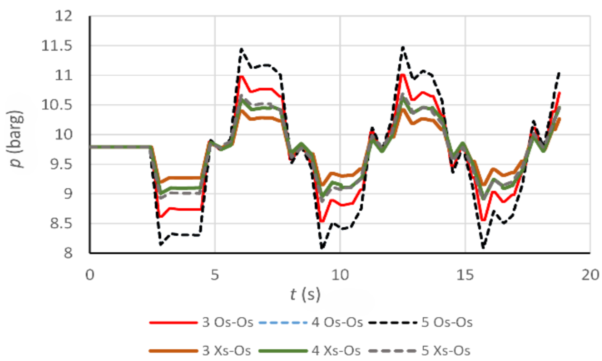

Fig. 15. Comparative diagram of pressure wave distribution at T-junction – 1:1 model: opening one branch vs. opening both branches

Effects of positive and negative pressure wave simultaneously

The transient states and the pressure wave distribution in the case of inducing a positive and negative pressure wave in the T-junction zone are given in Figure 16 for the 1:1 model and in Figure 17 and Figure 18 for the 1:2 model.

From the results obtained for the 1:1 model, where the positive and negative pressure waves arrive simultaneously in the T-junction, it is concluded that the pressure wave transmitted to the supply pipe is minimal due to the interference from the branches.

From the results obtained for the 1:2 model, where the positive and negative pressure waves do not arrive simultaneously in the T-junction, the transient states shape depends on which pressure wave (positive or negative) will arrive first at the T-junction.

As shown in Figure 17b, a positive pressure wave initially occurs in the T-junction transmission system, while in Figure 18b, a negative pressure wave is observed first. The transition modes that are reached under these conditions have the same magnitude and period, but they are of opposite signs, forming mirror-image responses in terms of the unsteady flow dynamics.

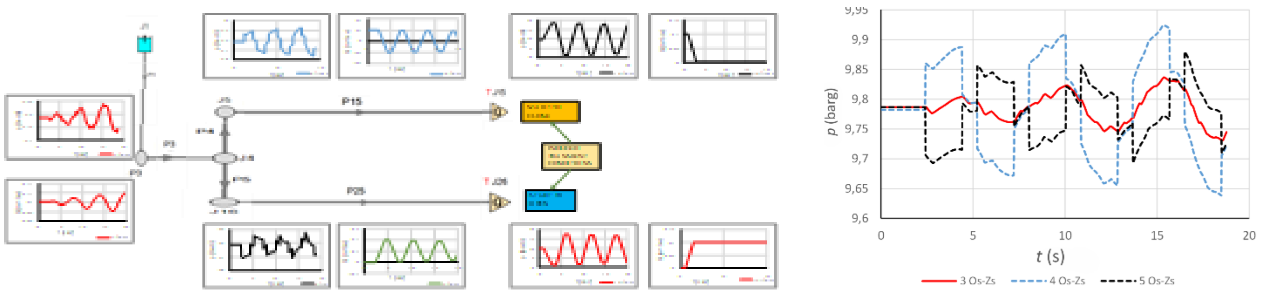

a) Pressure wave distribution at T-junction and initiation b) Comparative diagram

Fig. 16. Pressure wave distribution at T-junction – 1:1 model: opening/closing of branches at same time

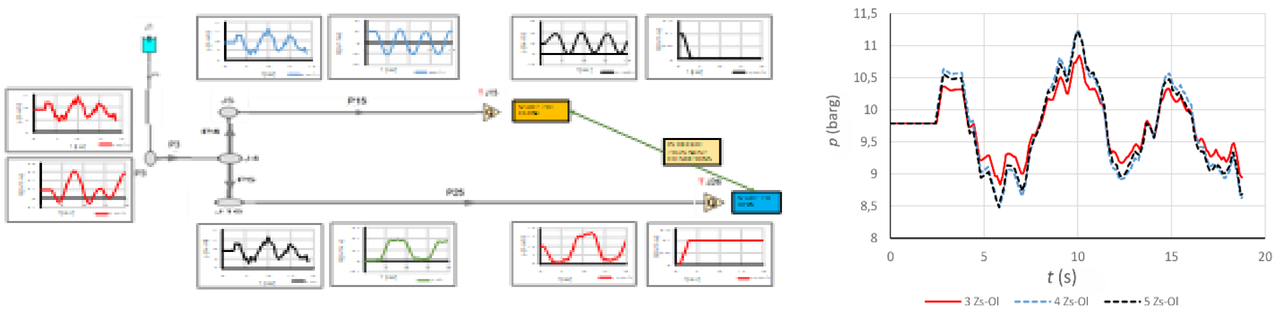

a) Pressure wave distribution at T-junction and initiation b) Comparative diagram

Fig. 17. Pressure wave distribution at T-junction –1:2 model: opening (longer) and closing (shorter) of branches at same time

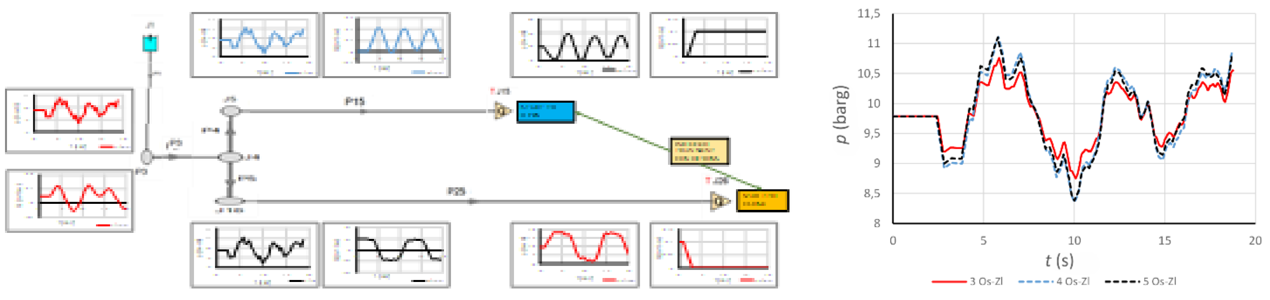

a) Pressure wave distribution at T-junction and initiation b) Comparative diagram

Fig. 18. Pressure wave distribution at T-junction –1:2 model: opening (shorter) and closing (longer) of branches at same time

The simultaneous presence of a positive and negative pressure wave in the T-junction has the effect of reducing the pressure increase that is transmitted through the inlet pipe (Figure 19), while in case of non-simultaneous presence of a positive and negative pressure wave in the T-junction, the transfer of pressure to the inflow pipe (press 3) is the same as if when closing only one branch (the shorter one), Figure 20.

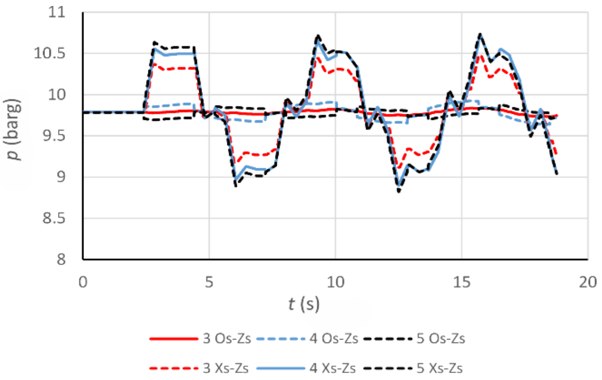

Fig. 19. Comparative diagram of pressure wave distribution at T-junction 1:1 model: closing one branch vs. closing/opening regime

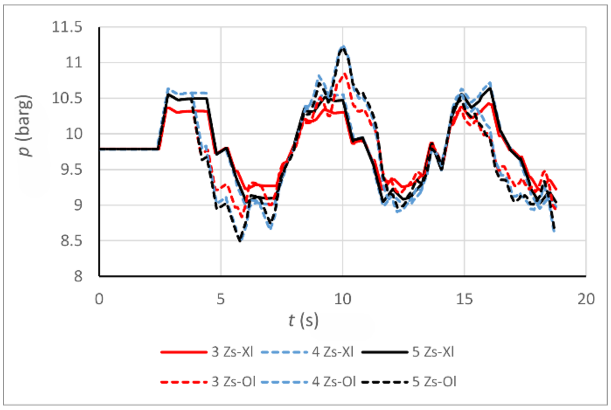

Fig. 20. Comparative diagram of pressure wave distribution at T-junction – 1:2 model: closing one branch (shorter) vs. closing/opening regime

CONCLUSION

The effects of superimposing pressure waves and their transmission through the T-junction are presented. A T-junction, i.e., a nodal point with three branches, is considered.

When pressure waves from both branches (positive or negative) arrive simultaneously at the T-junction, superposition occurs, leading to a more intense pressure response at the junction compared to cases where a wave enters from only one branch. In all scenarios, the transmitted wave into the supply pipeline (section 3) consistently exhibits the highest amplitude, whether it is a compression or rarefaction wave, due to the direct energy transfer from the initiating disturbance. When pressure waves originate from branches of unequal lengths, the arrival times and reflection phases differ, but the maximum transmitted wave intensity at the T-junction remains the same due to the hydraulic symmetry of the system. However, the timing and periodicity of the transient regime vary. Simultaneous closure or opening of both branches generates higher pressure amplitudes in the T-junction due to the interaction of waves from both sides. In contrast, closing or opening only one branch results in lower wave intensity because of absence of superposition. The system also shows that compression and rarefaction waves produce transient regimes of the same amplitude and frequency, but with opposite pressure signs.

The knowledge gained through the analyzed variant conditions is only an indicator of the need for a more detailed definition of the transitional regimes in a pipeline, and the same can be used in the design of pipelines and for the protection of pipelines from uncontrolled pressure increase/decrease occurrence.

REFERENCES

[1] Chaudhry, M. H. (1979): *Aplied Hydraulic Transients*, Van Nostrand Reihold Company.

[2] Zaruba, J. (1993): *Water Hammer in Pipe-Line Systems*, 1st Edition, Volume 43, ELSEVIER.

[3] Elbashir, M. A. M., Amoah, S. O. K. (2007): *Hydraulic transient in a pipeline using computer model to calculate and simulate transient*, Master thesis, Division of Water Resources Engineering, Lund University, Sweden.

[4] Nikodijević, M. D. (2021): *Nestacionarna strujanja u sistemima za transport tečnosti i njihova zaštita*, PhD thesis, University if Niš, Faculty of Mechanical Engineering in Niš, Serbia.

[5] Machalińska-Murawska J., Szydłowski, M. (2013): Lax-Wendroff and McCormack schemes for numerical simulation of unsteady gradually and rapidly varied open channel flow, *Archives of Hydro-Engineering and Environmental Mechanics* **60**, No. 1–4, pp. 51–62.

[6] Pal, S., Hanmaiahgari, P. R., Karney, B. W. (2021): An overview of the numerical approaches to water hammer modelling: The ongoing quest for practical and accurate numerical approaches, *Water* **13** (11), 1597. https://doi.org/10.3390/w13111597

[7] Henclik, S. (2018): Analytical solution and numerical study on water hammer in a pipeline closed with an elastically attached valve, *Journal of Sound and Vibration*

417, pp. 245–259.
https://doi.org/10.1016/j.jsv.2017.12.011

[8] Prica, S., Stevanović, V., Maslovarić, B. (2018): Numerical simulation of condensation induced water hammer, *Proceedings of ICONE12-49404*, pp. 791–795. https://doi.org/10.1115/ICONE12-49404

[9] Sam Ani, H. M. V, Khayatzadeh, A. (2002): Transient flow in pipe networks, *Journal of Hydraulic Research* **40** (5), 637–644. https://doi.org/10.1080/00221680209499908

[10] Kandil, M., El-Sayed, T. A., Kamal, A. M. (2024): Unveiling the impact of pipe materials on water hammer in pressure pipelines: an experimental and numerical study, *Scientific Reports* **14.**, https://doi.org/10.1038/s41598-024-80853-w

[11] Toumi, A., Sekiou F. (2024): Optimal valve closing law for improved water hammer control: a case from a water supply pipeline in Guelma, Algeria, *AQUA – Water Infrastructure, Ecosystems and Society* **73** (2), 200–216. https://doi.org/10.2166/aqua.2024.265

[12] Wood, D. J., Lingireddy, S., Boulos, P. F., Karney, B. W., McPherson, D. L. (2005): Numerical methods for modeling transient flow in distribution systems, *Journal AWWA* **97** (7), 104–115.

Mechanical Engineering – Scientific Journal, Vol. **43,** No. 1, pp. 17–22 (2025)
Number of article: 689
Received: May 13, 2025
Accepted: May 28, 2025
In print: ISSN 1857–5293
On line: ISSN 1857–9191
UDC: 621.941.013/.015:620.179.1
https://doi.org/10.55302/MESJ2543161c

Original scientific paper

EXPERIMENTAL ANALYSIS OF THE INFLUENCE OF PROCESS PARAMETERS ON CYLINDRICITY IN TURNING PROCESS

Marija Cvetkovska, Dragana Stamenkova, Anastasija Lefkova, Ema Vasileska, Ognen Tuteski, Boban Kusigerski, Gligorče Vrtanoski

Faculty of Mechanical Engineering, "Ss. Cyril and Methodius" University in Skopje, P.O.Box 464, MK-1001 Skopje, Republic of North Macedonia
ema.vasileska@mf.edu.mk

A b s t r a c t: Cylindrical parts produced through turning often demand certain form tolerances such as cylindricity to ensure proper function, reliability, and performance. As manufacturing shifts toward higher accuracy and sustainability, understanding how process parameters influence cylindricity becomes increasingly essential. This study presents an experimental analysis of the influence of three fundamental cutting parameters – depth of cut, feed rate, and spindle speed – on the cylindricity of parts produced under dry turning conditions. The experiments were performed on steel E335 using a full-factorial design with parameters varied at two levels. Cylindricity was measured on each machined part and statistically analyzed to evaluate individual effects and interactions of the parameters. Results show that all three parameters significantly affect cylindricity, with spindle speed exhibiting the highest statistical influence. Higher spindle speeds were associated with improved cylindricity, while increased feed rate and depth of cut tended to degrade form accuracy. A regression model was fitted to the experimental data to quantify the influence of each parameter and predict cylindricity deviations based on cutting conditions. The findings align with recent literature and offer practical insights for optimizing dry turning operations to achieve higher geometric precision.

Key words: turning process; design of experiment; regression analysis; cylindricity; process parameters

ЕКСПЕРИМЕНТАЛНА АНАЛИЗА НА ВЛИЈАНИЕТО НА ПАРАМЕТРИТЕ НА ПРОЦЕСОТ ВРЗ ЦИЛИНДРИЧНОСТА ПРИ СТРУЖЕЊЕ

А п с т р а к т: Ротациони делови добиени со стружење често бараат строги толеранции на форма како што е цилиндричност. Со стремежот на индустријата кон поголема точност и одржливост, сè поважно станува разбирањето на влијанието на параметрите на процесот врз цилиндричноста. Во овој труд експериментално се испитува влијанието на три параметри – длабочината на режење, поместот и бројот на вртежи на парчето – врз цилиндричноста добиена при стружење без користење на разладно средство. Експериментите се изведени на челик E335, користејќи сефакторен експеримент со менување на параметрите на две нивоа. Статистичката анализа покажа дека сите три параметри значително влијаат врз цилиндричноста, при што најголемо влијание има бројот на вртежи. Поголемиот број на вртежи доведува до помала вредност на цилиндричноста, додека зголемениот помест и длабочината на режење резултираат со поголема вредност. Регресионен модел беше искористен за да се моделира цилиндричност врз основа на параметрите на режење. Добиените резултати се во согласност со литературата и придонесуваат кон оптимизирање на процесот на стружење без разладно средство.

Клучни зборови: стружење; дизајн на експеримент; регресиона анализа; цилиндричност; процесни параметри

1. INTRODUCTION

Turning is one of the most widely used manufacturing processes for producing cylindrical parts with high precision and repeatability. Critical components, such as automotive shafts and aerospace pins, achieve their cylindrical form through turning operations, which reliably create axisymmetric surfaces [1, 2]. The importance of turning is to shape parts to the desired dimensions but also to achieve the required geometric accuracy to ensure proper function. In particular, cylindrical parts often dmand form tolerances such as cylindricity to meet quality and performance requirements [3].

Achieving high tolerance of cylindricity in turned parts can be challenging because many factors in the turning process can induce form errors. Machine tool imperfections (e.g., spindle misalignment or bed deflection) and tool wear can contribute to deviations from ideal geometry [4]. On the process side, the cutting parameters used in a lathe have a strong influence on the resulting form of the workpiece [5], as well as on its surface roughness [6]. These parameters determine the cutting forces, temperatures, and dynamics during material removal, all of which affect how closely the part adheres to a true cylindrical shape. Researchers have found that controlling cylindricity is more complex than controlling surface roughness, due to interactions between multiple inputs in turning [7]. In particular, an aggressive combination of parameters can lead to excessive tool deflection or vibration, resulting in deviations such as out-of-roundness or taper along the length of the part. Selecting optimal parameters can minimize such errors and yield near-ideal cylindrical surfaces. Numerous studies in the literature have investigated how turning parameters impact form accuracy of metal components [8–11]. A consistent finding across the literature is that the most influential parameters affecting cylindricity are the feed rate, spindle speed, and depth of cut. For example, Patel et al. reported that in dry turning of Al 7075 alloy, feed rate had the most significant impact on both circularity and cylindricity errors due to its strong influence on cutting force and vibration, followed by depth of cut and cutting speed [12]. Rafai and Islam concluded that feed rate, cutting speed, and depth of cut were influencing factors for diameter error and circularity in the dry turning of AISI 4340 [13].

In recent years, the rise of new industrial revolutions has enabled the adoption of advanced modeling techniques, including artificial intelligence methods [14, 15]. For instance, response surface methodology and genetic algorithms have been used to optimize cutting conditions and enhance cylindricity [16]. A recent study using artificial neural networks to model turning of aluminum AA7075 confirmed that the best results for overall surface integrity were obtained with a combination of low feed rate and high cutting speed [17].

Another key aspect in manufacturing is the machining environment: whether cutting is done dry or with coolant. Although dry turning has environmental and economic benefits, eliminating the need for cutting fluid disposal and reducing health hazards; the absence of coolant can result in higher cutting zone temperatures and faster tool wear, which potentially impact surface quality and accuracy [18]. The literature suggests that a balanced setting of lower feed rate, adequate (not very high) cutting speed, and small value of depth can yield the best cylindricity in dry turning of metals, even though it shows to have a negative effect on the tool wear [19].

Given the importance of turning for cylindrical components and the critical role of cylindricity in part functionality, understanding how cutting parameters affect this tolerance is of high practical relevance. Therefore, the current study extends this body of knowledge by experimentally analyzing the effect of depth of cut, feed rate, and spindle speed on the cylindricity of lathe-turned steel workpieces made of steel E335 under dry cutting conditions. In this work, a design of experiments approach is employed to analytically vary the three cutting parameters and measure the resulting cylindricity of the machined parts. The findings contribute to a better understanding of how cutting conditions affect cylindricity and provide insights for optimizing lathe operations to achieve higher machining accuracy.

2. EXPERIMENTAL EQUIPMENT

The experiments were carried out on a conventional lathe manufactured by Prvomajska (Croatia, model TVP 250). The lathe operates on a three-phase power supply at 50 Hz, with a rated power of 11.2 kW. The nominal current of the lathe is 23 A, increasing to 25 A during high-speed operations for stable performance across the cutting conditions.

A PSSNR2525M12 tool holder (Pafana, Poland) with a SNMG120408-MF insert (Sandvik Coromant, Sweden) were employed. The selected insert has a nose radius of 0.8 mm and a negative rake geometry, in order to enhance cutting stability and efficient chip removal while maintaining surface integrity and dimensional accuracy.

Cylindricity measurements of the machined parts were performed using a Mitutoyo Roundtest RA-400, shown in Fig. **1**. The instrument is capable of assessing roundness, cylindricity, and flatness among others. The RA-400 is equipped with a precise G-series digital servo motor, auto-focus functionality, and a maximum resolution of 65 nanometers. For collecting data for characterization of the surface form and cylindricity estimation, measurements were conducted along 20 mm length of each workpiece using a spiral scanning pattern.

Fig. 1. Mitutoyo Roundtest RA-400 instrument used for cylindricity measurements

3. EXPERIMENTAL DESIGN

A full-factorial experimental design was employed to investigate the influence of the machining parameters on cylindricity during dry turning process. The tests were performed on structural steel E335, characterized by controlled impurities with maximum values of P ≤ 0.045%, S ≤ 0.045%, and N ≤ 0.012%, and a carbon content around 0.17–0.20%, according to EN 10025-2:2004.

Three process parameters were used in the study: depth of cut (a_p), spindle speed (n), and feed rate (f_n), because as aforementioned these are widely recognized in the literature as the most significant factors affecting geometrical accuracy in turning processes. Each parameter was varied at two levels (low and high), with the corresponding values presented in Table 1. A full-factorial 2^3 experimental design was employed to evaluate all possible combinations of these factors, to make a comprehensive analysis of their individual contributions and possible interactions on cylindricity deviations.

Table 1

Variable factors with their levels employed in the full-factorial experiment

Factor	Low level	High level
Depth of cut, a_p (mm)	0.5	1.0
Feed rate, f_n (mm/rev)	0.08	0.315
Spindle speed, n (rpm)	100	400

Each experimental combination was replicated three times for statistical reliability of the results. As a result, the total number of experiments conducted was 24. The sequence of the experiments was randomized to mitigate external influences.

4. RESULTS AND ANALYSIS

Cylindricity was measured for each machined sample in the experimental trials. The data were analyzed using Minitab Statistical Software. Fig. **2** displays the individual values of cylindricity as a function of the values of the feed rate, depth of cut, and spindle speed. Each data point represents a single experimental observation, with symbol shapes distinguishing the two spindle speed levels: red squares for 400 rpm and blue circles for 100 rpm. The plot shows that the higher level of spindle speed (400 rpm) leads to lower cylindricity values, indicating better form accuracy. In contrast, lower spindle speeds (100 rpm) are resulting with greater deviations from ideal cylindricity. Moreover, an increase in feed rate and depth of cut tends to result in an increase in cylindricity deviation, suggesting that both parameters have a negative impact on form precision when elevated.

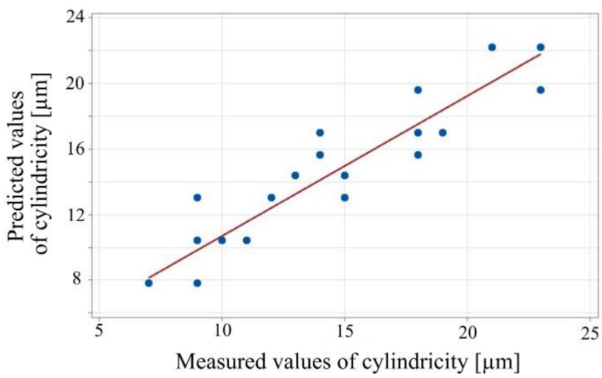

Fig. 2. Individual value plot of cylindricity values from the experiment samples as a function of process parameters

These results are confirmed by various literature works. Studies report that for most materials tested, increasing the cutting speed leads to reduced cylindricity error in turning operations [20]. In practical terms, using a faster spindle speed (within machine and tool limits) generally improves geometric accuracy. It's worth noting that the influence of speed on cylindricity is often less pronounced than feed or depth effects [21]. Studies confirm that a higher feed rate results in a thicker chip per revolution and greater cutting force, which tends to deflect the tool or workpiece and produce a less perfectly cylindrical shape [22, 23] Furthermore, studies show a clear trend of greater depth of cut leading to larger cylindricity error, since the cross-sectional area of the cut is increased, raising cutting forces and potential deflection [24, 25].

These conclusions are further confirmed by the main effects plot of the measured cylindricity values, shown in

Fig. **3**, which illustrates that increasing depth of cut and feed rate leads to worsening of the geometrical accuracy, resulting in higher cylindricity deviations. In contrast, increasing spindle speed has a positive influence, resulting in improved cylindricity and enhanced form accuracy.

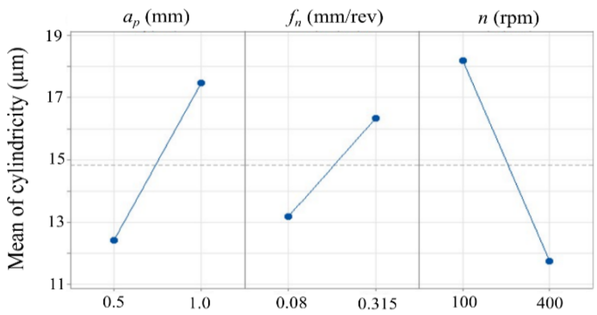

Fig. 3. Main effects plot of investigated process parameters on cylindricity

From the interaction plot for cylindricity (Fig. **4**), it can be observed that no significant interactions are present between the investigated cutting parameters, as indicated by the approximately parallel lines in each subplot. The lack of strong interaction effects suggests that each factor influences cylindricity independently, without notable interaction effects on the output variable.

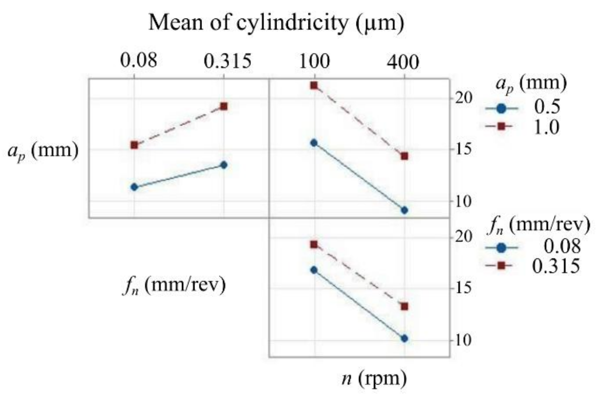

Fig. 4. Interaction plot of investigated process parameters on cylindricity

The ANOVA analysis provides a statistical assessment of the significance of each cutting parameter on cylindricity, and the results by this analysis are given in Table 2. The P-values shown in the table are rounded on three decimal places. As shown, all three factors have statistically significant effects on cylindricity, with P-values less than 0.05. Among them, the results show that spindle speed exhibits the highest influence, as indicated by the largest F-value (61.80), followed by depth of cut (F-value equal to 39.20), and then feed rate (F-value equal to 9.86). This finding is consistent with previous studies showing that spindle speed can have a dominant effect on form accuracy, since spindle speed governs the dynamic behavior of the machining system, influencing factors such as tool–workpiece interaction frequency, vibration tendencies, and thermal stability [26].

Furthermore, the interaction terms between the three factors did not show a significant effect based on the P-values being higher than the threshold value for statistical significance of 0.05. The findings support the trends observed in the main effects and interaction plots and align well with published literature on the influence of cutting parameters on form accuracy. From the ANOVA results all investigated factors will be included in the regression model. Since the results show no significant interactions between the factors, the regression equation will be formulated in linear form with first-degree terms.

T a b l e 2.

Results of ANOVA for cylindricity

Source	F-value	P-value
a_p (mm)	39.20	0.000
f_n (mm/rev)	9.86	0.005
n (rpm)	61.80	0.000

The results of the linear regression analysis showed the following predictive equation for cylindricity (μm):

$$C = 10.46 + 10{,}43 \cdot a_p + 11.13 \cdot f_n - 0.02183 \cdot n \quad (1)$$

where: C is cylindricity, a_p is the depth of cut (mm), f_n is the feed rate (mm/rev), and n is the spindle speed (rpm). The model demonstrated a strong fit, with a coefficient of determination (R^2) of 85.37%, indicating that 85.37% of the variation in cylindricity is explained by the selected cutting parameters. The positive coefficients for a_p and f_n confirm their increasing effect on cylindricity deviation, while the negative coefficient for n supports the observation that higher spindle speeds reduce cylindricity error.

Fig. **5** presents a scatter plot of the predicted values versus the actual cylindricity measurements, providing a visual assessment of the regression model's accuracy. The red line represents the ideal case where predicted values perfectly match the actual data. The distribution of points closely follows this line, indicating a strong correlation between the predicted and observed values. While some scatter and minor deviations from the line are visible, the overall trend confirms that the regression model effectively captures the relationship between the process parameters and cylindricity, supporting the reliability of the linear regression model.

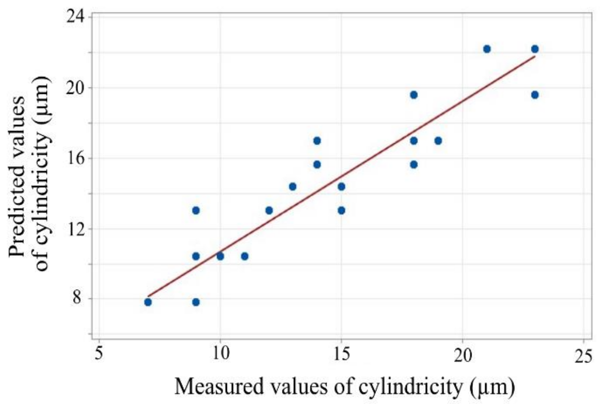

Fig. 5. Scatter plot results of the fitted regression model for cylindricity

5. CONCLUSION

This study investigated the influence of the three most significant cutting parameters: depth of cut, feed rate, and spindle speed, on the cylindricity of steel parts produced through rough dry turning on a conventional lathe. A full-factorial experimental design (2^3) was employed. Statistical analysis was conducted using Minitab software to quantify the individual and combined effects of the process parameters on the measured cylindricity. The findings showed that all three cutting parameters significantly affect cylindricity, with spindle speed as the most influential factor. Increasing spindle speed resulted in improved cylindricity, demonstrating better form accuracy under higher rotational speeds. Depth of cut and feed rate both had a positive correlation with cylindricity error, with larger values increasing cylindricity deviations. No significant interactions between factors were observed in the interaction plots. Therefore, first-degree linear regression model was fitted to correlate the cylindricity output as a function of the three process parameters, which resulted with a high accuracy of R^2 = 85.37%. These findings emphasize the importance of optimizing machining parameters to enhance precision and quality in turning applications.

For future research, the investigation will be expanded to include different materials and tool geometries to generalize the findings. Incorporating in-process monitoring methods, such as force or vibration sensors, can also provide deeper insights into the mechanisms affecting cylindricity and enable the development of adaptive control strategies.

REFERENCES

[1] You, S. H., Lee, J. H., Oh, S. H. (2019): A study on cutting characteristics in turning operations of titanium alloy used in automobile, *International Journal of Precision Engineering and Manufacturing*, Vol. **20**, No. 2, pp. 209–216. DOI: 10.1007/s12541-019-00027-x

[2] Tajne, A., Gupta, T. V. K., Ramani, H., Joshi, H. (2024): A critical review on the machinability aspects of nickel and cobalt based superalloys in turning operation used for aerospace applications, *Advances in Materials and Processing Technologies*, Vol. **10**, No. 2, pp. 833–866. DOI: 10.1080/2374068X.2023.2185850

[3] Kundrák, J., Karpuschewski, B., Gyani, K., Bana, Y. (2007): Accuracy of hard turning, *J Mater Process Technol*, Vol. **202**, No. 1, pp. 328–338. DOI: https://doi.org/10.1016/j.jmatprotec.2007.09.056

[4] Akhavan Niaki, F., Mears, L. (2017): A comprehensive study on the effects of tool wear on surface roughness, dimensional integrity and residual stress in turning IN718 hard-to-machine alloy, *J Manuf Process*, Vol. **30**, pp. 268–280, DOI: https://doi.org/10.1016/j.jmapro.2017.09.016

[5] Khan, A., Saghir, Q., Raza, A. (2019): Determining the effects of selected cutting parameters on circularity and cylindricity in turning operations for steel 4140 using Taguchi methods, *Introduction and Literature Review*.

[6] Tomov, M., Gečevska, V., Vasileska, E. (2022): Modelling of multiple surface roughness parameters during hard turning: A comparative study between the kinematical-geometrical copying approach and the design of experiments method (DOE). *Advances in Production Engineering and Management*, Vol. **17**, No. 1, pp. 75–88, DOI: 10.14743/apem2022.1.422

[7] Rafai, N., Islam, N. (2998): An investigation into dimensional accuracy and surface finish achievable in dry turning, *Machining Science and Technology*, Vol. **13**, pp. 571–589, DOI: 10.1080/10910340903451456

[8] Rangappa, R. *et al.* (2022): Coaxiality error analysis and optimization of cylindrical parts of CNC turning process, *The International Journal of Advanced Manufacturing Technology*, Vol. **120**, no. 9, pp. 6617–6634. DOI: 10.1007/s00170-022-09184-2

[9] Singaravel, B., Marulaswami, C., Selvaraj, T. (2016): Analysis of the effect of process parameters for circularity and cylindricity errors in turning process, *Applied Mechanics and Materials*, Vol. **852**, pp. 255–259. DOI: 10.4028/www.scientific.net/AMM.852.255

[10] Masoudi, S., Esfahani, M. J., Jafarian, F., Mirsoleimani, S. A. (2023): Comparison the effect of mql, wet and dry turning on surface topography, cylindricity tolerance and sustainability, *International Journal of Precision Engineering and Manufacturing-Green Technology*, Vol. **10**, no. 1, pp. 9–21. DOI: 10.1007/s40684-019-00042-3

[11] Islam N., Pramanik, A. (2015): Effects of insert geometry and feed rate on quality characteristics of turned parts, *Journal of Advanced Manufacturing Systems*, Vol. **14**, pp. 149–166. DOI: 10.1142/S0219686715500109

[12] Manjunath Patel, G. C., Lokare, D., Chate, G. R., Parappagoudar, M. B., Nikhil, R., Gupta, K. (2020): Analysis and optimization of surface quality while machining high strength aluminium alloy, *Measurement*, Vol. **152**, p. 107337. DOI: https://doi.org/10.1016/j.measurement.2019.107337

[13] Rafai, N. H., Islam, M. N. (2009): An investigation into dimensional accuracy and surface finish achievable in dry turning, *Machining Science and Technology*, Vol. **13**, no. 4, pp. 571–589. DOI: 10.1080/10910340903451456

[14] Argilovski, A., Vasileska, E., Tuteski, O., Kusigerski, B., Jovanoski, B., Tomov, M. (2024): Bridging the gap: Qualitative comparative analysis of Industry 4.0 and Industry 5.0, *Mechanical Engineering-Scientific Journal*, Vol. **42**, no. 1, pp. 61–66. DOI: 10.55302/mesj24421061a

[15] Argilovski, A., Vasileska, E., Jovanoski, B. (2023): Enhancing manufacturing efficiency: a lean Industry 4.0 approach to retrofitting, *Mechanical Engineering Scientific Journal*, Vol. **41**, no. 2, pp. 123–129, DOI: 10.55302/mesj23412672123a

[16] Gupta, U., Ghorapade, V. U., Raju, G. A., Nandam, S. R. (2018): Mathematical modelling and optimisation of cylindricity form parameter in CNC turning using response surface methodology and genetic algorithm, *Mater Today Proc*, Vol. **5**, no. 9, Part 3, pp. 19985–19996, DOI: https://doi.org/10.1016/j.matpr.2018.06.365

[17] Trujillo, F. J., Martín-Béjar, S., Bañón, F., Andersson, T., Sevilla, L. (2025): Ann-based predictive model of geometrical deviations in dry turning of AA7075 (Al-Zn) alloy, *Measurement*, Vol. **243**, p. 116355, 5. https://doi.org/10.1016/j.measurement.2024.116355

[18] Dhar, N. R., Islam, M. W., Islam, S., Mithu, M. A. H. (2006): "The influence of minimum quantity of lubrication (MQL) on cutting temperature, chip and dimensional accuracy in turning AISI-1040 steel, *J Mater Process Technol*, Vol. **171**, no. 1, pp. 93–99, https://doi.org/10.1016/j.jmatprotec.2005.06.047

[19] Diniz, A. E., De Oliveira, J. A. (2004): Optimizing the use of dry cutting in rough turning steel operations, *Int J Mach Tools Manuf*, Vol. **44**, no. 10, pp. 1061–1067. https://doi.org/10.1016/j.ijmachtools.2004.03.001

[20] Zmarzły, P. (2020): Technological heredity of the turning process, *Tehnički vjesnik*, Vol. **27**, no. 4, pp. 1194–1203. DOI: 10.17559/TV-20190425150325

[21] Abas, M. *et al.* (2020): Experimental investigation and statistical evaluation of optimized cutting process parameters and cutting conditions to minimize cutting forces and shape deviations in al6026-t9, *Materials*, Vol. **13**, no. 19, pp. 1–21. DOI: 10.3390/ma13194327

[22] Choudhury, S. K. (2012): Effect of cutting parameters on cutting force and surface roughness during finish hard turning AISI52100 grade steel, *Procedia CIRP*, Vol. **1**, pp. 651–656. DOI: 10.1016/j.procir.2012.05.016

[23] Magdum, V., Naik, V. (2017): Investigating feed rate effect on cutting force of EN 8 turning, *Asian Review of Mechanical Engineering*, Vol. 6, pp. 8–12. DOI: 10.51983/arme-2017.6.1.2424

[24] Sztankovics, I., Wafae, E. M. (2024): Preliminary study on the cutting force and shape error in turning of X5CrNi18-10 shafts with small feed, *Journal of Production Engineering*, Vol. **27**, no. 2, pp. 21–28. DOI: 10.24867/JPE-2024-02-021

[25] Abas, M., *et al.* (2020): Experimental investigation and statistical evaluation of optimized cutting process parameters and cutting conditions to minimize cutting forces and shape deviations in al6026-t9, *Materials*, Vol. **13**, no. 19, pp. 1–21. DOI: 10.3390/ma13194327

[26] Sztankovics, I.. Pásztor, I. (2022): Shape error analysis of tangentially turned outer cylindrical surfaces, *Acta technica corviniensis – Bulletin of Engineering*, Vol. **15**, pp. 23–28.

Mechanical Engineering – Scientific Journal, Vol. **43,** No. 1, pp. 23–30 (2025)
Number of article: 690
Received: April 17, 2025
Accepted: May 10, 2025
In print: ISSN 1857–5293
On line: ISSN 1857–9191
UDC: 628.47.036(497.711)
https://doi.org/10.55302/MESJ2543123uz

Original scientific paper

EXPLORING THE FEASIBILITY OF CONSTRUCTION AND DEMOLITION WASTE RECYCLING IN SKOPJE THROUGH ANALYZING FOUR DIFFERENT SCENARIOS

Monika Uler-Zefikj[1], Dame Dimitrovski[1], Aleksandar Mančevski[2]

[1]*Faculty of Mechanical Engineering, "Ss. Cyril and Methodius" University in Skopje, P.O.Box 464, MK-1001 Skopje, Republic of North Macedonia*
[2]*Association 6th Star - Energy, Waste and Environment Department, Nikola Parapunov 41, 1000 Skopje, Republic of North Macedonia*
monika.uler-zefikj@mf.edu.mk

A b s t r a c t: Construction and demolition waste (CDW) accounts for 25–30% of the total waste generated in the EU. In North Macedonia, CDW management is primarily based on collection and landfilling by public communal enterprises, with operations not fully aligned with EU standards. CDW generation is estimated at 460,000–500,000 tons/year nationwide and 142,434–154,820 tons/year in Skopje. Four scenarios for CDW treatment in Skopje are proposed: Full Treatment (FT), Selected Treatment (ST), Selected Treatment with Mobile Equipment (STM), and Do Nothing. FT offers high material recovery but requires significant investment and has a 12.2 year ROI. ST has lower costs with over 2 years of execution time, while STM provides the best ROI with a 6 month implementation timeline. All scenarios contribute to reducing GHG emissions (18,031,840 kg CO_2-e) and lowering landfilling by 449,000 tons. Implementation would also yield socio-economic benefits including job creation, improved public awareness, and advancement toward a circular economy.

Key words: construction and demolition waste; collection; landfilling; recycling; scenarios

ИСТРАЖУВАЊЕ НА ИЗВОДЛИВОСТА НА РЕЦИКЛИРАЊЕ ГРАДЕЖЕН ОТПАД И ШУТ ВО СКОПЈЕ ПРЕКУ АНАЛИЗА НА ЧЕТИРИ РАЗЛИЧНИ СЦЕНАРИЈА

А п с т р а к т: Градежниот отпад и шут (ГОШ) сочинува 25–30% од вкупниот отпад генериран во ЕУ. Во Северна Македонија управувањето со ГОШ се базира главно на собирање и депонирање од страна на јавни комунални претпријатија, при што операциите не се целосно усогласени со стандардите на ЕУ. Генерираното количество ГОШ се проценува на 460.000–500.000 тони годишно на национално ниво и 142.434–154.820 тони годишно во Скопје. Предложени се четири сценарија за третман на ГОШ во Скопје: целосен третман (ЦТ), селективен третман (СТ), селективен третман со мобилна опрема (СТМО) и непроменето. ЦТ овозможува висок степен на обновување на материјали, но бара значителни инвестиции и има поврат на инвестиција (ROI) од 12,2 години. СТ има пониски трошоци со повеќе од 2 години за реализација, додека СТМО нуди најдобар ROI и се реализира за 6 месеци. Сите сценарија придонесуваат за намалување на стакленички гасови (18.031.840 kg CO_2-e) и намалување на депонираниот отпад за 449.000 тони. Имплементацијата носи и социо-економски придобивки – отворање работни места, подобрување на јавната свест и премин кон циркуларна економија.

Клучни зборови: градежен отпад и шут; собирање; депонирање; рециклирање; сценарија

1. INTRODUCTION

The Skopje region is located in the northern part of the country and shares a border with Kosovo. Internally, it borders the Polog, Southwest, Vardar, and Northeast regions. The population of the Skopje statistical region according to the 2021 census is 526,502 residents [1]. Skopje is the most populous region in the country even though it is the smallest, covering 7.3% of the total area of the Republic of North Macedonia.

According to the data from the State Statistical Office, the amount of generated municipal waste in the Skopje Region in 2022 was 174,404 tons from which collected were 172,288 tons or around 98.8%. From the total amount of generated municipal waste in the Republic of North Macedonia the collected amount in the Skopje Region was the greatest amounting in 28.4%. In terms of waste types, the largest quantity of collected waste was mixed municipal waste with 81.7%, while the smallest quantity was tire waste with 0.2% of the total collected municipal waste. The average composition of waste in the Skopje Region is given in Table 1. The largest amount of collected municipal waste (99.8%) is disposed of in landfills [2].

Table 1

The average composition of waste in the Skopje Region [3]

Waste type	Amount of municipal waste collected (tons)	Percentage of the total amount of municipal waste collected (%)
Paper	12,178	2.01
Glass	3,754	0.62
Plastics	13,063	2.16
Metal (iron, steel, aluminium)	2,302	0.38
Organic waste (food, leaves, etc.)	40,259	6.65
Textile	8,373	1.38
Tire	1,487	0.25
Mixed municipal waste	494,693	81.68
Other	29,531	4.88

Construction and demolition waste (CDW) represents one of the heaviest and largest waste streams generated in the EU, constituting approximately 25%–30% of the total waste generated [4]. CDW originates from the construction, repair, maintenance, and demolition of infrastructure, buildings, and structures. It consists of construction waste, demolition waste and excavation waste. Construction waste results from management practices on sites, such as surplus materials, sharp and damaged materials. Demolition waste is created from the demolition of existing structures/objects instead of opting for renovation. It often includes many mixed waste streams, which may also contain hazardous substances such as asbestos. And excavation waste typically consists of materials such as soil, excavated earth, and existing foundations removed during excavations for new construction. It may contain contaminated material depending on the previous use of the site [5]. Materials that are commonly included in construction and demolition waste are concrete, bricks, tiles, and ceramics; wood, glass, and plastic; asphalt mixes, tar, and tar products; metals (including their alloys); soil, stone, and excavated material with a backhoe; insulation materials and construction materials containing asbestos; construction materials with gypsum [6].

In the Republic of North Macedonia, the waste management system primarily relies on the collection and landfilling of waste. The services for waste collection, transportation, and landfilling are provided by public communal enterprises (PCEs). Waste disposal is managed by PCEs at the locations of regional municipal landfills. Operations at these locations are carried out on a controlled basis, but they still do not comply with EU requirements [7]. Understanding the management of construction and demolition waste is challenging, with difficulties related to data accuracy and reporting. According to the estimates of the National Waste Management Plan the generation of construction and demolition waste in North Macedonia ranges from 460,000 to 500,000 tons/year, whereas in Skopje ranges from 142,434 to 154,820 tons/year [8]. However, these estimates might be low compared to experiences in other countries. The quantities vary per capita, indicating different reporting methodologies. Estimated quantities in other countries range as follows:

- construction and demolition waste + excavation waste: 2.3 to 5.9 tons per capita annually,
- construction and demolition waste – excavation waste: 0.94 tons per capita annually [9].

Using these figures, the estimated quantity of generated construction and demolition waste in Macedonia (excluding excavation waste) should be around 1.95 million tons per year [8].

There was a planned acquisition of a facility for treatment of construction waste with a planned capacity of 90,000 tons/year. The facility was to receive and treat construction waste. Initially, the CDW was to be crushed, then separated into iron, cement, bricks, and other construction materials so that it can be reused. Part of it was for covering and compacting the layers of the new landfill, and the other part for building roads and similar constructions. The construction of the facility was expected to be completed no later than the end of 2017. However, this activity to this day has not been realized.

2. EXPERIMENTAL

Four scenarios are being considered for further management and treatment of waste from construction activities and construction debris in the Skopje Region. The scenarios developed in this chapter will serve for further analysis and evaluation based on pre-established criteria in the areas of technical and organizational improvement, economic feasibility, and environmental impact and greenhouse gas emissions. The scenarios are divided into two groups: three scenarios (TO DO) and one (DO Nothing) scenario. According to the general activities in the scenario, they are set as follows:

A). **Scenario 1:** *FT – Full Treatment*

A scenario involving automated separation, selection, crushing, and fractionation procedures, additional separation of crushed material (metal, paper, plastic, wood, glass, concrete, and stone aggregates), and creating a final product with high market value. This scenario assumes the establishment of practices that enable the full functionality of the waste management system in the part related to construction waste. Users will be provided with an accessible service for depositing construction waste. Large construction sites, as before, will be responsible for bringing construction waste from construction activities to the Drisla landfill using their own transport machinery. As an additional motivation, the Drisla landfill will offer a low subsidized price for depositing this type of waste, 200 MKD per ton, as opposed to the price of 680 MKD per ton for mixed municipal waste. In this scenario, waste separation and collection practices for construction waste and small reconstructions will be established in two ways.

1) *Micro and very small reconstructions*

For these reconstructions branded bags for construction waste are planned to be used. These branded bags (similar to IKEA's blue bags) with a carrying capacity of up to 50 kg will be sold at various locations in the city and will be available to citizens at a more favorable price. These bags are shown in Figure 1. Craftsmen or small construction firms performing reconstructions will be required to pack the construction waste from the reconstruction in such bags and leave it at the nearest location where the PCEs have containers or bins for waste collection. The disposal of these bags will be done on specified days of the week (different days for different parts of the city), and the location of disposal will need to be reported by phone to the PCEs.

Fig. 1. Bag for packaging CDW

This scenario predicts procurement of a truck for collecting this waste and equipment for loading the bags into the truck. PCEs will establish a collection unit for this waste and a pilot scheme for collecting and transporting waste to the Drisla landfill.

2) *Medium and large reconstructions*

In the case of slightly larger reconstructions where it's not possible to collect construction waste in bags, use of the services of PCEs is planned involving placing a large 5 m^3 container for waste disposal. Regarding waste treatment and the technologies envisaged for processing, this scenario proposes a complete treatment up to the production of a finished secondary product. Upon arrival at the Drisla landfill, it is foreseen to have pre-selection (depending on the type of waste) and automated selection of materials. This process involves a moving belt on which the waste is placed, a crusher for waste shredding, magnetic separation for magnetic metals, a blower for lighter waste elements, optical removal of visible waste (glass and plastic), additional crushing, and selection by fractions of different sizes. Equipment for concrete slabs made from secondary materials, separation for cushion material, and separation for tampon material are also part of the envisaged treatment process. The investment value of this scenario is estimated at 1,870,000 euros for equipment, and the necessary procedure for setting up and commissioning the equipment is estimated at 2.5 years (urban and technical technological projects, execution, supervision, and commissioning).

B) **Scenario 2:** *ST – Selected Treatment*

This scenario involves the initial separation of incoming materials by the staff at the Drisla landfill according to previously established procedures. It includes crushing pre-selected material, partially separating parts from crushed material, and creating raw materials. The waste collection processes in this scenario are identical to Scenario 1, i.e., collecting construction debris and waste from smaller reconstructions in designated bags, distributing 5 m^3 containers for construction waste from medium reconstructions, and obliging construction firms to bring construction waste directly to the Drisla landfill for larger construction projects. In the waste treatment part, this scenario involves setting up equipment for crushing construction waste on-site at the Drisla landfill. The capacity of the equipment meets the projected annual quotas of generated construction waste for the Skopje Region, amounting to 150,000 tons annually. The value of the equipment is 450,000 euros, and the required procedure for setting up and commissioning the equipment is estimated at 2 years (urban and technical-technological projects, execution, supervision, and commissioning of the system).

C) **Scenario** 3: STM – *Selected Treatment on Mobile Equipment*

This scenario involves preparation for crushing similar to Scenario 2, but with the use of mobile equipment for crushing and final selection (including dust control equipment with sprayers) [9]. This implies that the equipment from the project is used at the Drisla landfill and, if necessary, at other locations designated for processing construction waste (large sites where waste is generated, other regional waste processing centres, construction sites, etc.). This scenario is a combination of the previous scenarios. Methods for collecting construction waste from Scenario 1 are used, indicating complete waste collection. In terms of the final product obtained during waste treatment, products are obtained from Scenario 2, such as cushioning materials and crushed asphalt. Regarding the equipment, this scenario involves the acquisition of mobile construction equipment for crushing construction waste. The capacity of the crusher will be dimensioned to meet at least 50% more than the quantities of generated construction waste in the Skopje Region. This allows the mobile equipment to move at short intervals (transport by truck with a platform) to construction sites or other locations where construction waste is generated. Along with the crusher, elements for preventing dust formation, such as water sprayers, need to be taken. The investment for the equipment in this scenario is 380,000 euros, and the duration for putting the equipment into operation is estimated at 2–3 months from the moment of procurement.

D) **Scenario 0:** *DN – Do Nothing*

A scenario in which the state of handling and managing construction waste remains unchanged. The description of the current situation is given in the Aims and Background section.

1) *Economic analysis of the projected scenarios*

The economic analysis of implementing each scenario is conducted to compare the developed scenarios in this study. The economic analysis is done for a six-year period and is based on several elements:

- The amount of investment required for each proposed technology in the scenarios.
- Funds obtained from the charged subsidized fee for depositing selected construction waste.
- Costs for processing the applied construction waste.
- The value of the material obtained from recycling and processing (as an amount not spent on acquiring new material).

The quantities of waste used for analysis are taken from the quantities of landfilled construction waste in Drisla in 2023 and projections for generated construction waste and debris in the Regional Waste Plans of the Ministry of Environment and Physical Planning. These quantities are given in Figure 2. The prediction parameters of the amount of generated waste are identical for all scenarios.

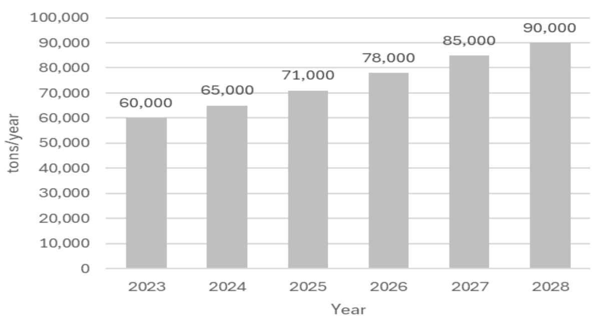

Fig. 2. Estimated CDW quantity delivered to Drisla from 2023 to 2028

In the analysis of investments, constant prices for waste disposal from the price list of the Public Enterprise Landfill Drisla in Skopje were used, with the possibility of correction in the next 6 years [10]. The prices for delivered CDW for landfilling are given in Figure 3. These prices are identical for all scenarios.

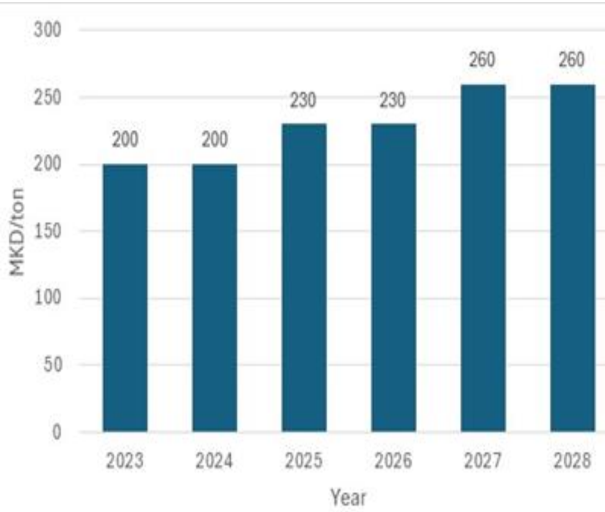

Fig. 3. Prices for undertaking CDW in Drisla from 2023 to 2028

Keeping this in mind, economy models are developed for all the scenarios: FT, ST and STM. To make the calculation easily comparable, few factors are taken into account:

Inflation is not calculated.

- All investment is calculated as delivered to the place of operation, commissioned, including training of personnel.
- All expenses (customs and other) are calculated in the price of investment.
- All profit/loss is calculated pre-taxed.

The total investments in equipment purchase and infrastructure preparation necessary for each scenario are given in Table 2.

T a b l e 2

Total investment for each scenario

	FT	ST	STM
Total investment in equipment and infrastructure (in euros)	154,365,000	67,035,000	56,580,000

3. RESULTS AND DISCUSSION

Selection of most feasible scenario is determined by the following criteria:

- Simplified ROI – return of investment,
- Execution time of the scenarios.

Calculations suggest that the FT scenario has a 12.2 year of ROI, which is logical having in mind the large investments for this scenario. ST scenario has a favourable ROI compared to FT, but the time of execution of this scenario is more than 2 years. This is due to the need for new urban and plan documentation, construction and mechanical projects and legal permits from the city and the municipalities. On the other hand, STM scenario has the best ROI, and the execution time is estimated at 6 months from the point of decision to implement the scenario. The operation of the equipment can be put in place after 6 months from the start of the purchasing from the city of Skopje, and in the same 6 months, a public campaign can be developed and executed so that the processes go simultaneously. The abovementioned data are summarized in Table 3.

T a b l e 3

ROI and execution time of each scenario

Assessment criteria	**FT**	**ST**	**STM**
ROI (years)	12.2	5.0	4.0
Execution time (years)	2.1	2.1	0.6

Measurable benefits from each of the proposed scenarios are reducing GHG emissions, lowering the landfilled CDW amount and increasing the recycled CDW amount. Using the emission factor for CDW recycling the CO_2 equivalent emission reduction due to execution of any scenario in the six-year calculation period is 18,031,840 kg CO_2-e [11]. The CDW left unproperly outside regulated landfill will be reduced by 449,000 tons. This amount of CDW would have been left in dumpsites in the DN Scenario. And the amount of CDW that will be recycled as secondary raw material and further used amounts to 179,000 tons. This contributes to lower emission of CO_2 due to lower mining processes, lower transport needed and lower natural resources consumption. The measurable environmental impacts are presented in Table 4.

Table 4

Environmental impact from implementation of any scenario

Additional parameters	All scenarios
GHG emission reduction (CO_2kg-e)	18,031,840
Reduction of CDW outside of landfill (t)	449,000
Amount of CDW recycled (t)	179,600

The immeasurable positive impacts are reflected through human health, soil, water, air quality, and socio-economic impact.

a) *Impact on human health*

In the long term, any of the proposed scenarios that would be implemented will positively influence the health of the citizens of the Skopje Region. It will contribute to establishing processes for the rational management of construction waste. The previous practice of leaving construction waste and debris in unregulated dumps and undefined locations is expected to significantly decrease. With a robust awareness campaign and enhanced efforts by inspection services, it is expected that a large portion of construction waste dumped in inappropriate locations will be affected by implementation of the activities. This will subject the waste to sorting, reuse of useful fractions, and recycling of fractions that can be used as buffer materials. This will directly reduce environmental pollution by around 50,000 tons of construction waste, decrease soil pollution, and subsequently reduce contamination of groundwater. Additionally, this will reduce the need for buffer materials from quarries, thereby decreasing air pollution from mining activities. Implementing the activities of these scenarios will lead to a reduction in the quantities of construction debris disposed of, elimination of small and micro-dumps everywhere, and an increase in public awareness regarding the quality of life and improvement of waste management practices.

b) *Socio-economic impact*

The implementation of the proposed scenarios will positively impact the socio-economic condition. It will introduce economic activity that contributes to better financing of public enterprises in the City of Skopje, especially the Drisla landfill. This enables the funds saved from the purchase of buffer materials to be invested in the development of the landfill, towards multiple systems to prevent waste creation, pollution prevention, and high-quality waste treatment for the waste from the Skopje planning region. The interest in establishing new processes in the circular economy in the Skopje planning region will increase and the economic conditions for employment will improve. Furthermore, establishment of improved waste management processes will be enabled, contributing to higher qualifications and better-paid job opportunities for those involved. The waste processing will reduce the amount of material being landfilled, extending the life of the Drisla landfill and reducing the need for new landfills.

c) *Impact on soil*

The implementation of these scenarios, designed for the treatment and management of construction debris and waste, will result in the rational use of land. Significant positive and long-term impacts on the soil are expected. Over 70 locations where construction waste was previously dumped will remain uncontaminated. Additionally, by establishing a waste flow for construction debris, the life of the Drisla landfill will be extended, reducing the need for new landfills. These solutions provide an opportunity for municipal authorities, through consistent compliance with legal obligations, to prevent any soil pollution from the disposal of construction debris and waste.

d) *Impact on air quality*

With the implementation of the proposed scenarios, long-term positive effects on air quality are expected. In areas where construction debris and waste are generated, practices for the selection, separation, and handling of construction waste are expected to improve. Furthermore, a reduction in open waste dumping and a decrease in dust content from waste are anticipated. At the location where the waste is processed, there is an expected generation of dust, which will be partially treated with water sprays. Emissions of harmful components from fuel combustion in the exhaust emissions are expected from the operation of machinery.

e) *Impact on the quality of surface and groundwater*

Since the construction activities planned for each scenario are not dependent on large quantities of water, environmental pollution due to emissions of waste waters is expected to be insignificant. Near the project site, where activities will be implemented, sprinklers are planned to be used to reduce dust from the crushing process of construction material, which could lead to emissions into groundwater through the soil and via the sewage system.

4. CONCLUSIONS

In this paper, four distinct scenarios have been outlined for the improved management and treatment of waste stemming from construction activities and construction debris within the Skopje Region. Each scenario presents a unique approach towards addressing the challenges associated with construction waste, spanning technical and organizational enhancements, economic viability, and environmental impact considerations. The scenarios delineated include Full Treatment, Selected Treatment, Selected Treatment on Mobile Equipment, and a baseline scenario of Do Nothing. Through a detailed description of each scenario's operational framework, including waste collection methods, treatment processes, and associated investments, this paper offers a comprehensive assessment of potential pathways for managing construction waste within the region. From a technical standpoint, the scenarios encompass a spectrum of waste treatment methodologies, ranging from comprehensive automated processes to more streamlined approaches. Economic analyses conducted for each scenario shed light on the financial implications of implementation, considering factors such as ROI and execution timelines of scenarios. Notably, the economic analysis reveals varying degrees of feasibility among the scenarios, with ST Mobile emerging as the most economically viable option, boasting a favorable ROI and relatively swift implementation timeframe. This scenario leverages mobile equipment for waste treatment, offering flexibility in deployment and minimizing operational delays.

Furthermore, the paper underscores the significant environmental benefits associated with the proposed scenarios, including decreased quantities of construction debris disposed of outside regulated landfills. This will result in reduced environmental damage and saved funds that were previously spent on clearing unregulated construction waste landfills. The recycling rates will increase, leading to reduced damage caused by mining activities for excavating landfill material. By adopting these measures, the region stands to mitigate environmental pollution, enhance soil and water quality, and improve overall air quality through more sustainable waste management practices. Other benefits include increased gains from the introduction of advanced technology and an improved level of qualifications for personnel in enterprises.

In addition to tangible environmental benefits, the implementation of these scenarios holds promising socio-economic implications for the Skopje Region. Beyond fostering economic activity and resource utilization efficiency, the proposed initiatives are poised to stimulate job creation, enhance public awareness, and bolster the region's transition towards a circular economy model.

In conclusion, the findings presented in this paper underscore the critical importance of proactive waste management strategies in mitigating the environmental impact of construction activities. By embracing innovative approaches and collaborative efforts, stakeholders in the Skopje Region can pave the way for sustainable development and pave a path towards a cleaner, more resilient future.

REFERENCES

[1] *Census of the Population, Households and Apartments in the Republic of North Macedonia, 2021*, Republic of North Macedonia, State Statistical Office, 2022. https://www.stat.gov.mk/publikacii/2022/POPIS_DZS_web_MK.pdf

[2] *News Release Municipal Waste, year 2022*, Republic of North Macedonia, State Statistical Office, 2023. https://www.stat.gov.mk/pdf/2023/9.1.23.01_mk.pdf.

[3] *Table Municipal Waste, year 2023*, Republic of North Macedonia, State Statistical Office, 2024. https://www.stat.gov.mk/PrikaziSoopstenie.aspx?rbrtxt=80

[4] Dodd, N., Donatello, S. & Cordella, M.: *Level(s) indicator 2.2: Construction and Demolition waste and materials,* European Commission, Publication version 1.0 (2020), https://susproc.jrc.ec.europa.eu/product-bureau/sites/default/files/2020, 10/20201013%20New%20Level(s)%20documentation_2.2%20C&d%20waste_Publication%20v1.0.pdf

[5] Tokpah, P.: *Hazardous Construction and Demolition Waste Management and Control,* 2023, https://www.researchgate.net/publication/366976842_Hazardous_Construction_and_Demolition_Waste_Management_and_control.

[6] Bianchini, G., Ristovski, I., Milcov, I., Zupac, A., Natali, C., Salani, G. M., Marchina, C., Brombin, V., & Ferraboschi, A.: Chemical Characterisation of Construction and Demolition Waste in Skopje City and Its Surroundings (Republic of Macedonia), *Sustainability*, vol. **12**, No. 5, 2020. https://doi.org/10.3390/su12052055

[7] European Environmental Agency: *Municipal waste management in Western Balkan countries — Country profile*

(North Macedonia), European Topic Centre on Waste and Materials in a Green Economy, 2021. https://www.eea.europa.eu/themes/waste/waste-management/municipal-waste-management-country/north-macedonia-municipal-waste-factsheet-2021

[8] *Waste Management Plan of the Republic of North Macedonia for 2021–2031*, Republic of North Macedonia, Ministry of Environment and Physical Planning, 2021. https://shorturl.at/UXHMJ

[9] European Commission: *Service Contract on Management of Construction and Demolition Waste – SR1 – Final Report Task 2*, Bio Intelligence Service, 2011. https://environment.ec.europa.eu/system/files/2020-12/2011_CDW_Report_0.pdf

[10] Bilsen, V., Kretz, D., Padilla, P., Van Acoleyen, M., Van Ostaeyen, J., Izdebska, O., Hansen, E., Bergmans, J., & Szuppinger, P.: *Development and Implementation of Initiatives Fostering Investment and Innovation in Construction and Demolition Waste Recycling Infrastructure*, European Comission, 2018. https://environment.ec.europa.eu/system/files/2020-12/CDW%20infrastructure%20study_0.pdf

[11] Public Enterprise Landfill Drisla Skopje: *Pricelist*. 2020. https://drisla.mk/czenovnik/

[12] Wang, T., Kaiyi, L., Liu, D., Yang, Y. & Wu: Estimating the carbon emission of construction waste recycling using grey model and life cycle assessment: A case study of Shanghai, *International Journal of Environmental Research and Public Health*, Vol. **19**, No.14, 2022. https://doi.org/10.3390/ijerph19148507

Mechanical Engineering – Scientific Journal, Vol. **43,** No. 1, pp. 31–38 (2025)
Number of article: 691
Received: April 17, 2025
Accepted: May 12, 2025
In print: ISSN 1857–5293
On line: ISSN 1857–9191
UDC: 553.551.4:622.73.05]:621.926.3(497.7)
https://doi.org/10.55302/MESJ2543131a

Original scientific paper

MINERAL PROCESSING OF THE DOLOMITES FROM DEPOSITS IN THE REPUBLIC OF NORTH MACEDONIA

Elena Arsoska[1], Andrijana Čankulovska Tenovska[1], Tajana Kostadinova[1], Arianit Reka[2], Slobodan Bogoevski[1], Boško Boškovski[1]

[1]*Faculty of Technology and Metallurgy, "Ss. Cyril and Methodius" University in Skopje, Ruǵer Bošković 16, Skopje, Republic of North Macedonia*
[2]*Faculty of Natural Sciences and Mathematics, University of Tetovo, 1200 Tetovo, Republic of North Macedonia*
earsoska@yahoo.com

A b s t r a c t: Dolomites are used as a raw material in various industries such as construction, inorganic chemical technology, metallurgy, agriculture, etc. In the Northwestern Region of the Republic of North Macedonia, there are several deposits of dolomite that are exploited. In this research, the dolomites from the localities of Čajle, Ogledalec and Suvodol were examined. The aim of the research is to define the mineral processing of the dolomite raw materials. The basic parameters of the grain size reduction were optimized, with a comparison between the deposits. Therefore, the dolomite raw materials were processed on a jaw crusher, a roller crusher and in a porcelain mill with balls. A wet sieve analysis was conducted to define the efficiency of size reduction. Various size fractions of grains were observed on a binocular microscope. The discussion of the obtained results defines the relation between material pressure strength and the efficiency of the grain size reduction process, as well as the electricity consumption.

Key words: dolomite; mineral processing; Čajle; Ogledalec; Suvodol

ТЕХНОЛОШКА ПОДГОТОВКА НА ДОЛОМИТИ ОД ЛЕЖИШТА ВО РЕПУБЛИКА СЕВЕРНА МАКЕДОНИЈА

А п с т р а к т: Доломитот се користи како суровина во различни индустрии – градежништво, неорганска хемиска технологија, металургија, земјоделио, итн. Во Северозападниот Регион на Република Северна Македонија постојат повеќе лежишта на доломит од коишто се врши експлоатација. Во ова истражување се испитувани доломитите од локалитетите Чајле, Огледалец и Суводол. Основната цел на истражувањето е да се дефинира процесот на технолошката подготовка на суров материјал. Оптимизирани се основните параметри на обработката на суровиот материјал, со соодветна компарација на лежиштата. Притоа е применето дробење во челусна дробилка и дробилка со валјаци, како и мелење во порцеланска мелница со топки. Направена е и ситова анализа за да се согледа ефикасноста од процесот на уситнување. Фракците со различни димензии на зрната се набљудувани под бинокулар. Добиените резултати ја дефинираат релацијата помеѓу цврстината на материјалот и ефикасноста на процесот на уситнување, а со тоа и потрошувачката на електрична енергија.

Клучни зборови: доломит; технолошка подготовка; Чајле; Огледалец; Суводол

1. INTRODUCTION

Limestones are widespread in the Republic of North Macedonia [1–4]. There are several dolomite deposits in the Northwestern Region. Previous explorations suggest that there are significant reserves of dolomite deposits in the localities of Čajle, Ogledalec and Suvodol [5–8]. As a raw material, dolomite has potential applications in various industries. Dolomite is mainly used as a raw material for refractory bricks production. Dolomite rock sand is used as fine aggregate replacement in construction activities. In inorganic chemical technologies, dolomite is used as a raw material for production of liquid fertilizer, as an alternative to limestone in cement manufacturing, etc. Dolomite is also used as an additive in animal feed

[9–14]. For efficient productivity, the mineral processing of dolomite is crucial. Therefore, the basic parameters of the size reduction process were defined [15–21] with a comparison between the deposits.

2. MATERIALS AND METHODS

In this research the dolomite raw materials from the localities of Čajle, Ogledalec, and Suvodol were examined. Within the mines there are processing plants where the raw material is crushed and separated by size into various dimensional fractions. The dolomite samples of 20 – 60 mm were collected for analysis (Figure 1).

In the mineral processing, the materials were primarily crushed. At first on a jaw crusher Blake (Figure 2). Then the materials were treated three times (at different distances between the rollers of 8.3 and 1 mm) on a roller crusher Denver B7141A (Figure 3). As the last stage of grain size reduction, the raw materials were processed into a porcelain ball mill (Figure 4). The material : ball ratio is 1 : 2,5 and the velocity of rotation is ω = 65°/min. The duration time of milling was 10, 20, 30, 60, and 120 min. In order to define the grain size reduction a wet sieve analysis was conducted. Set of standard sieves with a perforation size of 0.032 mm to 0.1 mm were used. Also, the various dimensional fractions of grain were observed on a binocular Carl Zeiss Jena [22–25].

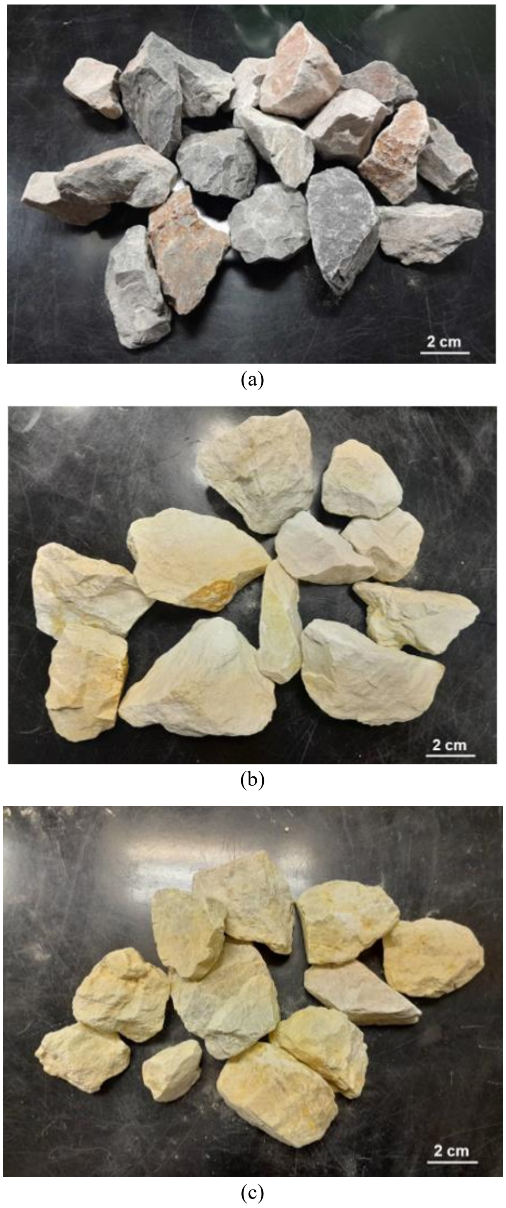

(c)

Fig. 1. Dolomite samples of 20–60 mm: (a) Čajle, (b) Ogledalec, (c) Suvodol

Fig. 2. Jaw crusher Blake

Fig. 3. Roller crusher Denver B7141A

Fig. 4. Porcelain mill with balls

The pressure strength is a significant characteristic for the mechanicaly preparation. Therefore, the pressure strength was determined on a compression testing machine (Figure 5).

Fig. 5. Pressure strength testing

3. RESULTS AND DISCUSSION

The pressure strength of the dolomite raw materials is presented in Table 1. The highest value of 174.2 MPa has dolomite from Čajle, and the lowest value of 131.5 MPa has dolomite from Suvodol. Dolomite from Ogledalec has a pressure strength of 167.4 MPa.

T a b l e 1

Pressure strength of the dolomite

Čajle	174.2 MPa
Ogledalec	167.4 MPa
Suvodol	131.5 MPa

The jaw crusher uses compressive force to crush the material pieces. The compressive force is applied by two jaws, one of the jaws is fixed while the other is movable. The material is fed into the top feed opening (gape) and gradually moves downwards towards the lower discharge outlet. As the material passes towards the outlet, it is crushed between the fixed and movable jaws. Because the distance between the two jaws decreases towards the discharge outlet, the size of the pieces is progressively reduced (Figure 6).

During the mechanical destruction process, fractures are formed in the direction of the cleavage plane. Consequently, the dolomite aggregates have a flat and sharp shape (Figure 7). This phenomenon is also present to the finest fraction of grains.

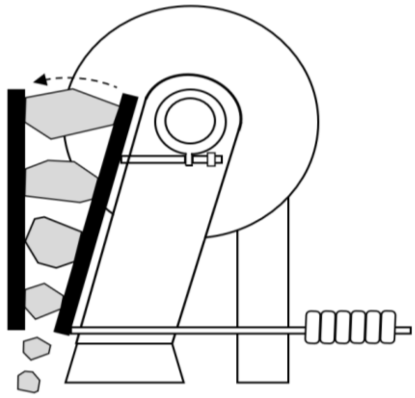

Fig. 6. Jaw crusher

Čajle

Ogledalec

Suvodol

Fig. 7. The raw materials after treating on a jaw crusher

The roller crusher consists of two heavy rollers placed in parallel, which are rotating in opposite directions (toward each other) and crush the material pieces (Figure 8). The size of crushed pieces is determined by the gap (the distance) between the rollers, which can be adjusted to suit the specific application requirements of the material.

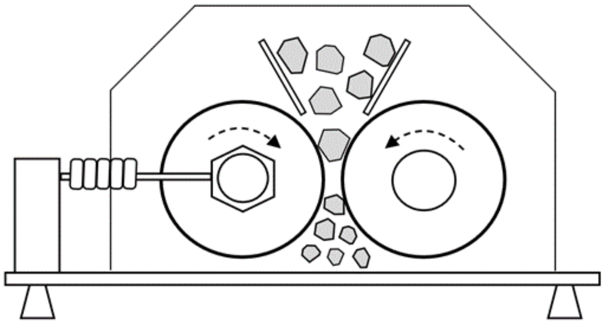

Fig. 7. Roller crusher

The granulometric composition of the dolomite raw materials after processing on the roller crusher is presented in Table 2.

T a b l e 2

Granulometric composition of the materials after processing on the roller crusher (mass %)

Dimensional fraction	Čajle	Ogledalec	Suvodol
+1 mm	47.62	37.46	27.76
–1 +0.5 mm	21.16	20.16	19.66
–0.5 +0.25 mm	10.10	12.46	14.60
–0.25+0.1 mm	6.22	6.40	7.48
–0.1 mm	14.90	23.52	30.50
Σ	100.00	100.00	100.00

The results correlate with the pressure strength. Accordingly, the dominant mass content of the coarse fraction (+1 mm) of 47.62 % has the dolomite from Čajle, while the dolomite from Suvodol has the highest mass content of the smaller fraction (–0.1 mm) of 30.52 %. This effect is explicitly observed on Figure 8.

In the final stage of the size reduction process, dry milling was applied into a ball mill. The ball mill consists of a drum that rotates around its axis. The drum is filled in the range of 30 – 50% with balls that grind the materials. As the drum rotates, the balls are held on the inner surface of the drum by centrifugal force. At a certain angle (depending on the velocity of rotation), the weight of the balls overcomes the centrifugal force and then they cascade down or drop from top of the drum (Figure 9). Analogically, the material pieces are ground by impact and attrition.

Čajle

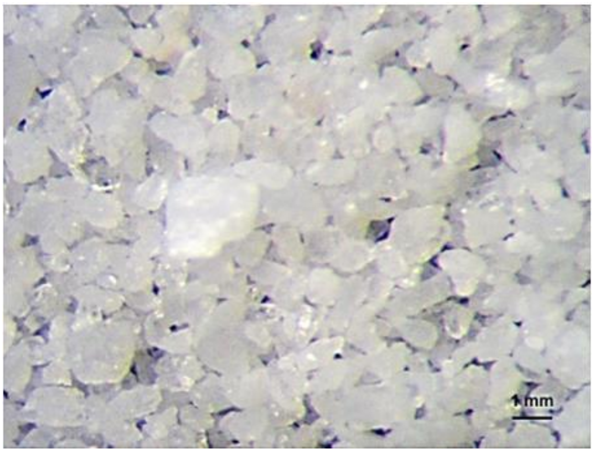

Ogledalec

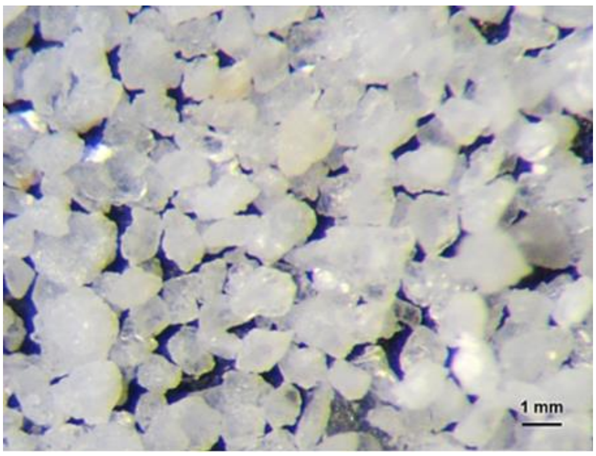

Suvodol

Fig. 8. The raw materials after treating on a roller crusher

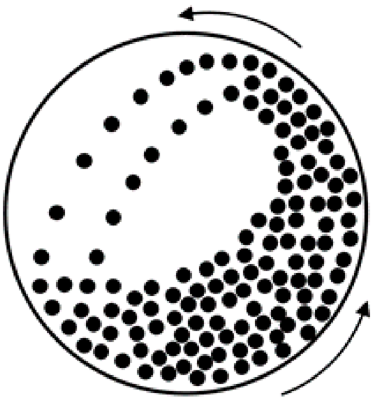

Fig. 9. Ball mill

The histograms of the mass content of various dimensional grain fractions at different milling phases are presented on Figure 10.

Simply, as the duration of milling time increases, the content of the finest fraction (–0.032 mm) continuously increases. Inversely, the content of the coarsest fraction (+0.1 mm) continuously decreases. The other size fractions have a minimum content. According to the granoblastic texture of raw materials, which are dominantly composed of fine grains, the size reduction is not affected by grinding, but is a consequence of the release of bounded fine grains in the aggregates.

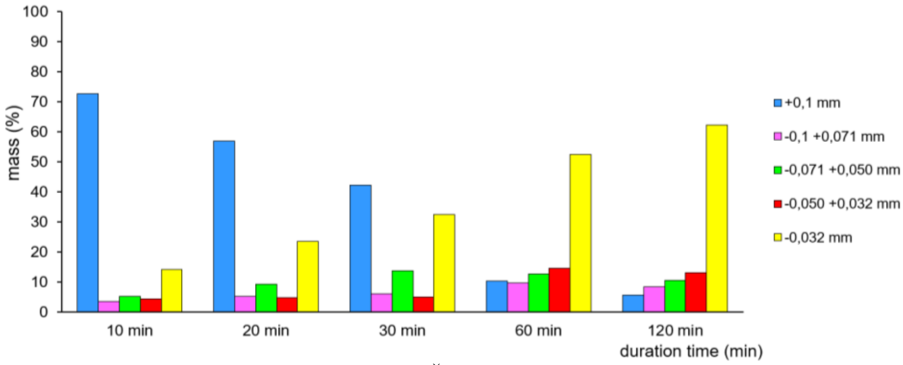

Čajle

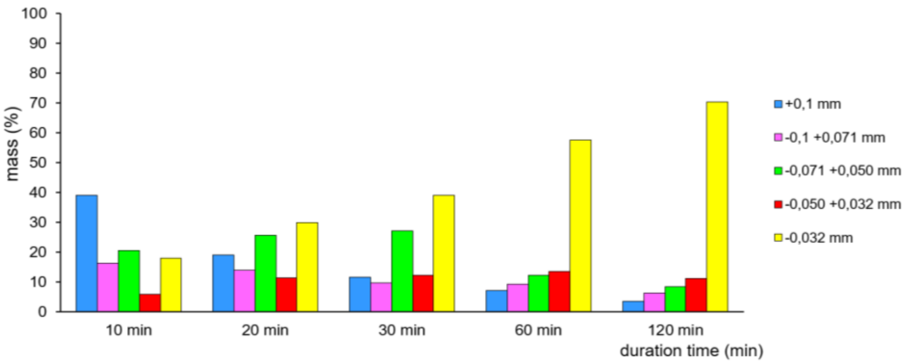

Ogledalec

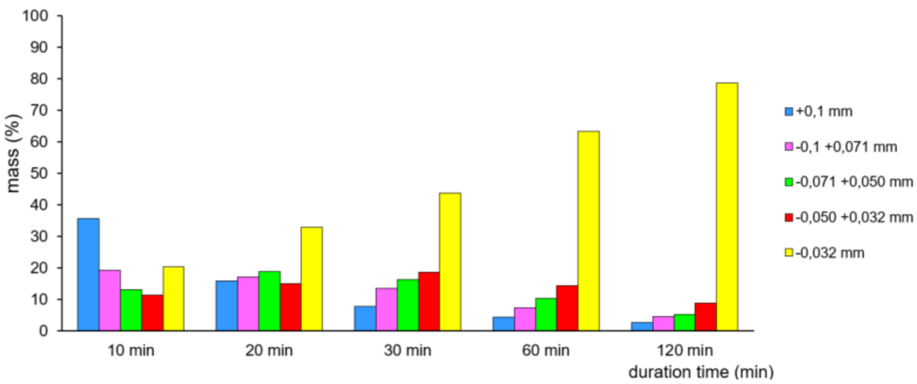

Suvodol

Fig. 10. Histograms of the mass content of various dimensional grain fractions at different milling phases

On Figure 11 are presented the curves of cumulative mass content of the finest fraction (–0.032 mm) at different milling phases. The asymptotic direction of curves indicates that the size reduction is insignificant after 60 minutes of milling time. Therefore, the optimal duration of milling time is in range of 50 – 60 minutes, where there is an optimal ratio of the duration time (electricity consumption) and size reduction.

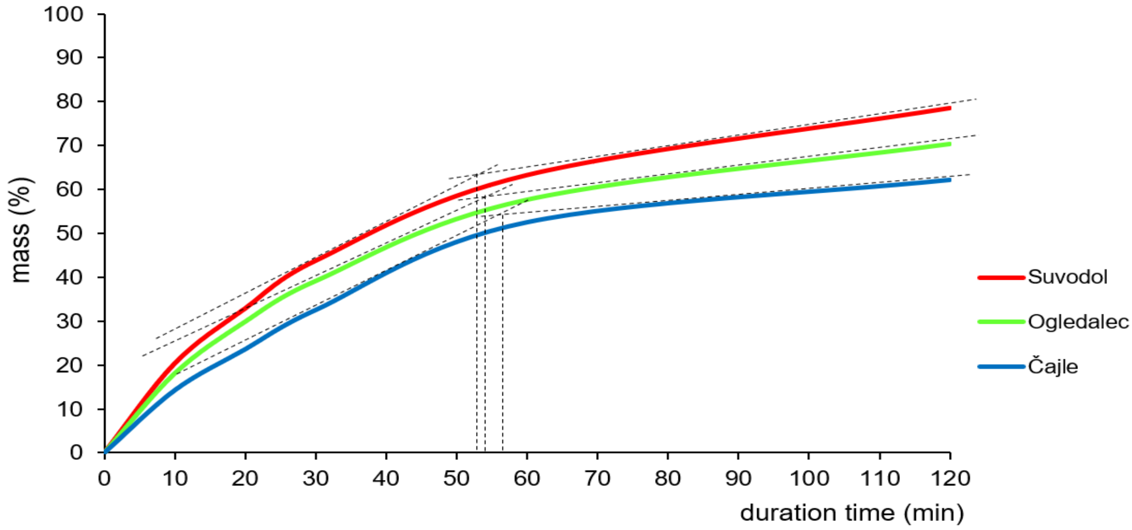

Fig. 11. Curves of cumulative mass content of the finest fraction (–0.032 mm) at different milling phases

Therefore, in Table 3 is presented the granulometric composition of the materials after 60 minutes of milling time. In addition to the previous results, the dominant mass content of the bigger fraction (+1 mm) of 10.33 % has the dolomite from Čajle, while the dolomite from Suvodol has the highest mass content of the finest fraction (–0.032 mm) of 63.24 %.

After 60 minutes of milling time, the size reduction of the dolomite raw materials is evident (Figure 12). In the finest dimensional grain fraction (–0.032 mm), as a consequence of increased surface activity, an intense aggregation was observed.

T a b l e 3

Granulometric composition of the materials after 60 minutes of milling time, (mass %)

Dimensional fraction	Čajle	Ogledalec	Suvodol
+0.1 mm	10.33	7.21	4.35
–0.1 +0.071 mm	9.76	9.33	7.47
–0.071 +0.050 mm	12.76	12.31	10.48
–0.050 +0.032 mm	14.68	13.52	14.46
–0.032 mm	52.47	57.63	63.24
Σ	100.00	100.00	100.00

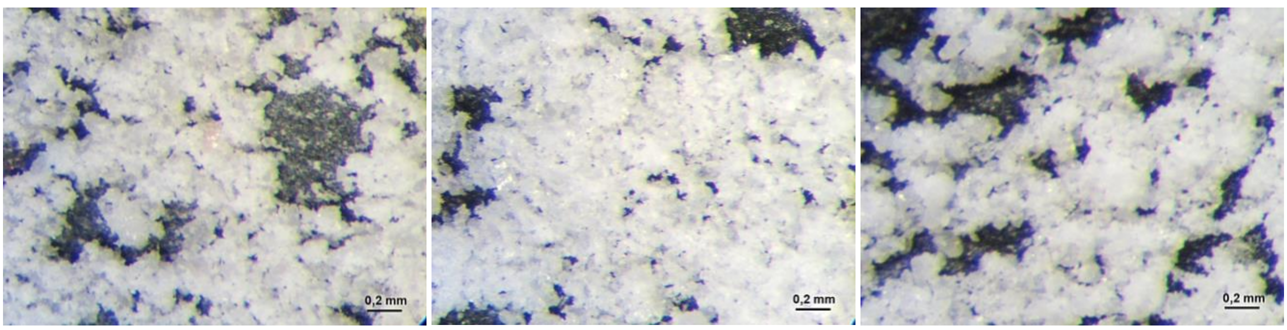

Čajle Ogledalec Suvodol

Fig. 12. The finest dimensional fraction (–0.032 mm) after 60 minutes of milling time

4. CONCLUSION

Dolomite has potential applications in various industries. As a raw material, dolomite is mainly used in construction, inorganic chemical technology, agriculture, etc. Therefore, in this research, the dolomites from the localities of Čajle, Ogledalec, and Suvodol were examined. The research defined the mineral processing of the raw materials. The samples with dimensions of 20 – 60 mm were primarily crushed, on jaw crusher and then on a roller crusher. Additionally, the samples were processed into a porcelain ball mill. In order to define the size reduction, a wet sieve analysis was conducted. Also, the various dimensional fractions were observed on a binocular. As a consequence of mechanical destruction, the dolomite grains have a flat and sharp shape.

The pressure strength of the materials was determined, as a significant property of mechanical destruction. The dolomite from Čaile has the highest value of compressive strength, while the dolomite from Suvodol has the lowest value. Therefore, the dolomite from Čaile has the highest mass content of the coarse grain fraction (+1 mm) after processing on a roller crusher. Consequently, the dolomite from Suvodol has the highest mass content of the finest grain fraction (–0.032 mm) after 60 minutes of milling. According to previously obtained results, the milling process can be implemented at specific regime in order to accomplish the previously set requirements for specific size fractions. The optimal duration of milling time is in range of 50 – 60 minutes.

Dolomites are mainly used as a raw material in construction, inorganic chemical technology, in agriculture, as an additive in animal feed, in metallurgy etc. Therefore, the basic parameters of the size reduction process were defined, with a comparison between the deposits.

REFERENCES

[1] Jovanovski, G., Boev, B., Makreski, P. (2012): *Minerals from the Republic of Macedonia with an Introduction to Mineralogy*, Macedonian Academy of Sciences and Arts, Skopje.

[2] Стојановиќ, М. (2005): *Наоѓалишта на неметални суровини во Македонија,* Скопје.

[3] Arabadžiev, D., Stefov, V., Stafilov, T., Boev, B. (2001–2002): Physico-chemical investigations of limestones in the Republic of Macedonia, *Geologica Macedonica*, 15–16, 35–41.

[4] Hristova, E., Jančev, S. (2003): Characteristics of a calcite "limestone"–marble from Macedonia, used as flux material, *Journal of Mining and Metaleurgy*, *Section B Metallurgy*, **39**, 3–4.

[5] Ри Рудинг ДОО – Скопје (2008): Главен рударски проект за експлоатација на доломит од површинскиот коп "Чајле" – Гостивар.

[6] Геолошки завод, ООЗТ Институт за истражување на минерални суровини (1988): Елаборат за класификација, категоризација, прекатегоризација на резервите на доломитското лежиште "БРЕСТ" (Силика минерал).

[7] Рудпроект ДОО – Скопје (2015): Елаборат за класификација, категоризација, прекатегоризација, на резервите на доломитското лежиште "Огледалец" – Македонски Брод.

[8] Геохидроинженеринг – Скопје (2014): Елаборат за класификација, категоризација, прекатегоризација, на резервите на доломитското лежиште "Пеклиште" с. Трново – Гостивар.

[9] Tsirambides, A. (2001): Industrial applications of the dolomite from Potamia, Thassos Island, N. Aegean Sea, Greece, *Materials and Structures*, **34** (2), 110–113. DOI: 10.1007/BF02481559

[10] Gruszecka-Kosowska, A., Wdowin, M., Kosowski, T., Klimek, A. (2015): An analysis of the chemistry, mineralogy and texture of waste dolomite powder used to identify its potential application in industry, *Geology, Geophysics & Environment*, **41** (4), 343–352. DOI:10.7494/geol.2015.41.4.343

[11] Tejashwi, L., Ananthkumar, M., Chinnaiyan, P., Bharath Krishnaa, A.C., Sasi, M. (2021): Dolomite rock sand as fine aggregate replacement in construction activities: A comparative study, *Materials Today Proceedings*, **46** (10), 5148–5152. DOI: 10.1016/j.matpr.2020.10.678

[12] Divekar, S., Sawant, R.M. (2023): Dolomite powder in concrete: a review of mechanical properties and microstructural characterization, *Civil Engineering and Architecture*, **11** (6), 3314–3321. DOI: 10.13189/cea.2023.110607

[13] Adeniyi, A.G., Ighalo, J.O. (2020): Synthesis of liquid fertilizer from rock phosphate and dolomite: An adjusted technique, *Iranian Journal of Energy & Environment*, **11** (3), 221–224. DOI: 10.5829/ijee.2020.11.03.07

[14] Filev, K., Gjorgovska, N., Arsov, N., Bogoevski, S. (2004): Dolomit as a source of magnesium for nutrition, *Krmiva,* **46** (4), 211–216.

[15] Tripathy, S. H., Murthy, Y. R., Panda, L., Singh, V., Banerjee, P. K., Bhatnagar, A. (2013): A review on dolomite: genesis, application and processing, *Journal of Mines, Metals and Fuels*, **62** (4), 93–102.

[16] Matijašić, G., Žižek, K., Hraste, M. (2007): Dolomite grinding behavior in laboratory planetary ball mill, *Industrial Ceramics*, **27** (2), 95–100.

[17] More, R., Parkhi, R., Nevase, S., Narayane, S., Lokhande, P.H. (2019): Design of dolomite crushing and grinding plant, *Journal of Emerging Technologies and Innovative Research*, **6** (4), 864–867. ISSN: 2349–5162.

[18] Osman, A. F, Fauzi, A. A. A., Amin, M. B., Halim, K. A. A., Ul-Hamid, A. (2022): Size reduction of dolomite into nano-size range through milling and tip-sonication processes, *Materials Science Forum*, **1075**, 3–8. DOI: 10.4028/p-3zkle9

[19] Nad, A., Brożek, M. (2018): Analysis of the particle size distribution of products crushing shale and dolomite crushing by compression of single irregular particles, *Journal of the Polish Mineral Engineering Society*, **20** (2), 241–245. DOI: 10.29227/IM-2018-02-30

[20] Menéndez, M., Gent, M., Torno, S., Crespo, N. (2017): A bond work index mill ball charge and closing screen product size distributions for grinding crystalline grains, *International Journal of Mineral Processing*, **165**, 8–14. DOI: 10.1016/j.minpro.2017.05.011

[21] Nikolić, V., Ferradal, P. S., Pierres, J. M., Menéndez-Aguado, J. M., Trumić, M. (2024): Methods for estimating the bond work index for ball mills, *Minerals*, **14**, 1264, DOI:10.3390/min14121264

[22] Wills, A. B., Napier-Munn, T. (2006): *Mineral Processing Technology*, 7th Edition, Elsevier Science & Technology Books.

[23] Кнежевић, Д. (2001): *Припрема минералних сировина*, Рударско-геолошки факултет, Београд.

[24] Бошковски, Б., Богоевски, С. (2023): *Подготовка на минерални суровини. Практикум за лабораториски вежби,* Технолошко-металуршки факултет, Универзитет Св. „Кирил и Методиј“ во Скопје.

[25] Boškovski, B., Jančev, S., Pavlovski, B., Reka, A., Čanklovska, A., Bogoevski, S. (2021): Characterization of the calcite raw material from the microlocalities of Šušički Most and Gorna Banjica near Gostivar, Republic of North Macedonia, *Geologica Macedonica*, **35** (2), 85–94. DOI: 10.46763/GEOL21352085b

Mechanical Engineering – Scientific Journal, Vol. **43,** No. 1, pp. 39–47 (2025)
Number of article: 692
In print: ISSN 1857–5293
Received: April 17, 2025
On line: ISSN 1857–9191
Accepted: May 12, 2025
UDC: 552.581.08-049.8:62/63(497.722)
https://doi.org/10.55302/MESJ2543139k

Original scientific paper

SPECIFIC APPLICATIONS OF DIATOMACEOUS EARTH FROM SLAVIŠKO POLE, REPUBLIC OF NORTH MACEDONIA

Tajana Kostadinova, Andrijana Čankulovska Tenovska, Katerina Atkovska, Gordana Ruseska, Boško Boškovski, Slobodan Bogoevski

Faculty of Technology and Metallurgy, University "Ss Cyril and Methodius" in Skopje, Rugjer Bošković 16, 1000 Skopje, Republic of North Macedonia
tajana@tmf.ukim.edu.mk

A b s t r a c t: Diatomaceous earth from Slaviško Pole, based on the results of mineralogical-petrographic and physico-chemical analyses, exhibits specific characteristics that could be utilized to meet particular industrial, construction, and agricultural requirements. As a raw material predominantly composed of feldspars, K-feldspar of the microcline type, as well as Na-Ca plagioclases of albite-oligoclase type, several species of diatoms, and minor quantities of quartz, iron-bearing minerals, and other trace elements embedded within sedimentary layers, it demonstrates properties that align well with certain application demands. The material has been found to possess exceptionally favorable thermal insulation characteristics in compact segments, making it highly suitable for the construction industry, along with the potential for straightforward mechanical processing. Further investigations into its chemical and mineralogical composition, primary particle size distribution, and mechanical transformation potential have revealed parameters that strongly indicate possible applications in agriculture, including ecological pest control against insects and nematodes, soil conditioning and pH regulation, and passive soil decontamination. Additionally, its applicability in filtration processes for potable and waste water, as well as other fluids, has been identified.

Key words: diatomaceous earth; Slaviško Pole; thermal insulation properties; ecological pest control

МОЖНОСТИ ЗА СПЕЦИФИЧНА ПРИМЕНА НА ДИЈАТОМЕЈСКАТА ЗЕМЈА ОД СЛАВИШКО ПОЛЕ, РЕПУБЛИКА СЕВЕРНА МАКЕДОНИЈА

А п с т р а к т: Дијатомејската земја од Славишко Поле, според резултатите од минералошко-петрографските и физичко-хемиските испитувања, покажува некои специфични карактеристики кои би можеле да се искористат за исполнување конкретни специфични барања во индустријата, градежништвото и земјоделието. Како суровина која доминантно содржи фелдспати, К-фелдспат од типот микроклин, како и Na-Ca плагиокласи на албит-олигоклас, неколку видови дијатомеи, како и минорни количини кварц, железоносни минерали и други микроелементи, сите вклопени во седиментни слоеви, дијатомејската земја покажува особини кои целосно одговараат на некои барања од апликативната лепеза. Утврдени се исклучително позитивни термоизолациони карактеристики на компактни сегменти од суровината, пожелни за градежната индустрија, како и можноста за едноставно механичко конфекционирање. Од другите испитувања на хемискиот и минералошкиот состав, димензиите на примарните честички и можностите за механичка трансформација, утврдени се параметри кои несомнено упатуваат на можна примена на материјалот во областите на земјоделието (како еколошка заштита на растенијата од инсекти и нематоди, подобрувач на почвата и регулатор на pH, пасивна деконтаминација на почва), а секако и за примена во процесите на филтрација на вода за пиење и отпадна вода, како и други флуиди.

Клучни зборови: дијатомејска земја; Славишко Поле; термоизолациони карактеристики; еколошка заштита од инсекти

1. INTRODUCTION

Diatomaceous earth (DE) is a naturally occurring complex sediment composed of the fossilized remains of diatoms, a class of unicellular algae characterized by intricate silica-based exoskeletons, commonly known as frustules [1–3]. It has unique physicochemical properties, including exceptionally high porosity, low bulk density, and a high specific surface area. Diatomaceous earth exhibits remarkable utility across diverse industrial applications [4–8]. The majority of research on DE focuses on the analysis of its individual components, including its diverse exoskeletal morphologies and its high silica content. The morphological diversity observed among diatoms suggests the potential for multifunctionality, particularly in interactions with a broad spectrum of pathogens. Notably, detailed structural examinations of these frustules provide valuable insights in fields such as biomedical engineering, water purification, and agricultural enhancements, reinforcing the long-held principle that form is inherently dictated by function [9–14]. In 2023, the United States remained the predominant global producer of diatomaceous earth, contributing an estimated 32% of total worldwide output. Denmark followed with a 17% share, while China, Turkey, and Argentina, along with Mexico and Peru, accounted for approximately 10%, 8%, and 4% each, respectively. Furthermore, DE extraction occurred on a smaller scale in 19 additional countries [15]. Among these, North Macedonia possesses substantial DE reserves. The economic viability of DE sourced from North Macedonia is primarily attributed to its fine microstructure and, more significantly, its high content of non-crystalline (amorphous) silica [16–19]. This structural characteristic enhances the material's reactivity, making it particularly advantageous for various applications. The objective of this research is to systematically analyze key fundamental and main characteristics of diatomaceous earth, with the aim of facilitating its optimized utilization in specialized and application-specific contexts.

2. MATERIALS AND METHODS

In the geographical map and satellite image (Figures 1 and 2), the location of Slaviško Pole and the broader area from which diatomaceous earth samples were collected are marked. Slaviško Pole is situated within the contact zone between the Kratovo-Zletovo region and the Serbo-Macedonian Massif. The sampling points are predominantly located along the edges of the former Pliocene lake, where the concentration of diatoms in the overall mass is lower compared to the lower-lying areas of the present-day basin.

The samples collected for analysis are shown in Figure 3 and originate from multiple locations within the site.

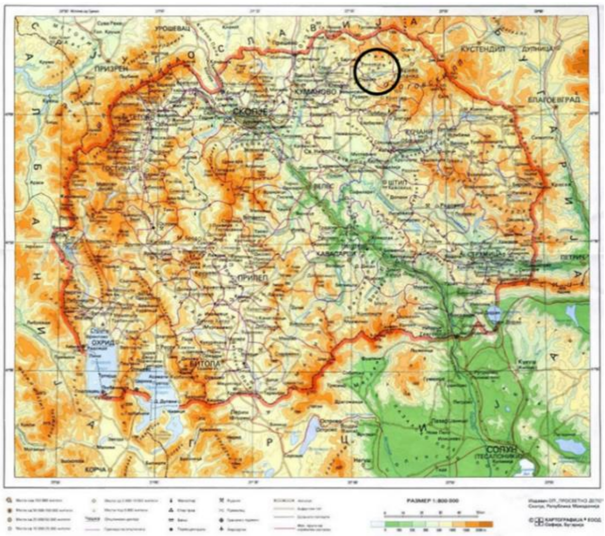

Fig. 1. Geographical location of Slaviško Pole

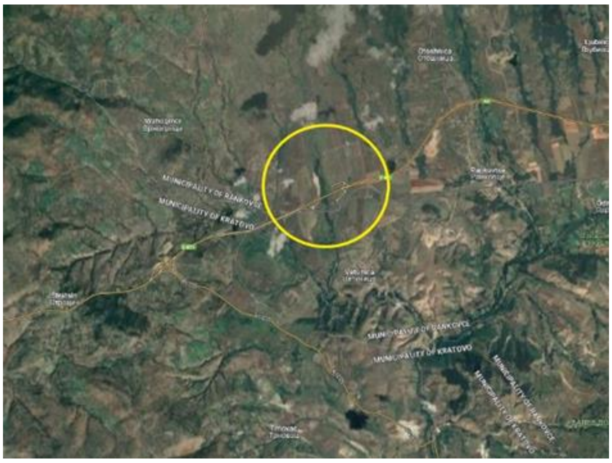

Fig. 2. Satellite image of Slaviško Pole

Fig. 3. Samples of diatomaceous earth from the corresponding sampling points

According to previous studies, X-ray diffraction analysis and transmission optical microscopy reveal the following mineralogical characteristics of this material: a dominant content of fine-grained feldspars (K-feldspar of the microcline type, as well as Na-Ca plagioclases of albite-oligoclase), a significant percentage of amorphous or cryptocrystalline mass, and several species of diatoms [20].

The diatoms, as a component of this material, were identified using transmission optical microscopy (SM-POL type, Letz-Wetzlar, Germany). The chemical composition was determined through silicate chemical analysis with alkaline melting of each fraction, with the fractions obtained via wet sieve analysis following a grinding process (without the presence of porcelain balls) in a porcelain mill for one hour. The presence of trace elements was determined using ICP-MS (Model 7850, Agilent Technologies). Physico-chemical examinations were conducted with standard laboratory equipment, determining specific mass, bulk density, water absorption, open, closed, and total porosity, and compressive strength in both raw and annealed states (ZRMK Ljubljana HPM 400). To determine the size and morphology of the primary grains, SEM analysis (JEOL JSM 35 CF) with an X-ray analyzer (TRACOR NORTHERN TN – 2000) was applied. The characteristic thermal insulation capacity was defined through a custom-designed laboratory test.

3. RESULTS AND DISCUSSION

The granulometric analysis was conducted using a set of sieves with perforation size of 0.1 mm, 0.071 mm, 0.045 mm, and 0.032 mm, following the grinding process in a porcelain mill (without the presence of porcelain balls) for one hour. The obtained results are presented in the histogram shown in Figure 4.

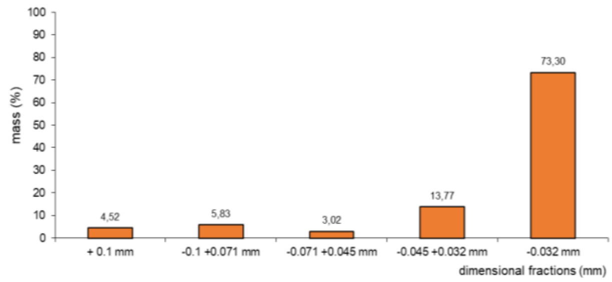

Fig. 4. Histogram of mass content of various dimensional grain fractions after 1 hour milling

Silicate chemical analysis with alkaline melting was performed on each of the dimensional fractions to determine the distribution variations of each component. The results are presented in Table 1.

T a b l e 1

Chemical composition of various dimensional grain fractions (mass %)

	+0.1 mm	–0.1 +0.071 mm	–0.075 +0.045 mm	–0.045 +0.032 mm	–0.032 mm
SiO_2	62.96	60.80	60.96	61.90	64.84
Fe_2O_3	15.96	16.06	15.95	16.16	9.22
Al_2O_3	2.88	2.95	2.90	2.85	6.01
CaO	6.10	7.40	7.40	6.90	3.80
MgO	1.97	2.75	2.70	2.55	1.78
Na_2O	2.61	2.72	2.51	2.72	1.80
K_2O	3.73	4.24	4.24	3.73	1.94
SO_3	tr.	tr.	tr.	tr.	tr.
l.w.	2.92	2.16	2.36	2.33	9.65
Σ	99.13	99.08	99.02	99.14	99.04

From the chemical analysis, it can be concluded that in the finest fraction, the content of alkaline oxides, which are indicators of the presence of feldspars, drastically decreases. Another characteristic of the finest fraction is the highest content of SiO_2 and Fe_2O_3, while, conversely, there is a drastically lower concentration of Al_2O_3. The highest value for weigh loss of ignition at 600°C predominantly originates from the content of organic matter, as shown in Table 2, where the finest fraction contains the dominant content of organic matter in the total mass of the material. The content of trace elements is presented in Table 3.

Table 2

Total content of organic matter (mass %)

Dimensional fraction (mm)	Organic matter content, 600°C (mass %)
+ 0.1	1.72
–0.1 +0.071	0.97
–0.071 +0.045	0.77
–0.045 +0.032	1.12
–0.032	7.34

Table 3

ICP-MS analysis, content of trace elements (ppm)

Element	(ppm)
Ag	<1
Al	39679.60
As	7.10
B	23.86
Ba	337
Ca	15053.90
Cd	<1
Co	<1
Cr	8.95
Cu	25.09
Fe	30398.40
K	12158.90
Li	4.70
Mg	1948.56
Mn	2
Mo	<1
Na	0
Ni	3.82
P	2
Pb	33.93
Sr	0
V	49.80
Zn	79.58

The basic mass of the material is predominantly cryptocrystalline, with quartz and feldspar grains occasionally found in the size range of 0.005–0.01 mm and 0.05–0.1 mm (Figure 5). The feldspar mass is represented by polysynthetic lamellae of plagioclases of the albite-oligoclase type (Figure 6). Within the basic mass, diatom skeletons were also found, exhibiting an elongated shape with longitudinally connected segments measuring approximately 100 µm (Figure 7). Another type of diatom is shown in Figure 8. These skeletons are symmetrically separated longitudinally at the center and represent silicate spicules of the spongolite type. The identification of microfossils in this sediment was carried out through comparative analysis of identical species, which are well-known according to the literature data [21], and *Melosira undulata* [22].

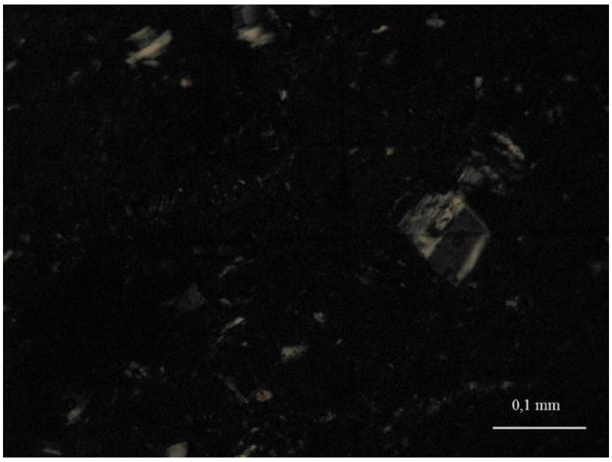

Fig. 5. Photograph of transmissional optical microscopy. Minor crystalline phase in the base mass (N+)

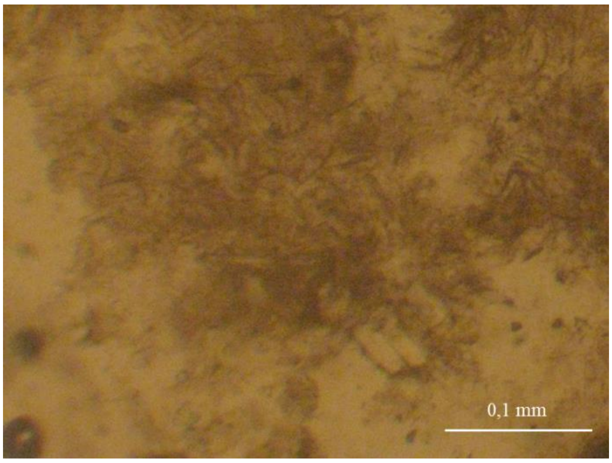

Fig. 6. Photograph of transmissional optical microscopy. Polysynthetic lamellae

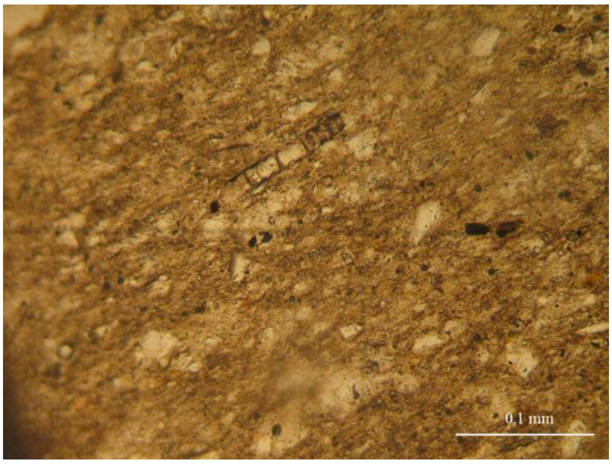

Fig. 7. Photograph of transmissional optical microscopy. Typical longitudinal section of diatoms (*Melosira undulata*) incorporated into basic fine-grained cryptocrystalline amorphous opal mass, in which round grains of feldspar and quartz coexist

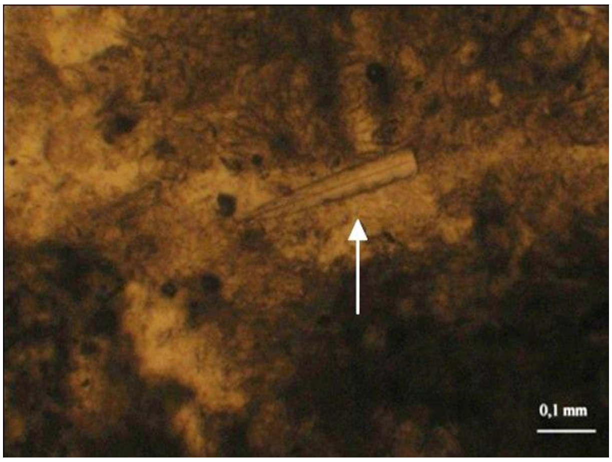

Fig. 8. Photograph of transmissional optical microscopy. *Spongolite spicule* incorporated into cryptocrystalline amorphous opal mass (N+)

Further examinations were conducted to assess certain physico-chemical characteristics, which were divided into several segments. The following physico-mechanical and physico-chemical analysis were performed on the compact sedimentary material of diatomaceous earth: specific mass, bulk density, water absorption, open, closed, and total porosity, and compressive strength. These analyses were carried out on the material in its raw state, treated at 600°C for 2 hours and treated at 800°C for 2 hours. The results of these tests are presented in Table 4.

Table 4

Physical characteristics of the raw material

Physico-мechanical characteristics (properties)		Raw material	Treated at 600°C, 2h	Treated at 800°C, 2h
Specific mass (g/cm³)		2.511	2.533	2.558
Bulk density (g/cm³)		0.95	0.92	0.94
Water absorption (%)		61.46	62.99	62.72
Porosity (%)	Open	58.99	59.81	58.95
	Closed	2.82	2.69	4.30
	Total	61.81	62.50	63.25
Compressive strength (MPa)		7.22/7.30*	17.10	7.25

From the presented results for compressive strength, it can be concluded that the material retains its basic mechanical characteristics in all orientations, both in its original state and after being thermally treated at 600°C and 800°C. This data is significant for the application of diatomaceous earth in compact elements for construction, where it is required that the material, when processed to appropriate dimensions, remains self-supporting.

From the analysis conducted using SEM and EDS, as shown in Figure 9 and Table 5, the dimensions of the primary grains and their aggregates at multiple levels can be clearly observed. The composition is typical of the base mass, confirmed by the other methods.

The material's ability to function as a thermal insulator in its compact form was experimentally demonstrated as follows: a piece of the material, approximately 4 cm thick, was partially perforated from the backside at distances of 1, 2, and 3 cm measured from the front side (Figure 10). A thermal sensor was placed in the perforated holes while the material was heated from the opposite side using a propane-butane flame at a temperature of 850°C (Figures 11 and 12).

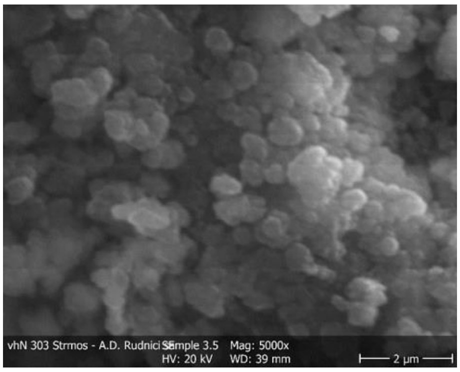

Fig. 9. SEM image of the diatomaceous earth sample

Fig. 10. Perforation of the material at different depths for the placement of the thermal sensor

Fig. 11. Segment of the experimental setup

Fig. 12. Treated sample after the thermal insulation experiment

Table 5

SEM-EDS composition

Components	Mass %
Na_2O	1.31
MgO	1.22
Al_2O_3	14.99
SiO_2	72.17
P_2O_5	0.52
SO_3	0.59
Cl	0.22
K_2O	1.84
CaO	2.55
TiO_2	0.85
MnO	0.11
FeO	3.52

The experiment lasted 60 minutes, and the results for all three measurements are shown in the diagram in Figure 13 and in Table 6.

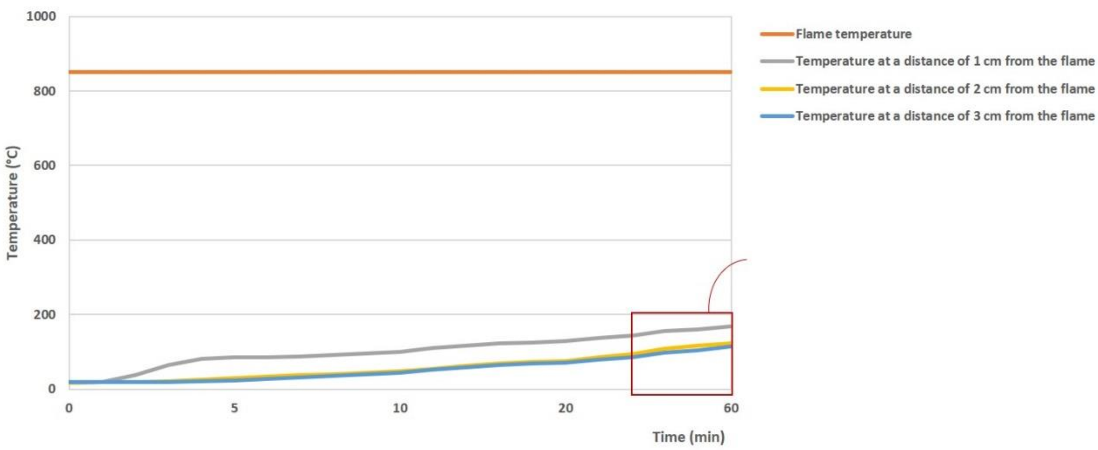

Fig. 13. Diagram of the heat transfer during the thermal treatment

Table 6

Data from the experiment on thermal insulation characteristics

Time (min)	Temperature at a distance of 1 cm from the flame	Temperature at a distance of 2 cm from the flame	Temperature at a distance of 3 cm from the flame
0	18	18.2	19.4
1	19.9	18.4	19.7
2	38.0	19.1	19.6
3	64.0	21.7	20.1
4	82.0	25.7	21.4
5	85.0	29.9	24.0
6	85.0	34.5	27.5
7	88.0	38.0	31.5
8	92.0	41.0	36.1
9	97.0	45.2	39.9
10	101.0	47.3	45.0
12	110.0	55.1	52.3
14	116.5	62.0	59.6
16	122.1	68.1	64.9
18	125.0	73.1	69.9
20	130.0	75.8	72.0
25	136.5	84.8	78.5
30	143.1	93.3	85.3
40	156.0	107.5	99.0
50	160.6	117.0	103.5
60	169.5	124.0	114.9

The results show an exceptionally high thermal insulation property of the compact material, as it maintains a ΔT value higher than 700°C during the 1 hour exposure to the maximum temperature on the other side. This effect of extremely high thermal insulation capability primarily originates from the material's porosity. The distinct separation of curves from the experimental values at 1 cm distance compared to those at 2 and 3 cm results from the following effect: at the first curve, the influence of the porosity of the basic mass dominates, but since the material is sedimentary, with different layers on its contact surface showing varying characteristics during heating, layer separation occurs within the still compact material. These separation segments, as air barriers, further increase the thermal insulation ability. As heat penetrates deeper into the material, the subsequent sediment layers begin to separate due to thermal expansion, with noticeable separation of the curves at 2 and 3 cm, where the next layer starts to open (Figure 14).

The separation of layers during thermal treatment results from the relatively different composition of individual layers, which exhibit different properties as a consequence. For example, the presence of divalent iron in larger or smaller quantities, during its transformation into trivalent iron during the thermal treatment, contributes to the tendency for layer separation. The higher presence of iron in some sediment layers is visually represented by a piece/segment of diatomaceous earth thermally at 800°C, where the higher or lesser presence of iron in different layers is visually noticeable (with varying colour intensity), as clearly shown in Figure 15.

Fig. 14. Profile of the treated compact sample for thermal insulation experiment

Fig. 15. Thermally treated diatomaceous earth sample at 800°C for 2 hours (in an oxidizing atmosphere)

CONCLUSIONS

Based on the obtained results from the conducted physico-chemical and mineralogical analyses, as well as previous studies on the diatomaceous earth from Slaviško Pole, the following can be concluded:

The diatomaceous earth from the mentioned locality of Slaviško Pole, predominantly consists of K-feldspar of the microcline type, as well as Na-Ca plagioclases of albite-oligoclase type, along with specific diatom species (silicate spicules of the spongolite type and *Melosira undulata*), interspersed with minor quantities of quartz within a cryptocrystalline matrix.

The chemical composition has been determined across all fractions obtained from the wet sieve analysis, providing insight into the distribution of constituent elements within each fraction. Notably, the highest content of organic matter is determined in the finest fraction (–32 µm), which also exhibits an increased SiO_2 content, as a consequence of higher content of diatoms.

According to the results of the physical-mechanical tests, the compact mass of diatomaceous earth from this locality demonstrates highly favourable properties that align with the requirements of the construction industry. Key attributes include: the feasibility of segmenting elements of relatively large dimensions along sedimentary planes (allowing for processing with minimal energy input); high compressive strength across various orientations (ensuring self-supporting structural integrity); exceptional high thermal insulation capacity (with a temperature gradient of approximately ΔT 700°C over a 1 cm distance within one hour); and resistance to high temperatures without emitting hazardous volatile substances.

The morphology and dimensions of the primary particles/grains (200 – 300 nm), along with their aggregated forms, suggest that this material holds potential as a natural, eco-friendly means of plant protection against specific insect and nematode species. The abrasive action of the diatomaceous earth mechanically affects the exoskeletal joints of insects, while the diatom content induces dehydration in nematodes, thereby reducing their viability.

The combination of open porosity, particle size distribution, absorption and adsorption properties, and chemical stability unequivocally meets the criteria for filtration applications in both potable and waste water treatment. Additionally, this material is well-suited for emergency interventions requiring the removal of hazardous fluids from the environment. Furthermore, when processed into an appropriate granulometric distribution, it can serve as an effective medium for the passive remediation of soils contaminated with heavy metals, leveraging its cation-exchange capacity.

REFERENCES

[1] Wang, Z. Y., Zhang, L. P., Yang, Y. X. (2009): Structural investigation of some important Chinese diatomites, *Glass Physics and Chemistry*, **35** (6), 673–679. DOI: 10.1134/S1087659609060182

[2] Zhang, D. Y, Wang, Y., Cai, J., Pan, J. F., Jiang, X. G., Jiang Y. G. (2012): Bio-manufacturing technology based on diatom micro- and nanostructure, *Chinese Science Bulletin*, **57** (30), 3836–3849. DOI: 10.1007/s11434-012-5410-x

[3] Karaman, E. S., Wang, Z., Di Benedetto, G., Zunino, J. L., Meng, X., Mitra, S. (2019): Fabrication of supercapacitors and flexible electrodes using biosilica from cultured diatoms, *Materials Today Energy*, **11**, 0166–173. DOI: 10.1016/j.mtener.2018.11.004

[4] Hu, Z., Zheng, S., Li, J., Zhang, S., Liu, M., Wang, Z., Li, J., Sun, H. (2022): Pore structure and surface properties of diatomite with mechanical grinding and its influence on humidity control, *Physicochemical Problems of Mineral Processing,* **58** (6), 153509. DOI: 10.37190/ppmp/153509

[5] Li, B., Wang, T., Le, Q., Qin, R., Zhang, Y., Zeng, H. C. (2023): Surface reconstruction, modification and functionalization of natural diatomites for miniaturization of shaped heterogeneous catalysts, *Nano Materials Science*, **5** (3), 293–311. DOI: 10.1016/j.nanoms.2022.05.001

[6] Aggrey, P., Nartey, M., Kan, Y., Cvjetinović, J., Andrews, A., Salimon, A.I., Dragnevski, K.I., Korsunsky, A.M. (2021): On the diatomite-based nanostructure-preserving material synthesis for energy applications, *RSC Advances*, **11** (51), 31884–31922. DOI: 10.1039/d1ra05810j

[7] Villani, M., Onesto, V., Coluccio, M. L., Valpapuram, I., Majewska, R., Alabastri, A., Battista, E., Schirato, A., Calestani, D., Coppedé, N., Zappettini, A., Amato, F., Di Fabrizio, E., Gentile, F., (2019): Transforming diatomaceous earth into sensing devices by surface modification with gold nanoparticles, *Micro and Nano Engineering*, **2**, 29–34. DOI: 10.1016/j.mne.2018.11.006

[8] Wang, C., Li, K., Sun, Q., Zhu, S., Zhang, C., Zhang, Y., Shi, Z., Hu, Y., Zhang, Y. (2023): Diatomite-like $KFeS_2$ for use in high-performance electrodes for energy storage and oxygen evolution, *Nanomaterials*, **13** (4), 643. DOI: 10.3390/nano13040643

[9] De Stefano, M., De Stefano, L. (2005): Nanostructures in diatom frustules: functional morphology of valvocopulae in Cocconeidacean monoraphid taxa, *Journal of Nanoscience and Nanotechnology*, **5** (1), 15–24. DOI: 10.1166/jnn.2005.001

[10] Stanisz, M., Klapiszewski, Ł., Jesionowski, T. (2020): Recent advances in the fabrication and application of biopolymer-based micro- and nanostructures: a comprehensive review, *Chemical Engineering Journal*, **397**, 125409. DOI: 10.1016/j.cej.2020.125409

[11] Arfin, T. (2021): Emerging trends in lab-on-a-chip for biosensing application, *Functionalized Nanomaterials Based Devices for Environmental Applications,* 199–218. DOI: 10.1016/B978-0-12-822245-4.00008-8

[12] Zong, P., Makino, D., Pan, W., Yin, S., Sun, C., Zhang, P., Wan, C., Koumoto, K. (2018): Converting natural diatomite into nanoporous silicon for eco-friendly thermoelectric energy conversion, *Materials & Design*, **154**, 246–253. DOI: 10.1016/j.matdes.2018.05.042

[13] Zeni, V., Baliota, G. V., Benelli, G., Canale, A., Athanassiou, C. G. (2021): Diatomaceous earth for arthropod pest control: back to the future, *Molecules*, **26** (24), 7487. DOI: 10.3390/molecules26247487

[14] Wu, J., Yang, Y. S., Lin, J. (2006): Advanced Tertiary treatment of municipal wastewater using raw and modified diatomite, *Journal of Hazardous Materials*, **127** (1–3), 196–203. DOI: 10.1016/j.jhazmat.2005.07.016

[15] *Mineral commodity summaries 2024*. Reston, Virginia: US Geological Survey, 2024, pp. 68–69.

[16] Reka, A., Pavlovski, B., Fazlija, E., Berisha, A., Pacarizi, M., Daghmehchi, M., Sacalis, C., Jovanovski, G., Makreski, P., Oral, A. (2021): Diatomaceous earth: characterization, thermal modification, and application, *Open Chemistry*, **19** (1), 451–461. DOI: 10.1515/chem-2020-0049

[17] Reka, A., Anovski, T., Bogoevski, S., Pavlovski, B., Boškovski, B. (2014): Physical-chemical and mineralogical-petrograpic examinations of diatomite from deposit near village Roždеn, R. Macedonia, *Geologica Macedonica*, **28** (2), 121–126.

[18] Reka, A., Pavlovski, B., Anovski, T., Bogoevski, S., Boškovski, B. (2015): Phase transformations of amorphous SiO_2 in diatomite at temperature range of 1000–1200°C, *Geologica Macedonica*, **29** (1), 87–92.

[19] Reka, A., Pavlovski, B., Boev, B., Bogoevski, B., Boškovski, B., Lazarova, M., Lamamra, A., Jashari, A., Jovanovski, G., Makreski, P. (2021): Diatomite-evaluation of physico-mechanical, chemical, mineralogical and thermal properties, *Geologica Macedonica*, **35** (1), 5–14. DOI: 10.46763/GEOL21351368005ar

[20] Bogoevski, S., Jančev, S., Boškovski, B. (2014): Characterization of diatomaceous earth from the Slavishko Pole locality in the Republic of Macedonia. *Geologica Macedonica*, **28** (1), 39–43.

[21] Inglethorpe, S. D. J., Pearce, J. M. (1999): *Mineralogy and petrography of diatomite from the Lampang Basin, Changwat Lampang, northern Thailand*. Technical report. British Geological Survey, Nottingham, 1993.

[22] Kützing, F. T. (1844). *Die Kieselschaligen Bacillarien oder Diatomeen*. Nordhausen, 152 pp., 30 pls.

Mechanical Engineering – Scientific Journal, Vol. **43,** No. 1, pp. 49–57 (2025)
Number of article: 693
Received: April 24, 2025
Accepted: May 12, 2025
In print: ISSN 1857–5293
On line: ISSN 1857–9191
UDC: UDC: 621.313.13-133.2:534.242.089
https://doi.org/10.55302/MESJ2543149a

Original scientific paper

REAL-TIME VIBRATION ANALYSIS AND RESONANCE DETECTION OF STEPPER MOTORS

Medin Ademi, Maja Anačkova, Dejan Šiškovski

Faculty of Mechanical Engineering, "Ss. Cyril and Methodius" University in Skopje, P.O.Box 464, MK-1001 Skopje, Republic of North Macedonia
m.ademi2607@student.mf.ukim.edu.mk

A b s t r a c t: This paper focuses on developing a real-time system for vibration analysis and resonance detection in stepper motors used in CNC machines. The goal is to optimize motor performance and reduce resonance effects, which impact precision and efficiency. The ADXL345 accelerometer is mounted near the motor shaft to measure vibrations, while the Arduino Mega 2560 serves as an interface. Vibration data is processed in LabVIEW using FFT to analyze frequency and time domains. A potentiometer controls the motor speed, powered by an L298N driver. Additionally, an Arduino Uno reads the potentiometer input and adjusts the speed. The TCST1230 optical sensor measures the motor's RPM, allowing a detailed analysis of the relationship between speed and vibration frequencies. Results visualized in Excel help identify resonance frequencies, enabling better parameter selection. This system enhances the accuracy, efficiency, and longevity of CNC machines by minimizing harmful vibrations.

Key words: resonance detection; CNC machine; accelerometer; FFT; Arduino

РЕАЛНОВРЕМЕНСКА АНАЛИЗА НА ВИБРАЦИИ И ДЕТЕКЦИЈА НА РЕЗОНАНЦИЈА КАЈ ЧЕКОРНИТЕ МОТОРИ

А п с т р а к т: Овој труд се фокусира на развој на реалновременски системи за анализа на вибрации и детекција на резонанција кај чекорните мотори во CNC-машини. Целта е да се оптимизираат перформансите на моторот и да се намалат негативните ефекти од резонанција, која влијае врз прецизноста и ефикасноста. До вратилото на моторот е поставен акцелерометар ADXL345 за мерење вибрации, додека Arduino Mega 2560 служи како интерфејс. Податоците се обработуваат во LabVIEW користејќи FFT за анализа во фреквенциски и временски домен. Потенциометарот ја контролира брзината, додека драјверот L298N го напојува моторот. Дополнително, Arduino Uno го чита сигналот од потенциометарот и ја контролира брзината. Оптичкиот сензор TCST1230 ја мери брзината на моторот RPM, овозможувајќи анализа на врската меѓу брзината и вибрациите. Резултатите во Excel помагаат во идентификација на резонантните фреквенции, овозможувајќи подобар избор на параметрите и намалување на штетните вибрации во CNC-машините.

Клучни зборови: детекција на резонанција; CNC-машина; акцелерометар; FFT; Ардуино

1. INTRODUCTION

Over the years, stepper motors have evolved significantly, with their commercial adoption beginning in the 1960s. This was largely due to advancements in silicon wafer fabrication, which enabled the development of devices capable of switching high DC currents in motor windings. Initially, stepper motors were not considered a viable alternative to AC or DC servomotors because of their limited high-speed performance. However, as noted by Stout (2000), improvements in motor design and drive systems have made stepper motors highly effective actuators in digital control systems. Their operation can be described as inherently digital, as the rotor moves in precise, discrete steps when the motor windings are energized [1].

Stepper motors enable various operating modes, such as Fullstepping, Halfstepping, and Microstepping, which play a crucial role in their use in different applications (CNC machines, robotic arms, 3D printers, etc.). In the context of research on frequency resonance detection, the characteristics of the Fullstepping mode are of particular importance and will be used in this study. Below Table 1 is a explaining the different operating modes and their characteristics based on the specifications provided in the QSH4218 stepper motor datasheet [2].

Table 1

Different operating modes of stepper motors and their characteristics

Driver scheme	Resolution	Velocity range	Comment
Fullstepping	200 steps per rotation	Low to very high. Skip resonance areas in low to medium velocity range	Audible noise and vibrations especially at low velocities
Halfstepping	200 steps per rotation*2	Low to very high. Skip resonance areas in low to medium velocity range	Audible noise and vibrations especially at low velocities
Microstepping	200*(number of microsteps) per rotation	Low to high	Low noise, smooth motor behavior
Mixed: Microstepping and Fullstepping for high velocitites	200*(number of microsteps) per rotation	Low to very high	At high velocities, there is no audible difference for fullstepping

When a step motor is driven in the open-loop mode, pronounced velocity oscillations are observed in certain input frequency ranges (steps/sec). In the low-frequency range, the step motor exhibits substantial oscillations at or near the natural frequency and its subharmonics. This phenomenon, known as "low-frequency resonance", is well-documented in the literature. According to Higuchi, Mizuno, and Oshima (1981), this resonance occurs due to the interaction between the motor's mechanical inertia and the electromagnetic forces generated during operation [3]. In this study, resonance is detected by comparing the input frequency (derived from the optic sensor measuring RPM) with the vibration frequency (measured using the ADXL345 accelerometer). When these frequencies align, the system enters a resonant state, leading to increased vibrations and oscillations, as predicted by the theoretical framework described in [3]. Resonance in stepper motors can significantly affect their stability, particularly at certain speeds, leading to unstable torque output. A common issue in motion control systems is the occurrence of vibrations at low speeds, which become especially pronounced when the motor operates near its resonance frequency. As demonstrated by Arva, Stanica, and Anghel (2018) [4], one of the primary causes of these vibrations is cogging torque, which arises from the interaction between the permanent magnet poles and the stator, generating unwanted oscillations. As the input frequency approaches the motor's natural frequency, the system may initially appear to function normally; however, speed oscillations eventually emerge. This oscillatory behavior typically becomes noticeable at frequencies higher than several hundred steps per second. In the literature, this phenomenon is commonly referred to as "medium frequency resonance" or "high frequency resonance". When the motor operates within its resonance frequency range, a sudden drop in available torque is observed, and the torque does not recover to its previous level. This effect, referred to as a torque drop on the torque-speed curve, severely limits the motor's operational performance [4]. Additionally, Kenjo and Sugawara (1994) [5] highlight that the resonance phenomenon is exacerbated by the nonlinear dynamics of the motor's rotor-stator interaction, particularly in open-loop control systems where feedback compensation is absent [5]. In the context of CNC machines, resonance can have detrimental effects on machining accuracy and surface finish. As noted by Altintas and Weck (2004) [6], vibrations caused by resonance in stepper motors can propagate through the machine structure, leading to chatter and poor surface quality in machined parts [6]. This is particularly critical in high-precision CNC applications, where even minor oscillations can result in dimensional inaccuracies and increased tool wear. Smith et al. (2020) [14] further emphasize that resonance-induced vibrations in CNC systems can lead to reduced machining efficiency and higher energy consumption, highlighting the need for effective resonance suppression techniques [7].

The study underscores the importance of mitigating resonance in CNC systems to ensure optimal performance and product quality. The present paper is structured as follows: The second section presents the operating mode and connections required to drive the stepper motor. The third section explains the selection of the sensor. The fourth section presents the experimental setup and experimental results, while the final section is reserved for conclusions.

2. STEPPER MOTOR CONNECTIONS

a) *Stepper motor calculations*

The stepper motor's behavior is a critical factor in the Arduino coding process, and its implementation depends on the specific type of motor selected. As described in the research by Harun and Lim, to calculate the number of steps required for the motor to complete one full revolution, the following equation is used. For most standard stepper motors, the step angle is 1.8 degrees per step, which translates to 200 steps per revolution [8].

$$\frac{360\,Degree}{1\,Revolution\ \frac{Degree}{Step}} = \frac{Step}{Revolution}$$

As mentioned at the beginning, there are different operating modes for the stepper motor, but for the purpose of this study, we use the mode that is most suitable for vibration detection and frequency resonance analysis, which is the Full-step mode. This operating mode ensures a constant angular position of 1.8° per step. In our case, with an angle of 1.8° per step, the number of steps per revolution will be:

$$\frac{360°}{1{,}8\,°} = 200\ steps/revolution$$

For this research, a NEMA17 stepper motor (model QSH4218-35-10-027) was utilized. According to the datasheet documentation (see Figure 1), the wiring layout and the configuration of the two windings were identified, which is critical for ensuring correct motor connections.

Fig. 1. Documentation of the datasheet for stepper motor NEMA17 QSH4218-35-10-027

The motor is equipped with UL 1007 wires, which have a thickness of AWG26. This wire specification is vital for maintaining sufficient electrical conductivity and minimizing resistance within the system. These parameters are particularly significant in this study, as proper electrical connectivity and reduced losses are essential for obtaining precise motor speed measurements [9].

b) *Stepper motor connections*

One of the critical aspects of stepper motor applications is the selection of a suitable driver for motor control. Operating a stepper motor involves switching the current between the stator windings, a function managed by the driver, which regulates and amplifies the control pulses. For this study, the L298N driver was integrated to power the motor, serving as the central component of the motion control hardware system. Based on the methodology outlined in Muain (2010) [10], the L298N driver acted as a power interface, enabling synchronization between the microcontroller and the NEMA17 stepper motor. Powered by a 12 V and 2 A adapter, the L298N efficiently regulated and amplified the voltage and current, ensuring optimal motor performance. The motor windings were connected to the designated A and B pins on the L298N driver, following the connection scheme described in Muain (2010). Additionally, the control pins were carefully linked to the corresponding pins on the Arduino, establishing a reliable communication pathway. To connect all components, 6 female-to-male jumper wires and 3 male-to-male jumper wires were used. A stable electrical environment was achieved by grounding the negative pins together with the Arduino’s ground, as recommended in the referenced research [10]. To control the speed of the stepper motor, a 100 kΩ potentiometer was used, enabling precise speed regulation, which is essential for vibration measurement. In this setup, an Arduino UNO was implemented, powered via an adapter, and served as the central control unit for managing the motor's operation. The connection diagram, including the L298N driver, stepper motor, potentiometer, and all necessary pins from the Arduino UNO, is shown in Figure 2.

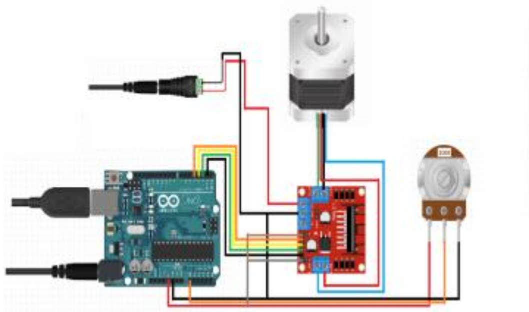

Fig. 2. Connection diagram of the stepper motor, L298N driver, Arduino UNO, and potentiometer

3. ADXL345 ACCELEROMETER

The selection of the sensor is crucial for achieving accurate results, with requirements for stable performance and a good frequency response. According to the study by Rodrigues et al. (2021) [11], Micro-Electro-Mechanical Systems (MEMS) are microdevices that combine mechanical and electrical properties, creating an interface between mechanical and electronic phenomena at a microscopic level. Accelerometers developed using this technology consist of three main components: (i) a seismic mass, (ii) a system of micro-springs that attach the mass to the circuit substrate, and (iii) a system of multiple parallel plate capacitors. When the seismic mass is subjected to acceleration, the springs allow the lateral plates of the mass to move into the dielectric region of the capacitors. The presence of this material within the electric field causes a variation in the system's capacitance, generating an electrical disturbance that can be detected by measuring the electric current between the plates in an intermediate circuit [11].

The ability of an accelerometer to provide reliable responses under mechanical excitation is determined by five key criteria:

i) Sensitivity, which relates the intensity of the electrical signal (in V) to the amplitude of vibrations;

ii) Frequency range, which defines the range of frequencies supported by the circuit;

iii) Maximum supported vibration amplitude, which indicates the highest vibration level the accelerometer can measure;

iv) Shock limit, which specifies the maximum acceleration the MEMS device can withstand;

v) Linearity, which reflects how well the accelerometer's responses align with a specific mathematical model within the supported frequency range.

The analysis of these characteristics, combined with the implementation costs, is ideal for selecting the most suitable accelerometer for our application. A list of key specifications for the desired application has been established, as shown in Table 2. The acceleration range was determined based on research by Saponara et al. (2015) [12]. The bandwidth, or frequency range, is a critical factor in determining which sensor to use. For digital MEMS sensors, the bandwidth is limited to half the data transmission rate of the signal processing circuit to satisfy the Nyquist frequency criterion. The operating temperature is also significant, as high temperatures can occur during the operational mode of the stepper motor.

T a b l e 2

Desired sensor specification

Specification	Min	Max
Brandwidth	50Hz	1kHz
Interface	Digital or analog	N/A
Operating temperature	–10°C	70°C
Acceleration range	0.5g	5g
Noise density	Og/√Hz	10mg/√Hz
Cross axis sensitivity		
Cost	0	$150

With these key characteristics in mind, a selection of commonly available sensors has been evaluated in Table 3. All of these sensors come premounted on development boards that include basic circuitry and connection terminals. They are all designed to function within a temperature range of -40°C to +85°C, making them well-suited for the intended application.

T a b l e 3

Comparision of MEMS sensors for vibration measurement

Sensor	Band. width. Hz	Interface	Noise Density mg/√Hz	Cost ($)
ADXL345	6.25 to 1600	SPI / I2C	3.9 31.2	84
ADXL343	0.1 to 1600	SPI	4.2 34.3	60
ADIS16209	0 to 50	SPI	0.19	161
ADXL375	0 to 1000	SPI / I2C	5	60
LIS331AL	0 to 1000	Analog	0.3	71
BMA150	25 to 1500	I2C	0.5	42

From the analyzed MEMS sensors, the most suitable for measuring vibrations on a stepper motor is the ADXL345, as it meets all the required criteria. The ADXL345 (Figure 3) is a compact 3 mm × 5 mm × 1 mm device with a selectable measurement range of ±2 g, ±4 g, ±8 g, and ±16 g. For this application, the ±2 g range is used, as it offers the highest resolution, which is ideal for detecting small vibrations in the stepper motor. It features a 32 level FIFO buffer, reducing microcontroller interaction and saving power. The block diagram below shows the 3 axis MEMS sensor, ADC, digital filter, and FIFO buffer. It supports SPI and I2C communication, has interrupt logic for event detection, and includes a power management system for efficient operation.

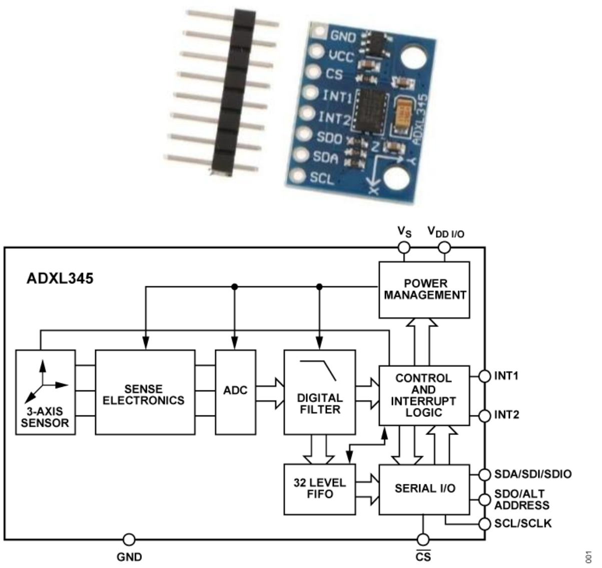

Fig. 3. ADXL345 sensor module and block diagram

4. EXPERIMENTAL SETUP

a) *Hardware setup and description*

The hardware setup shown in Figure 4 consists of a stepper motor (NEMA17), Arduino UNO, Arduino mega 2560, L298N driver, ADXL345 and TCST1230 optic sensor. The optical sensor is mounted on one of the mounting holes of the stepper motor to measure RPM. A metal disk with a hole is attached to the motor shaft, and the optical sensor detects this hole to monitor the rotational movement. Additionally, the ADXL345 accelerometer is mounted on the other mounting hole of the stepper motor, allowing it to capture more accurate data for the RPM measurement. The experimental setup works as follows: The Arduino Mega 2560 is responsible for signal processing through LabVIEW. It communicates with the sensors via the SDA and SCL pins, collecting data from both the optical sensor (for RPM measurement) and the ADXL345 accelerometer (for more precise motion data). The data is processed in LabVIEW using FFT blocks to analyze the signals in both the time and frequency domains. This enables the display of RPM and other relevant metrics on the LabVIEW front panel. The Arduino UNO is used to drive the stepper motor, with a potentiometer allowing the motor's speed to be varied from minimum to maximum in order to detect resonance frequencies. The optical sensor monitors the RPM, which is then displayed on the LabVIEW front panel through a gauge.

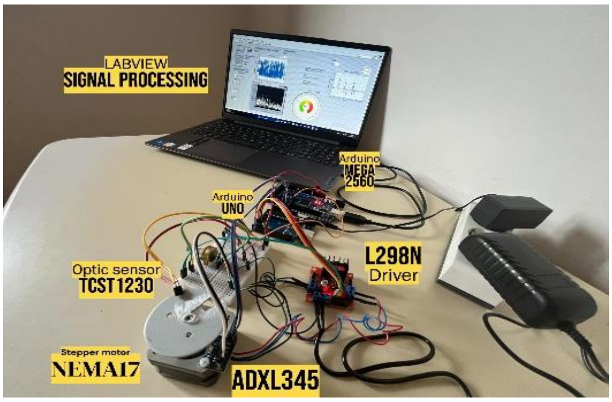

Fig. 4. Hardware setup

b) *Signal processing and FFT implementation in LabVIEW*

For measuring the vibrations of a stepper motor using LabVIEW and Arduino Mega 2560, the Fast Fourier Transform (FFT) is essential for signal processing. Several parameters in the Virtual Instrument (VI) play a key role in obtaining accurate measurements. The sampling frequency (f_s) defines the number of measurements or samples taken per unit of time during the digitization of the analog signal, and it must be greater than twice the highest frequency of the vibration signal to avoid aliasing (false frequency). The FFT size ($\underline{N}$) determines the number of points used for the FFT calculation, directly affecting both the frequency resolution ($\Delta\underline{f}$) and the computational load. Specifically, a larger FFT size allows for a finer frequency resolution, but it also demands more computation time. For example, when the sampling frequency (f_s) is set to 3.7 Hz and the FFT size (N) is 1024, the frequency resolution is calculated as shown in the literature by National Instruments (2020), where the relationship between f_s, N, and frequency resolution is described in detail [13].

$$\Delta f = \frac{fs}{N} = \frac{3{,}7}{1024} = 0.00361 \text{ Hz}$$

This implies that we can distinguish frequencies with very small differences, which is particularly important when analyzing vibrations with closely spaced frequency components. The chosen parameters f_s = 3.7 Hz and N =1024 are suitable because they provide sufficiently high resolution for analyzing the vibrations of the stepper motor, whose operating frequency ranges from 0 to 1.8 Hz. The sampling frequency f_s = 3.7 Hz is greater than twice the highest frequency of the signal (1.8 Hz × 2 = 3.6 Hz), meaning it satisfies the Sampling Theorem and ensures accurate reconstruction of the signal's frequency components without aliasing. With this configuration, the stepper motor's vibrations can be precisely analyzed in both the time domain using the Time Graph and in the frequency domain using the Frequency Graph.

5. RESULTS AND DISCUSSION

a) *Vibration analysis along the X-axis*

In the experimental setup, the ADXL345 accelerometer is mounted on the stepper motor's mounting hole, with its X and Y axes aligned horizontally, while the Z-axis is oriented vertically. Exeriments were first conducted at lower speeds, 20 and 40 RPM, to analyze resonance effects. At these speeds, resonance was detected, causing the motor to stop due to mechanical instability. FFT analysis shown in Figure 5 revealed resonant frequencies of 1.40 Hz (20 RPM) and 1.60 Hz (40 RPM), while the calculated rotational frequencies of the motor were 0.30 Hz and 0.67 Hz, respectively. This occurred due to the alignment of natural vibration frequencies with harmonics generated by the motor's rotation, amplifying vibrations and leading to instability. Figure 5 also shows amplified vibrations in the time domain, particularly along the X-axis, further confirming the presence of resonance. These data clearly indicate that at 20 RPM and 40 RPM, the system enters a critical operating mode, leading to significant mechanical disturbances and motor stoppage. Meanwhile experiments at higher speeds were also conducted, 60 and 120 RPM, where the frequency graph revealed dominant frequency which exactly matched the calculated rotational frequency. Unlike the previous speeds where resonance occurred, this time the motor continued to operate without interruptions.

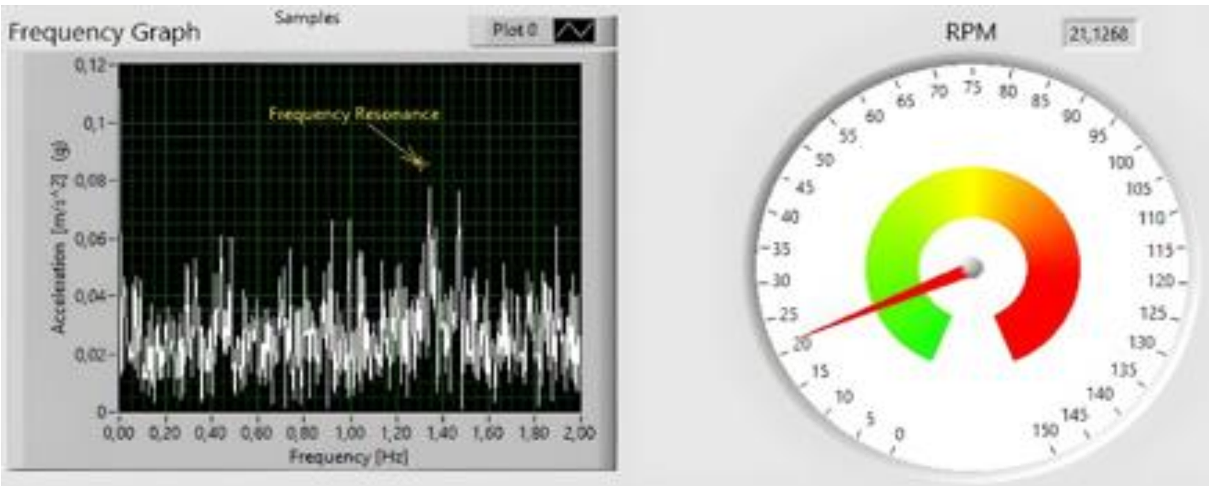

Fig. 5. Analysis of stepper motor vibrations at 20 RPM

b) *Vibration analysis along the Y-axis and Z-axis*

After completing the experiments around X-axis, experiments were further conducted around the Y-axis, following the same approach as before, starting with lower speeds 20 and 40 RPM. FFT analysis shown in the Figure 6, revealed a resonant frequency of 1.40 Hz (20 RPM) and 1.20 Hz (40 RPM), while the calculated rotational frequencies of the motor were 0.35 Hz and 0.67 Hz, respectively. Similar to the observations along the X-axis, this overlap between the system's natural frequency and the harmonics generated by the motor's rotation led to the occurrence of resonance. The consequences of resonance were clearly visible: the motor exhibited significant instability and eventually stopped functioning completely. In the time domain, pronounced oscillations were observed, particularly along the Y-axis, further confirming the presence of resonance. To ensure system stability and safety, it is essential to avoid resonant frequencies. Following the experiments around speeds of 60 and 120 RPM. Similar to the results along the X-axis, the frequency graph revealed a dominant frequency that exactly matched the calculated rotational frequency. At these speeds, the motor continued to operate stably without interruptions, unlike the lower speeds where resonance occurred. This indicates that the system avoided resonance conditions, allowing for stable operation. The absence of significant amplitude changes in the frequency spectrum and the balanced vibration distribution along the *Y*-axis further confirmed the system's stability under these conditions, consistent with the findings for the *X*-axis. In the analysis of vibrations around the *Z*-axis, it was observed that no significant oscillations occurred. This is due to the orientation of the ADXL345 sensor, which is positioned such that the Z-axis is directed upward and aligned with the coordinate origin. As a result, the motor does not exhibit acceleration or movement in this direction. This configuration ensures that all vibrations measured along the *Z*-axis are minimal or negligible. This configuration ensures that all vibrations measured along the Z-axis are minimal or negligible. The measurements along all three axes (*X*, *Y*, and *Z*) align with findings in the research by Smith et al., where multi-axis vibration analysis is commonly employed to assess system dynamics and resonance conditions [14].

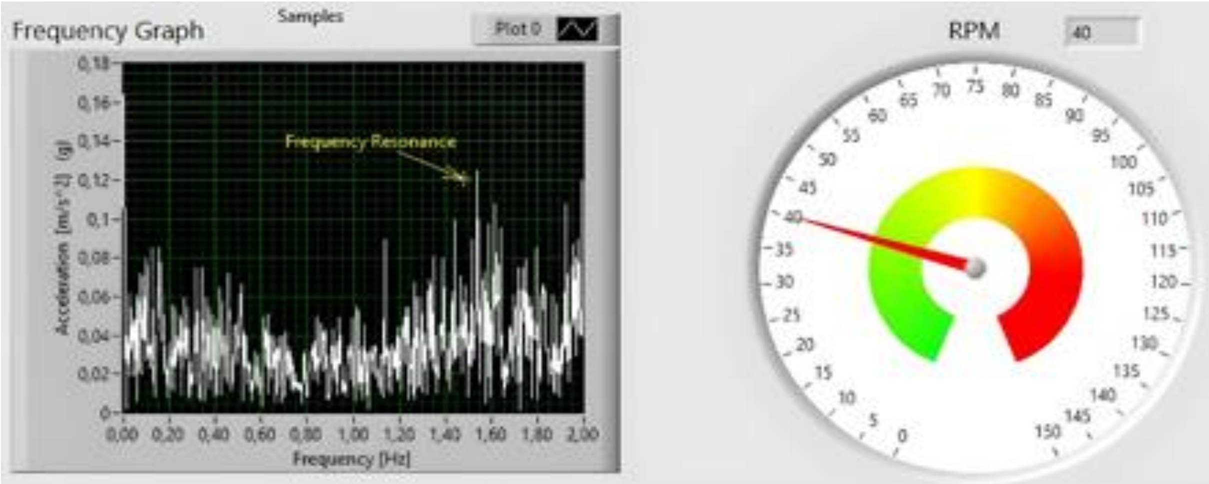

Fig. 6. Analysis of stepper motor vibrations at 40 RPM

6. CONCLUSION

From the measurements conducted around the X-axis and Y-axis, it has been confirmed that resonance occurs only at low motor speeds. This was initially mentioned when explaining the operational mode of the stepper motor, where in fullstepping mode at low speeds, frequency resonance occurs, leading to the interruption of the motor's rotation. The results of the analysis clearly show at which RPM values frequency resonance occurs. In Figure 7, similar to the findings of Zhang et al. [15], who investigated RPM-frequency relationships in CNC machines using stepper motors, the graph illustrates the relationship between RPM and frequency, demonstrating that at low speeds, specifically 20 RPM and 40 RPM (Figure 8), frequency resonance occurs (causing the motor to stop), while at higher speeds of 60 RPM and 120 RPM, the motor operates without interruptions. This is particularly important for CNC machines, where operating at speeds that match resonant frequencies can lead to mechanical instability, reduced precision, and potential damage. Therefore, it is not recommended for CNC systems to operate at speeds that align with these resonant frequencies. One of the major limitations of research within this field is the fact that the influence of temperature on the sensor. It has been observed that the stepper motor generates significant heat during operation, which directly impacts the precision of the measurements. The increase in temperature can cause changes in the sensor's characteristics, resulting in inaccurate data (Figure 9). To minimize these effects, it is necessary to implement appropriate cooling methods or thermal isolation. Future developments should prioritize improving sensor stability and accuracy under varying temperature conditions, addressing the impact of heat on measurement precision. In addition, integrating high-speed ADCs with powerful processors, such as those from NVIDIA, could significantly enhance data processing capabilities. This would enable faster, more accurate resonance detection and real-time analysis. Additionally, the use of advanced machine learning algorithms, combined with IoT technologies for continuous monitoring, could further enhance system efficiency and reliability, ensuring precise vibration measurements for industrial applications.

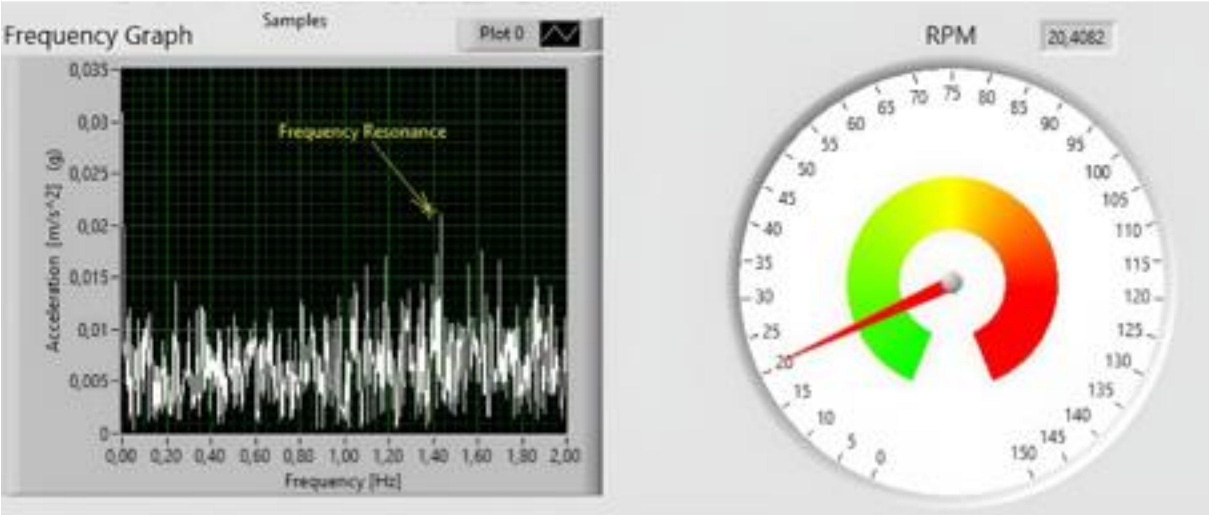

Fig. 7. Analysis of stepper motor vibrations at 20 RPM

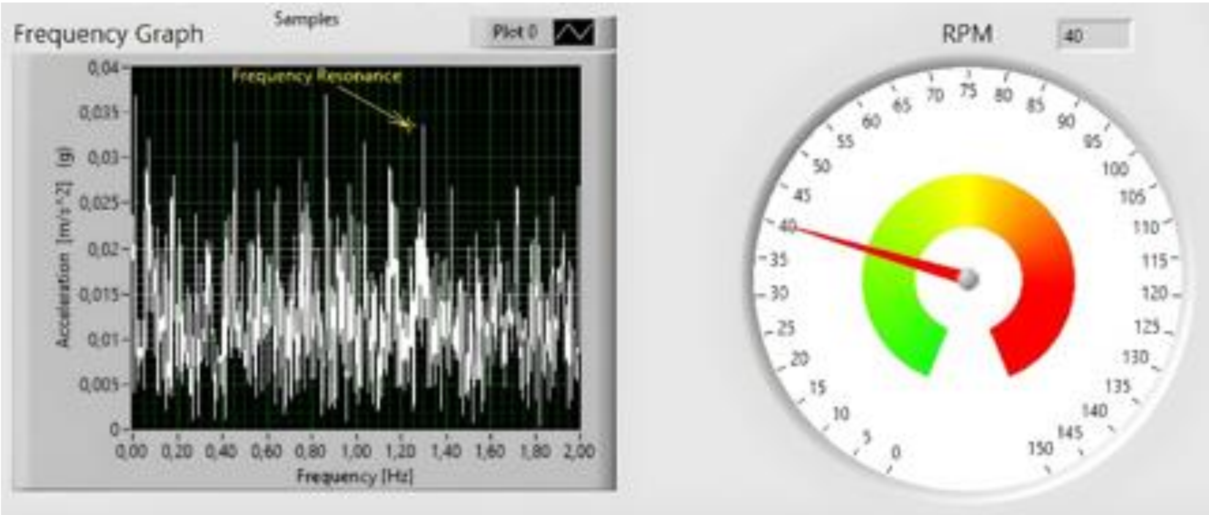

Fig. 8. Analysis of stepper motor vibrations at 40 RPM

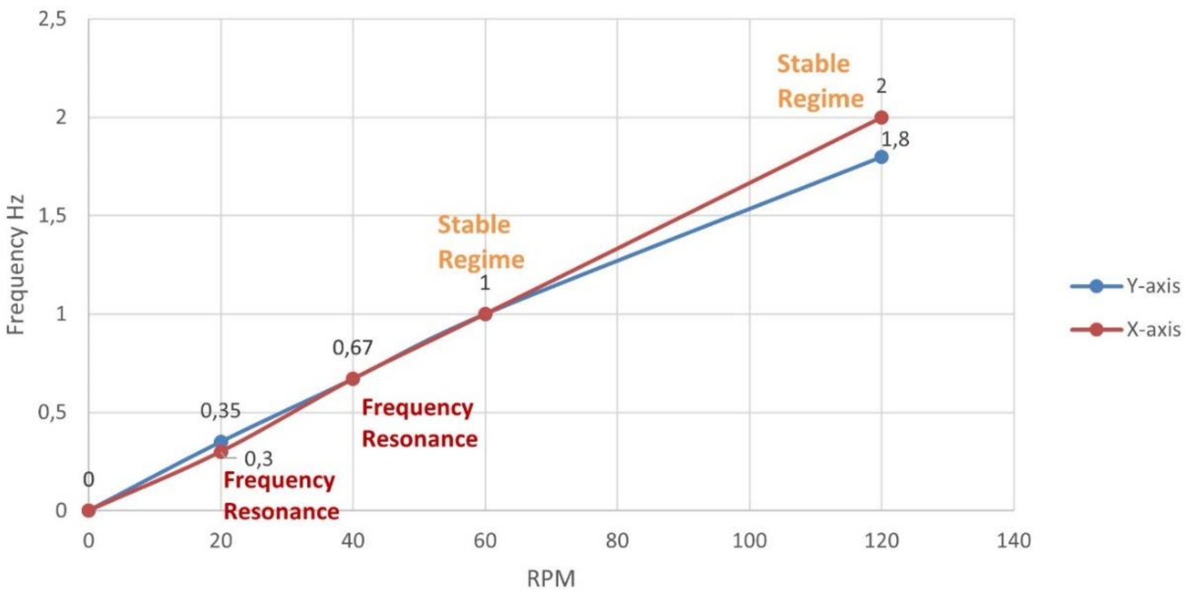

Fig. 9. Analysis of stepper motor resonance: RPM frequency correlation

REFFERENCES

[1] Stout, A. J. (2000): *Instrumentation techniques and improved control of stepper motor driven machinery*. Nottingham Trent University (United Kingdom).

[2] https://www.analog.com/media/en/technical-documentation/data-sheets/QSH4218-x-10k_datasheet_rev1.50.pdf

[3] Higuchi, T., Mizuno, T., Oshima, Y. (1981): *An analysis of midfrequency resonance phenomenon in permanent-magnet step motors*, IFAC Control Science and Technology, Kyoto, Japan, pp.2053-2056.

[4] Arva, M.-C., Stanica, M., & Anghel, N. (2018): Analysis of vibration and resonance characteristics in a low-speed 3-phase stepper motor. *Proceedings of the 10th International Conference on Electronics, Computers, and Artificial Intelligence (ECAI).*

[5] Kenjo, T., & Sugawara, A. (1994): *Stepper Motors and Their Microprocessor Controls*. Oxford University Press.

[6] Altintas, Y., & Weck, M. (2004): Chatter stability of metal cutting and grinding. *CIRP Annals – Manufacturing Technology*, **53** (2), 619–642.

[7] Smith, S., Tlusty, J., & Ziegert, J. (2010): The effects of vibration on CNC machining performance. *Journal of Manufacturing Science and Engineering*, **132** (3), 034501.

[8] Harun, W. S. W., Lim, S. Z. (2016): *Innovative Powder Delivery System for SLM*. DOI:10.13140/RG.2.1.2439.7688

[9] https://www.analog.com/media/en/technicaldocumentation/data-sheets/QSH4218-x-10k_datasheet_rev1.50.pdf

[10] Muain, M. F. B (2010): *Step motor speed controller* (Doctoral dissertation, Universiti Malaysia Pahang).

[11] Rodrigues, J. V. O., Pedroso, M. P. G., Silva, F. F. B. and Junior, R. G. L. (2021): Performance evaluation of accelerome-ters ADXL345 and MPU6050 exposed to random vibrational input. *Research, Society and Development*, **10** (15).

[12] Saponara, S., Fanucci, L., Bernardo, F., & Falciani, A. (2015): A network of vibration measuring nodes with integrated signal processing for predictive maintenance of high power transformers. *Proceedings of the 2015 IEEE 9th International Symposium on Intelligent Signal Processing (WISP)*, 1–4.

[13] National Instruments (2020): *The Fundamentals of FFT-Based Signal Analysis and Measurement*.

[14] Smith, J., Doe, R., & Brown, T. (2020): Multi-axis vibration analysis for rotational machinery. *Journal of Mechanical Engineering*, **45** (3), 123–135.

[15] Zhang, L., Wang, H., Chen, Y. (2018): Analysis of stepper motor resonance in CNC machines and strategies for mitigation. *International Journal of Advanced Manufacturing Technology*, **97** (5–8), 2345–2357.

Mechanical Engineering – Scientific Journal, Vol. **43,** No. 1, pp. 59–65 (2025)
Number of article: 694
In print: ISSN 1857–5293
Received: May 7, 2025
On line: ISSN 1857–9191
Accepted: May 12, 2025
UDC: 621.38.049.77:004.31]:[621.51:621.313.2
https://doi.org/10.55302/MESJ2543159a

Original scientific paper

DESIGN AND DEVELOPMENT OF MECHATRONIC SYSTEM FOR ROOM TEMPERATURE REGULATION

Maja Anačkova, Katerina Andonovska, Nikola Bimbiloski, Simon Prentoski, Damjan Pecioski

Faculty of Mechanical Engineering, "Ss. Cyril and Methodius" University in Skopje, P.O.Box 464, MK-1001 Skopje, Republic of North Macedonia
aleksandar.argilovski@mf.edu.mk

A b s t r a c t: This project describes a simple and efficient room temperature control system developed using a microcontroller, a DHT11 temperature and humidity sensor, a DC motor, and a motor driver. The DHT11 sensor continuously monitors the ambient temperature and sends the data to the microcontroller. Based on the temperature readings, the microcontroller adjusts the speed of the DC motor, which acts as a cooling unit. When the temperature exceeds a predefined upper limit, the microcontroller activates the DC motor to cool the room. When the temperature drops below the lower limit, the motor is turned off to conserve energy. The motor driver ensures the safe and efficient operation of the motor, ensuring compatibility with the microcontroller. This simple system offers an affordable and economical solution for regulating temperature in small spaces, demonstrating the practical application of basic electronics and microcontroller programming.

Key words: temperature; humidity; room temperature regulation; PID control

ДИЗАЈН И РАЗВОЈ НА МЕХАТРОНИЧКИ СИСТЕМ ЗА РЕГУЛАЦИЈА НА АМБИЕНТАЛНА ТЕМПЕРАТУРА

А п с т р а к т: Овој проект опишува едноставен и ефикасен систем за контрола на температурата во соба, развиен со користење на микроконтролер, DHT11 сензор за температура и влажност, DC-мотор и драјвер за моторот. Сензорот DHT11 континуирано ја мери амбиенталната температура и ги испраќа податоците до микроконтролерот. Врз основа на добиените мерења на температурата, микроконтролерот ја приспособува брзината на DC-моторот, кој служи како единица за ладење. Кога температурата ќе ја надмине претходно дефинираната горна граница, микроконтролерот го активира DC-моторот за да ја излади просторијата. Кога температурата ќе се намали под долната граница, моторот се исклучува за да се заштеди енергија. Драјверот за моторот овозможува безбедно и ефикасно работење на моторот, осигурувајќи компатибилност со микроконтролерот. Овој едноставен систем нуди достапно и економично решение за регулирање на температурата во мали простории, демонстрирајќи практична примена на основна електроника и програмирање на микроконтролери.

Клучни зборови: DHT11; температура; влажност; регулација на собна температура; PID контрола

1. INTRODUCTION

Temperature and humidity sensors are key components in engineering systems that require precise monitoring of environmental conditions. These sensors measure temperature and relative humidity, providing real-time data through continuous monitoring, and they are essential for maintaining controlled conditions in applications such as HVAC systems, industrial machinery, and agricultural equipment. These sensors are indispensable for optimizing thermal management, ensuring equipment reliability, and improving energy efficiency. Advances in sensor technology have resulted in compact, precise, and durable designs that can be easily integrated into mechanical systems.

Temperature sensors work by detecting changes in physical properties such as resistance, voltage, or current, which vary with temperature. These changes are then converted into electrical signals, which can be measured and interpreted to determine the temperature. Temperature sensors are classified into contact and non-contact measuring systems. Most instrumentation systems use contact-based measurement. Contact temperature measurement involves conducting heat from the surface of the object to the sensor. A portion of the body's thermal radiation is absorbed by the sensor and converted into a useful signal. Heat transfer from the centre of the sensor, which causes it to heat up, can lead to inevitable measurement errors. Non-contact temperature measurement systems are based on the principles of radiation thermometry, which has recently been used in medicine. The advantage of non-contact temperature measurement is that there is no heat absorption from the body or surface being measured. Various types of thermometers commonly used include mechanical, electrical, semiconductor devices, and thermal sensors [1].

In smart temperature sensor systems and microsystems (MEMS), integrated sensors are often used, combining sensing elements with the interface electronics required for communication, for example, with microcontrollers. The most common temperature sensing elements include transistors, thermocouples, and thermopiles, as these elements can be implemented using IC technology [2].

A humidity sensor works by detecting changes in the physical properties of a material when exposed to moisture in the air. These sensors are typically based on two main principles: resistance and capacitance. In resistive humidity sensors, the electrical resistance of a hygroscopic material changes as it absorbs moisture, and this change in resistance is directly related to relative humidity. A capacitive humidity sensor operates by measuring the change in capacitance of the sensor material when there is a change in ambient humidity. The sensor material is usually a dielectric material that absorbs water vapor from the air, altering its electrical properties. Capacitive sensors often use plastic or polymer as the dielectric material.

2. LITERATURE REVIEW

Traditional temperature measurement instruments are difficult to carry, expensive, and have limitations in monitoring specific locations (such as wounds or tumor ablation sites). Patient movement can also lead to inaccurate measurements. To address these issues, wearable, flexible, thin, and sensitive temperature sensors have become a research focus. The flexible temperature sensors use various materials. Common flexible substrates include polydimethylsiloxane (PDMS), polyimide (PI), polyurethane (PU), polyethylene terephthalate (PET), polyvinyl alcohol (PVA), polyvinyl butyral (PVB), paper, and silicone rubber. For better skin compatibility, biodegradable materials such as pectin, cotton, silk, and other cellulose-based materials are used. Heat-sensitive active materials include various carbon-based materials such as graphite (Gr) and graphene. Metallic materials like gold (Au), silver (Ag), copper (Cu), platinum (Pt), nickel (Ni), and aluminum (Al) are used for electrodes and wiring. Metal oxides such as vanadium dioxide (VO_2) and nickel oxide (NiO) are also important active materials. Polymers also serve as thermally sensitive materials, with hydrogels and carbon nanotubes increasing temperature sensitivity. Research has led to the development of flexible temperature sensors that can accurately monitor skin temperature, detect dehydration and heat stroke, and track wound healing progress. These sensors are integrated into fabrics, threads, and bandages, offering wireless data transmission capabilities. Results show that flexible temperature sensors can provide precise temperature monitoring [3].

The core material of a humidity sensor is its moisture-sensitive material. When the moisture-sensitive material interacts with humidity (through chemical action, biological action, or physical adsorption), its quality, thickness, and optical, mechanical, and electrochemical characteristics change, altering the impedance between detection electrodes. In this way, humidity information can be obtained by detecting the output signal of the impedance. Graphene is a new type of carbon material with a flexible, two-dimensional structure. Due to its excellent lattice stability and mechanical flexibility, graphene-based materials can be used in flexible humidity sensors. Since graphene oxide (GO) and reduced graphene oxide (rGO) are rich in oxygen-containing functional groups and have a large specific surface area for molecular adsorption, they have great potential for widespread application in flexible humidity sensors. With their high sensitivity, excellent flexibility, good elasticity, and stability, graphene-based flexible humidity sensors have significant potential for applications, including personal health monitoring. They can be placed on the human body or clothing to detect signals from human activity and obtain various physiological information. Graphene-based flexible humidity sensors can be classified into four categories: monitoring human respiration, monitoring skin humidity, detecting sweat, and detecting environmental humidity [4].

A sensor that combines both temperature and humidity measurements is the DHT11. The DHT11 temperature and humidity sensor can be used for automatic room temperature control using Arduino. The user sets the minimum and maximum reference temperature range via a keypad. The DHT11 sensor measures the room's ambient temperature and provides the result in degrees Celsius. The reference and measured values are displayed on an LCD. The Arduino microcontroller, as the system's processing unit, receives the measured data from the sensor and compares it with the set value. The results are as follows:

→ When the measured room temperature is lower than the minimum set value, the microcontroller activates the heating system.

→ If the measured room temperature is higher than the maximum set value, the fan is activated.

→ The fan speed is controlled via Pulse Width Modulation (PWM), depending on the difference between the sensor's measurement and the maximum set value. The greater the temperature difference, the higher the fan's duty cycle and speed.

→ Finally, if the measured room temperature is within the set range, all devices remain off [5].

3. SENSOR ANALYSIS METHODOLOGY

3.1. *Conceptual analysis of the measurement system using the DHT11 sensor*

Our measurement system consists of several key components working together to monitor and control the room's temperature as shown in Figure 1.

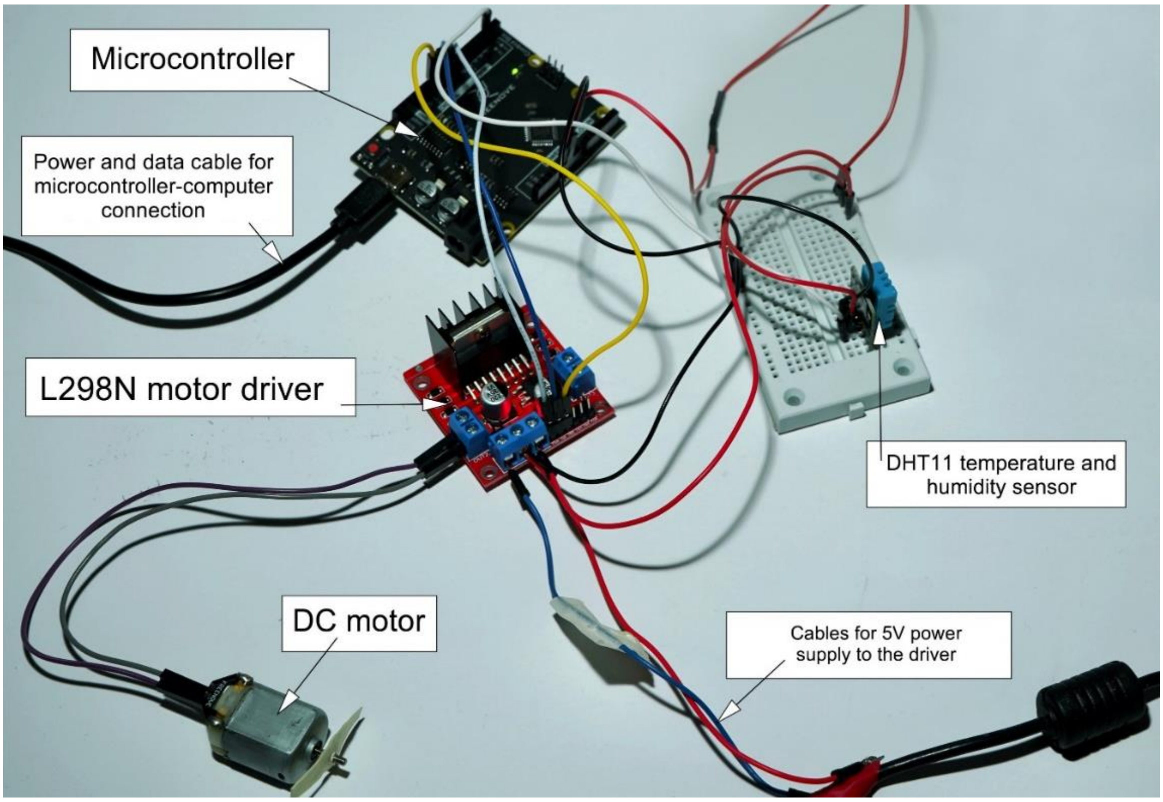

Fig. 1. All physical components illustrating the connection between them
1. **Microcontroller** – The central control unit, responsible for processing the DHT11 sensor data and controlling the DC motor. 2. **DHT11 sensor** – Measures ambient temperature and humidity, providing real-time data for temperature adjustment. 3. **DC motor** – Acts as a cooling unit or ventilation device. 4. **Motor driver (L298N)** – Ensures safe and efficient motor operation, as microcontrollers cannot directly supply the required voltage and current. 5. **Power supply** – Provides 5V power to the motor driver and other components.

The system operates as follows: The DHT11 sensor continuously monitors the temperature and humidity in the room, sending the data to the microcontroller, which uses PID control to continuously regulate the number of rotations to maintain 30 degrees Celsius in the room. The microcontroller generates a PWM signal and sends it to the driver, which controls the motor.

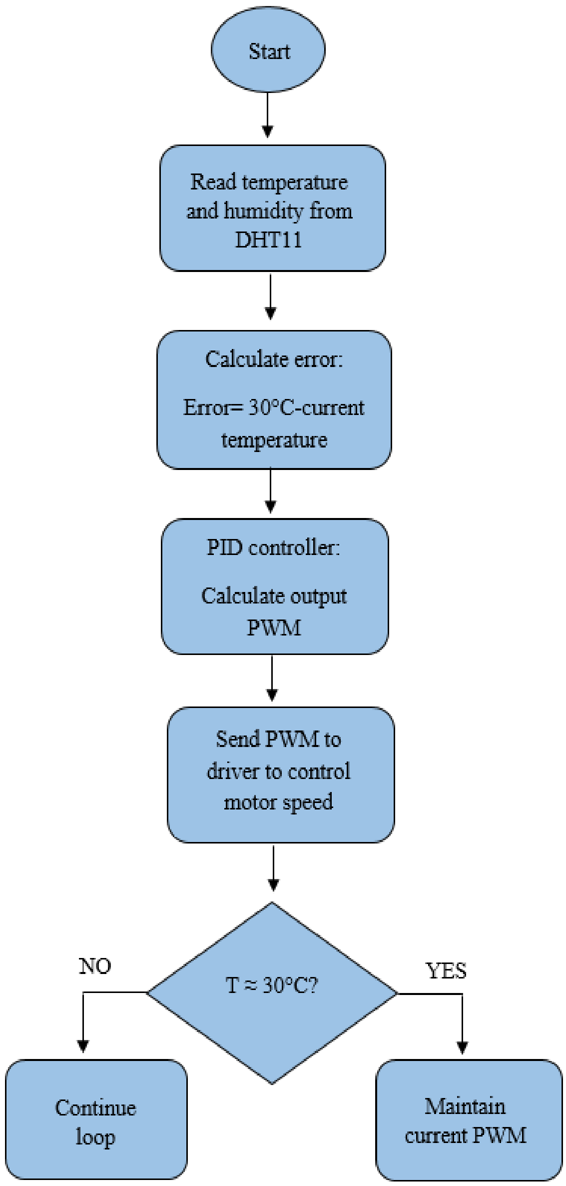

Fig. 2. Flowchart for fan speed control

The DHT11 sensor is used for measuring air temperature and humidity. This sensor is designed for applications with low power consumption, high stability, and compatibility with IoT-based systems. The DHT11 has a measurement accuracy of ±1°C for temperature and ±5% for relative humidity, making it an ideal choice for real-time environmental monitoring applications [6]. The DHT11 sensor measures humidity and temperature using a capacitive humidity sensor and a thermistor. The capacitive sensor detects changes in humidity by measuring the change in capacitance caused by moisture in the air. This change is converted into a digital signal. The thermistor changes its resistance based on temperature; the sensor reads this resistance and converts it into a temperature value. The sensor communicates with the microcontroller using a specific protocol, sending a total of 40 bits of data, which include humidity and temperature measurements along with a checksum for error detection. For example, the first 16 bits represent humidity, the next 16 bits represent temperature, and the last 8 bits serve as a verification check to ensure data integrity. Changes in resistance (for temperature) and capacitance (for humidity) are initially analog signals, but the DHT11 has a built-in microcontroller that converts these analog signals into digital data. The ADC process involves sampling the signals at regular intervals, then quantizing them into discrete values representing temperature and humidity levels. Once the microcontroller converts the analog data into digital values, it formats the data into a standardized output (usually a series of binary numbers) representing both temperature and humidity. The microcontroller reads the pulse widths of the signal sent by the DHT11, processes them to extract the temperature and humidity values, and converts these numbers into a readable format (e.g., Celsius for temperature and percentage for humidity).

3.2 *Analysis of sensor performance parameters*

Main static and dynamic characteristics of the sensor:

Humidity range: 20% to 90% RH

Temperature range: 0°C to 60°C

Humidity accuracy: ±5% RH

Temperature accuracy: ±2°C

Resolution: 8-bit for both humidity and temperature.

Sampling frequency: 1Hz

Power supply: 3.3V to 5.5V

Current consumption: 0.5 to 2.5 mA during operation, 100 to 150 µA in standby mode [7].

Response time: A few seconds for temperature, 5–30 seconds for humidity changes.

While the DHT11 performs well under typical weather conditions within its specifications, extreme environments such as condensation or lack of protection can degrade its accuracy and lifespan. For better performance in specific weather conditions, more durable sensors such as the DHT22 or BME280 can be used. These sensors offer a wider range and higher accuracy, and the BME280 also has a higher sampling frequency.

3.3. *Sensor applications*

The main applications of the DHT11 include agriculture (monitoring environmental conditions for optimal crop growth), pharmaceuticals (ensuring proper storage conditions for medications), biomedical applications (maintaining controlled environments for patient care and laboratory experiments), home automation (smart home climate control systems), and meteorological stations (collecting data for weather studies) [8].

4. RESULTS

The system was tested by setting up the hardware components and using the Arduino IDE to execute the instructions, along with MATLAB to display real-time graphs of the temperature (°C), humidity (%), and motor speed (RPM). When power is supplied to the system, the sensor begins measuring temperature and humidity. PID control is implemented in the microcontroller to regulate the fan speed and maintain a stable temperature.

It continuously compares the measured temperature to the desired setpoint (30°C) and calculates a control signal based on the error. The control signal determines the duty cycle of a PWM signal, which is then sent to the motor driver to adjust the fan speed.

The PID controller calculates the control output using three terms:

– *Proportional (P):* Reacts to the current error by applying an immediate correction.

– *Integral (I):* Accumulates past errors to eliminate steady-state deviations.

– *Derivative (D):* Predicts future errors and reduces sudden fluctuations.

The control signal is determined using the following formula:

$$u(t) = K_p e(t) + K_i \int_0^t e(t)\ dt + K_d \frac{de(t)}{dt}$$

where:

K_p is the proportional gain,

K_i is the integral gain,

K_d is the derivative gain,

$e(t)$ is the error.

This feedback control ensures that the system dynamically adjusts the fan speed to maintain the set temperature with minimal deviation.

For the purpose of visual representation of the collected data, three separate graphs for the humidity, temperature and RPM (revolutions per minute), are extracted as shown in Figure 3. Furthermore, based on the PID feedback control, it is conluded that the ouput(RPM) curve follows almost the same curve of the input (temperature). This gives us the opportunity to make certain post-processing calculations that allow us to dive deeper in understanding the meaning of the curves in the graphs themselves.

Table 1 represents the dots from Figure 4.

As shown in Figure 5 the orange line represents the behavior of the system: the ratio between RPM values and temperature values. The dotted black line is a linear trendline fitted to the orange line's data to give a simplified model of the relationship. The trendline is given as:

$$\text{RPM} = 138.98 \cdot \textit{temperature} - 934.36$$

The equation is in the form of a straight line $y = kx + b$ where y is RPM (dependent variable), x is the temperature, k is the slope and b is the y-intercept. From the trendline we can conclude that for each 1°C increase, the RPM increases by 138.98 on average since the slope has a value of 138.98. This shows a positive, strong correlation between the temperature and motor speed. The y-intercept has a value of –934.36 and it is important for defining the full line equation.

The trendline serves as a mathematical simplification of how the system behaves. In our case, it gives the ability to easily predict and estimate the RPM values for any given temperature within or slightly outside the range, which can help in controlling the system.

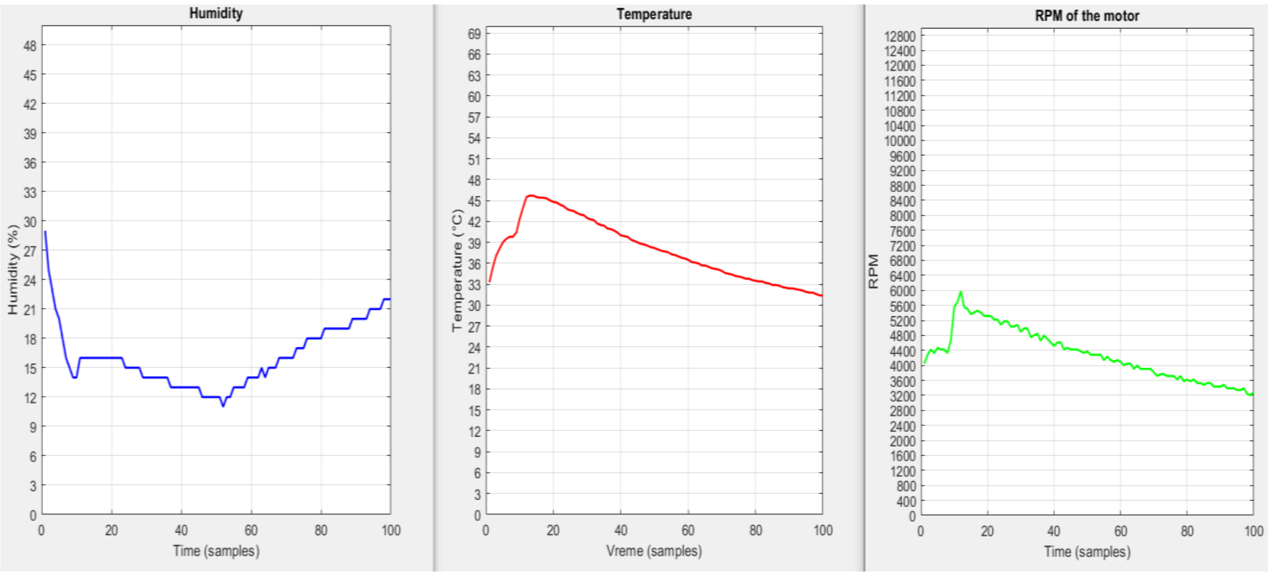

Fig. 3. Real-time graphs of the humidity, temperature and RPM and their influence on each other

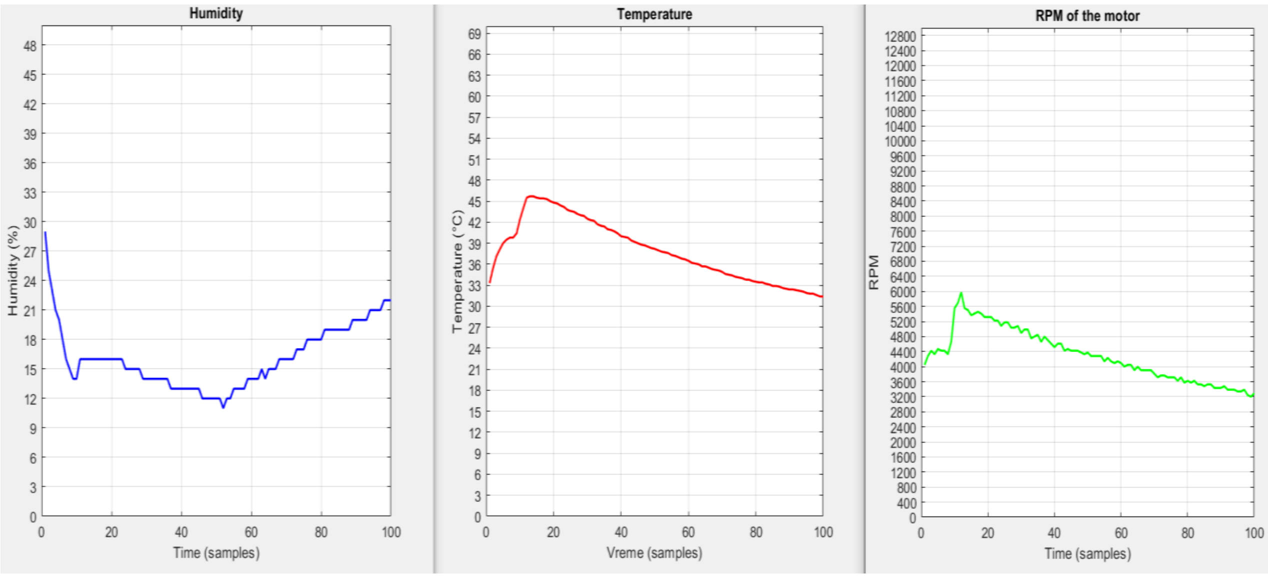

Fig. 4. The graphs with dotted points per 10 samples of the time axis

Table 1

The dots from Figure 4

	A	B	C	D	E	F	G	H	I	J
Humidity (%)	29	14	16	14	13	11	14	16	18	20
Tepmperature (°C)	33	41.54	44.9	42.2	40.05	38.1	36.1	34.5	33.2	32.7
RPM	4000	4790	5400	4980	4500	4400	4110	3810	3600	3420
Ratio RPM/Temperature	121.21	115.42	120.27	118.01	111.1	115.49	113.,86	110.43	108.43	104.59

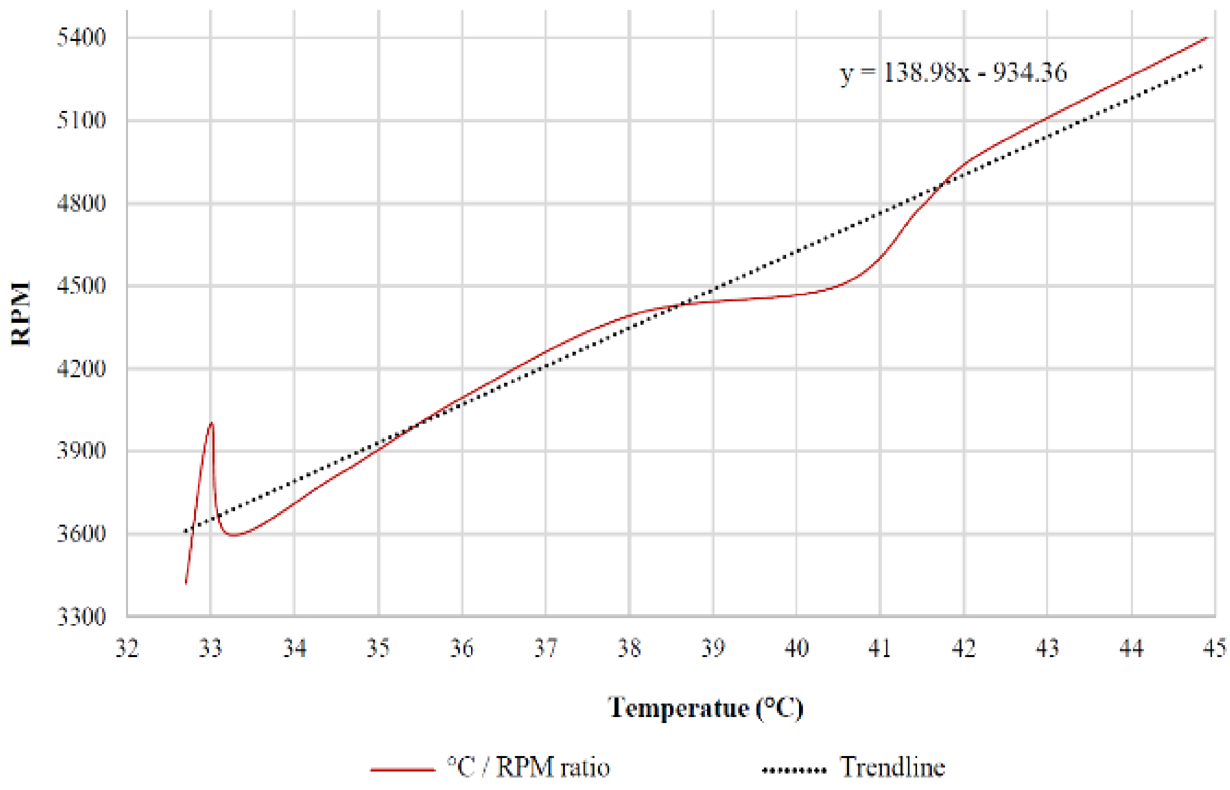

Fig. 5. Effect of temperature on motor speed (RPM) with linear trendline

5. CONCLUSION

The room temperature control system developed in this project successfully demonstrates how a simple combination of a microcontroller, a DHT11 sensor, a DC motor, and a motor driver can be effectively used to regulate ambient temperature. The system achieved its primary goal of maintaining the desired temperature by monitoring real-time temperature data and activating the motor when necessary. The project showcased the functionality of the motor driver, which safely amplifies the control signals from the microcontroller to power the motor, while the use of a PWM signal enabled a simple and efficient method for motor control. This system is energy-efficient, as the motor operates only when necessary, reducing power consumption and extending the motor's lifespan. Additionally, it is cost-effective and easy to implement, making it suitable for small rooms or environments where basic temperature regulation is required.

REFERENCES

[1] Onwubolu, G. (2005): *Mechatronics: Principles and Applications*. Elsevier.

[2] Meijer, G. C., Wang, G. and Heidary, A. (2018): Smart temperature sensors and temperature sensor systems. In: *Smart Sensors and MEMs* (pp. 57–85). Woodhead Publishing.

[3] Su, Y., Ma, C., Chen, J., Wu, H., Luo, W., Peng, Y., Luo, Z., Li, L., Tan, Y., Omisore, O.M. and Zhu, Z. (2020): Printable, highly sensitive flexible temperature sensors for human body temperature monitoring: a review. *Nanoscale Research Letters*, **15**, pp.1-34.

[4] Liang, R., Luo, A., Zhang, Z., Li, Z., Han, C. and Wu, W. (2020): Research progress of graphene-based flexible humidity sensor. *Sensors*, **20** (19), p. 5601.

[5] Debele, G. M. and Qian, X. (2020): Automatic room temperature control system using Arduino Uno R3 and DHT11 sensor. In: *2020 17th International Computer Conference on Wavelet Active Media Technology and Information Processing (ICCWAMTIP)* (pp. 428-432). IEEE.

[6] Tukan, M. I. (2024): Monitoring tools using DHT11 sensor, soil moisture sensor and motion sensor. *Journal of Frontier Research in Science and Engineering*, **2** (4), pp. 38–48.

[7] Gay, W. and Gay, W. (2018): DHT11 sensor. *Advanced Raspberry Pi: Raspbian Linux and GPIO Integration*, pp. 399-418.

[8] Srivastava, D., Kesarwani, A. and Dubey, S. (2018): Measurement of temperature and humidity by using Arduino tool and DHT11. *International Research Journal of Engineering and Technology (IRJET)*, **5** (12), pp. 876–878

Mechanical Engineering – Scientific Journal, Vol. **43,** No. 1, pp. 67–70 (2025)
CODEN: MINSC5
In print: ISSN 1857–5293
On line: ISSN 1857–9191

INSTRUCTIONS FOR AUTHORS

The *Mechanical Engineering – Scientific Journal* is published twice yearly. The journal publishes **original scientific papers, short communications, reviews** and **professional papers** from all fields of mechanical engineering.

The journal also publishes (continuously or occasionally) the bibliographies of the members of the Faculty, book reviews, reports on meetings, informations of future meetings, important events and data, and various rubrics which contribute to the development of the corresponding scientific field.

Original scientific papers should contain hitherto unpublished results of completed original scientific research. The number of pages (including tables and figures) should not exceed 15 (28 000 characters).

Short communications should also contain completed but briefly presented results of original scientific research. The number of pages should not exceed 5 (10 000 characters) including tables and figures.

Reviews are submitted at the invitation of the Editorial Board. They should be surveys of the investigations and knowledge of several authors in a given research area. The competency of the authors should be assured by their own published results.

Professional papers report on useful practical results that are not original but help the results of the original scientific research to be adopted into scientific and production use. The number of pages (including tables and figures) should not exceed 10 (18 000 characters).

Acceptance for publication in the Journal obliges the authors not to publish the same results elsewhere.

SUBMISSION

The article and annexes should be written on A4 paper with margins of 2.5 cm on each side with a standard font Times New Roman 11 points and should be named with the surname of the first author and then if more and numbered. It is strongly recommended that on MS Word 2003 or MS Word 2007 and on PDF files of the manuscript be sent by e-mail:

mesj@mf.edu.mk.

A letter must accompany all submissions, clearly indicating the following: title, author(s), corresponding author's name, addres and e-mail addres(es), suggested category of the manuscript and a suggestion of five referees (their names, e-mail and affiliation).

Articles received by the Editorial Board are sent to two referees (one in the case of professional papers). The suggestions of the referees and Editorial Board are sent to the author(s) for further action. The corrected text should be returned to the Editorial Board as soon as possible but in not more than 30 days.

PREPARATION OF MANUSCRIPT

The papers should be written in the shortest possible way and without unnecessary repetition.

The original scientific papers, short communications and reviews should be written in English, while the professional papers may also be submitted in Macedonian.

Only SI (Système Internationale d'Unites) quantities and units are to be used.

Double subscripts and superscripts should be avoided whenever possible. Thus it is better to write $\nu_3(PO_4)$ than $\nu_{3_{PO_4}}$ or exp(–E/RT) than $e^{-E/RT}$. Strokes (/) should not be used instead of parentheses.

When a large number of compounds have been analyzed, the results should be given in tabular form.

Manuscript should containt: title, author(s) full-name(s), surname(s), address(es) and e-mail of the corresponding author, short abstract, key words, introduction, experimental or theoretical background, results and discussion, acknowledgment (if desired) and references.

The **title** should correspond to the contents of the manuscript. It should be brief and informative and include the majority of the key words.

Each paper should contain an **abstract** that should not exceed 150 words, and **3–5 key words**. The abstract should include the purpose of the research, the most important results and conclusions.

The **title**, **abstract** and **key words** should be translated in Macedonian language. The ones written by foreign authors will be translated by the Editorial Board.

In the **introduction** only the most important previous results related to the problem in hand should be briefly reviewed and the aim and importance of the research should be stated.

The **experimental** section should be written as a separate section and should contain a description of the **materials used and methods** employed – in form which makes the results reproducible, but without detailed description of already known methods.

Manuscripts that are related to **theoretical studies**, instead of experimental material, should contain a sub-heading and the **theoretical background** where the necessary details for verifying the results obtained should be stated.

The **results and discussion** should be given in the same section. The discussion should contain an analysis of the results and the conclusions that can be drawn.

Figures (photographs, diagrams and sketches) and **mathematical formulae** should be inserted in the correct place in the manuscript, being horizontally reduced to 8 or 16 cm. The size of the symbols for the physical quantities and units as well as the size of the numbers and letters used in the reduced figures should be comparable with the size of the letters in the main text of the paper. Diagrams and structural formulae should be drawn in such a way (e.g. black Indian ink on white or tracing paper) as to permit high quality reproduction. The use of photographs should be avoided. The tables and the figures should be numbered in Arabic numerals (e.g., Table 1, Figure 1). Tables and figures should be self-contained, i.e. should have captions making them legible without resort to the main text. The presentation of the same results in the form of tables and figures (diagrams) is not permitted. The use of equation editor (MS Word, Microsoft Equation, Math Type 6.0 Equation) for typesetting the equations is recommended. Strokes (/) should not be used instead of parentheses.

Figures and tables must be centred in the column. Large figures and tables may span across both columns (Figure 1).

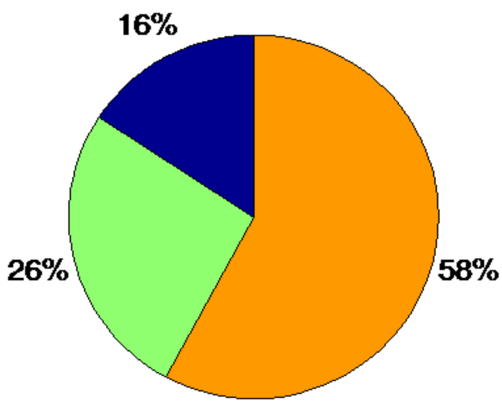

Fig. 1. Example of a graph and a single-line caption (colour)

Graphics may be full colour. Please use only colours which contrast well both on screen and on a black-and-white hardcopy because the Journal is published in black-and-white, as shown in Figure 2. The colour version is only for the electronic version of the Journal.

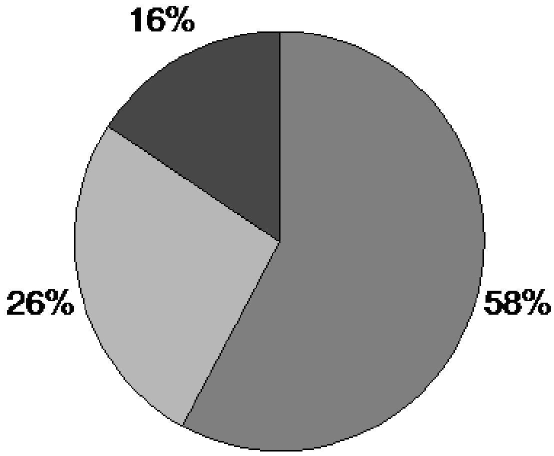

Fig. 2. Example of a graph and a single-line caption (bleck and vhite)

Please check all figures in your paper both on screen and on a black-and-white hardcopy. When you check your paper on a black-and-white hardcopy, please ensure that:

– the colours used in each figure contrast well (Figure 3),

– the image used in each figure is clear,

– all text labels in each figure are legible.

Please check all figures in your paper both on screen and on a black-and-white hardcopy. When you check your paper on a black-and-white hardcopy, please ensure that the image used in each figure is clear and all text labels in each figure are legible.

Fig. 3. Example of an image as it will appear at the electronic version of the Journal and a multi-line caption

Footnotes are also not permitted.

The **reference** should be given in a separate section in the order in which they appear in the text. The surname of one or two authors may be given in the text, whereas in the case of more than two authors they should be quoted as, for example:

Examples of reference items of different categories shown in the References section include:

- example of a book in [1]
- example of a book in a series in [2]
- example of a journal article in [3]
- example of a conference paper in [4]
- example of a patent in [5]
- example of a website in [6]
- example of a web page in [7]
- example of a databook as a manual in [8]
- example of a datasheet in [9]
- example of a master/Ph.D. thesis in [10]
- example of a technical report in [11]
- example of a standard in [12]

All reference items must be in 9 pt font. Please use Regular and Italic styles to distinguish different fields as shown in the References section. Number the reference items consecutively in square brackets (e.g. [1]).

When referring to a reference item, please simply use the reference number, as in [2]. Do not use "Ref. [3]" or "Reference [3]" except at the beginning of a sentence, e.g. "Reference [3] shows …". Multiple references are each numbered with separate brackets (e.g. [2], [3], [4–6]).

The **category** of the paper is proposed by the author(s), but the Editorial Board reserves for itself the right, on the basis of the referees' opinion, to make the final choice.

Proofs are sent to the author(s) to correct printers' errors. Except for this, alterations to the text are not permitted. The proofs should be returned to the Editorial Board in 2 days.

The author(s) will receive, free of charge, 1 reprints of every paper published in the Journal.

REFERENCES

[1] Surname, N(ame).; Surname, N(ame). (Year): *Name of the Book*, Publisher.

[2] Surname, N(ame).; Surname, N(ame). (Year): *Name of the Book*, Name of the Series. Publisher, **vol.** XXX.

[3] Surname, N(ame).; Surname N(ame). (Year): Title of the article, *Name of the Journal*, **vol. XX,** No. XX, pp. XXX–XXX.

[4] Surname, N(ame).; Surname N(ame). (Year): Title of the article, *Proceedings of the Name of the Conference,* vol. **XX,** pp. XXX–XXX.

[5] Surname, N(ame).; Surname, N(ame).: *Name of the Patent*, Institution that issued the patent and Number of the patent (Date dd. mm. yyyy).

[6] N.N. (Year): *The XXX web site*, web address.

[7] Surname, N. (Year): *XXX homepage on XXX*, web address.

[8] N.N. (Year): *Title of the Manual*, Name of the Organization.

[9] N.N.: *XXX data sheet*, Name of the Organization.

[10] Surname, N. (Year): *Title of the Thesis*, Master/Ph.D. thesis (in Language), Institution.

[11] Surname, N(ame).: Surname, N(ame). (Year): *Title of the Report*, Organization that issued the report, number of the report.

[12] Institution that issued the standard (Year): *Name of the Standard* & Number of the standard.